Spark Ablated Metal Oxide Nanoparticles for Gas Sensing

MSc. Thesis

Esad Beydilli

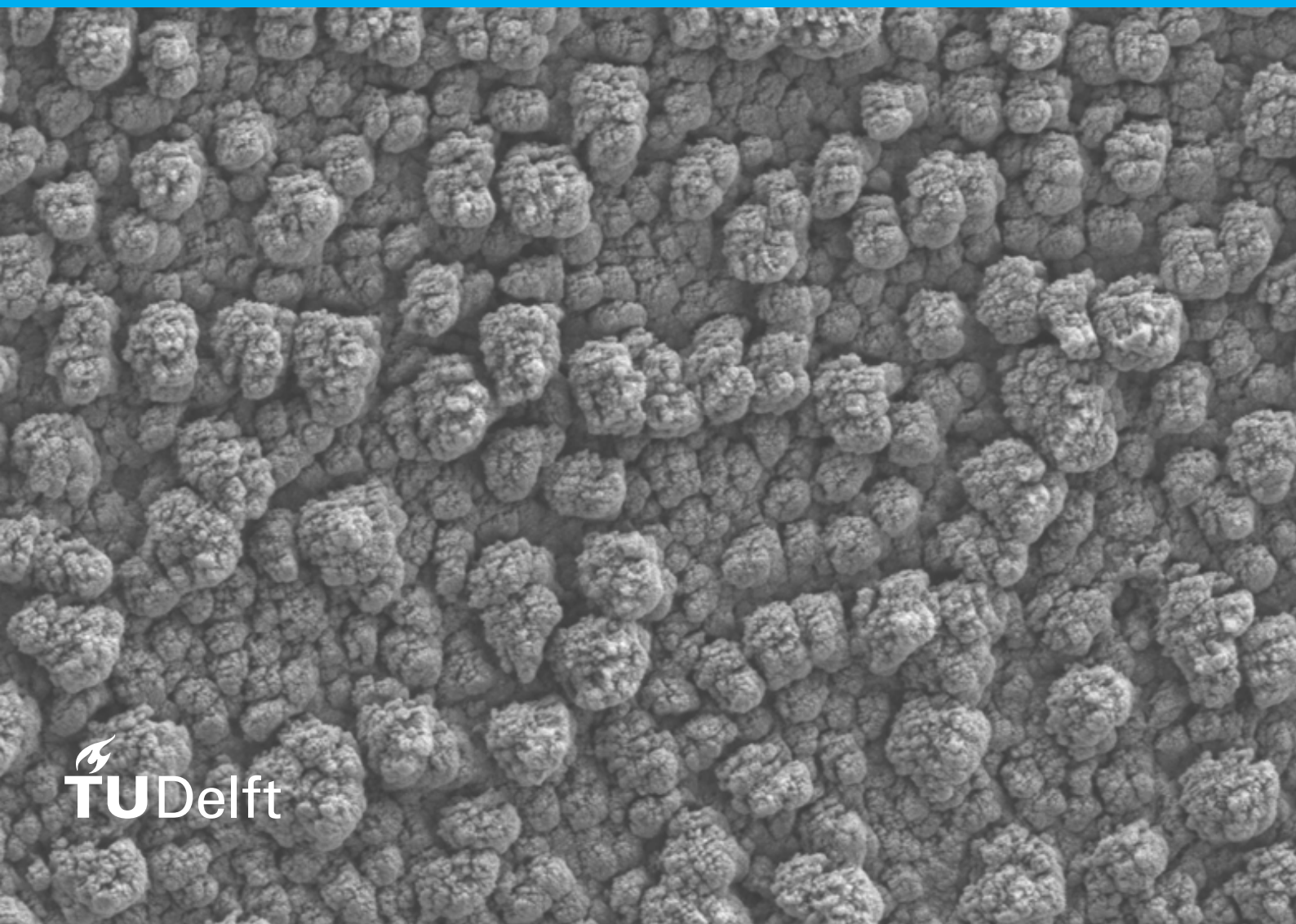

TU Delft

Spark Ablated Metal Oxide Nanoparticles for Gas Sensing

MSc. Thesis

by

Esad Beydilli

to obtain the degree of Master of Science
at the Delft University of Technology,
to be defended publicly on Tuesday October 25, 2022 at 14:00.

Student number:	4444981	
Thesis committee:	Dr. ir. S. Vollebregt,	TU Delft, supervisor
	Prof. Dr. P. J. French,	TU Delft
	Dong Hu,	TU Delft, supervisor
	Joost van Ginkel,	TU Delft, supervisor

An electronic version of this thesis is available at `http://repository.tudelft.nl/`.

TU Delft Delft University of Technology

Acknowledgements

I am very grateful to have had all the help I received from my supervisors Sten, Dong and Joost, whether if it was with the project itself or anything outside of it. This all would not have been possible without their support and patience throughout the year. I would also like to thank them for allowing me to delve into the world of nanoparticles, a field that I was not familiar with at all. I would like to thank the other members of the ECTM group for helping out when I needed it and making the entire experience much more enjoyable. Thanks to Sohrab, Mustafeez, Rami, Devashish, Tom, Hanxing, Nikhil, Shriya, Michael, Samantha, Shirley, Bram, Samhitha, Weiping, Filippo and Laveena (forgive me if I forgot names). The lunches and coffee breaks will definitely be missed a lot. Of course I would also need to thank them for their selfless deed of helping me out during my job seeking process. Thanks are also due to the EKL staff for keeping things up and running, and providing all the help with otherwise risky equipment. I would definitely need to thank Nikki and Marian for the new coffee machine as I have been using it a lot. Finally I would like to thank my family for supporting me throughout my whole life.

Abstract

Metal oxide nanoparticle gas sensors show promise due to their high sensitivity towards a wide range of gases, low costs, and low complexity. Particle sizes at nanometers offer a high surface-to-volume ratio which provides more areas on the surface where reactions can occur. This work presents the application of spark ablated nanoparticles on chemiresistors and chemFETs, and does a study on whether spark ablated nanoparticles are a viable alternative to nanoparticles generated using other methods. The focus in this thesis is on pure metal oxide nanoparticles without any addition of dopants or decorations. Devices are fabricated with different interdigitated electrode dimensions. The effect of electrode width and gap size on the gas response is studied by comparing the sensing performance of the devices. In this work, a very high sensitivity of 1300% is achieved towards 35% relative humidity using a 1x1 mm device with SnO_2 nanoparticles. Towards 20 ppm of ethanol, sensitivities of 39% and 67% are achieved using 1x1 mm and 4x1 mm devices with SnO_2 nanoparticles respectively, which implies that spark ablated nanoparticles could be a viable alternative to particles generated using other methods. The full recovery time after gas exposure seems to be very long and takes around an hour for some devices at 200 $°C$. Possible solutions for this are setting a higher temperature (not possible with the used setup), or reducing the particle size (~20 nm in this study). The electrode finger widths and gap sizes are varied between 2-15 μm for each device. However, no correlation is found between electrode geometry and gas response within this range, suggesting that differences in gas response between devices likely stem from nanoparticle layer quality differences.

Contents

1 Introduction

There is a growing demand for gas sensors as a result of technological advancements. Massive amounts of toxic gases are getting released into the atmosphere that pose a threat to the climate or even to human health. Most recently in the Netherlands, the Dutch high court made the decision to suspend permits for constructions that may emit nitrogen compounds and severely pollute the atmosphere [1]. NO_2 is an inorganic gas commonly released by combustion engines that causes serious damage to the environment as well as the human respiratory system at higher concentrations [2]. The severity of pollution due to NO_2 resulted in the construction of houses and airport runways to be stalled by lawmakers. Ammonia is another nitrogen compound that is most commonly emitted by manure, and many experts believe that the animal farm sector must be downsized as a measure against pollution. Volatile Organic Compounds(VOCs) are commonly emitted from building materials and paints. Ethanol is the most commonly occurring VOC in homes and the buildup of it leads to indoor air pollution which can cause health issues in households and offices [3]. Gas sensors are also sought after in industrial environments where hazardous gases are involved that might endanger individuals working in such areas.

As time passes and more pollutants are released into the atmosphere harming the climate, wildlife and society, smaller amounts of gases continue to have greater consequences. This implies that the sensitivity requirements for gas sensors become more restrictive over time, and they must be able to detect smaller concentration changes. Sensors with higher sensitivity allow for precautionary measures to be taken with the least amount of harm being done, whether it is interior or outdoor pollution.

1.1. Motivation & Objectives

One characteristic of the previously mentioned gases is that they have the ability to act as either reducing or oxidizing agents, meaning that they are able to donate or accept electrons during a chemical reaction. The majority of gas sensors are so-called chemiresistors, which are electrically resistive gas sensing devices that use either an n-type or a p-type semiconductor as the sensing element. When a reducing or oxidizing gas comes in contact with the semiconductor layer, it causes a change in the conductivity of the device. This change is correlated to the concentration of the gas that is present in the area.

Many existing chemiresistive gas sensors use metal oxide semiconductors such as SnO_2, ZnO and CuO as their sensing layer. The main advantages of such sensors are their low costs, low fabrication complexity, and relatively high sensitivity towards a wide range of gases. However, currently available metal oxide gas sensors often suffer from limitations such as the need for high operating temperature, sensitivity towards variations in humidity, and the need for a large surface area in order to maintain high sensitivity.

In this work, the focus is on improving the sensitivity of metal oxide gas sensors. The development and operation of 1x1mm and 4x1mm resistive gas sensing devices with metal oxide nanoparticles as their sensing layers are covered. Layers consisting of nanosized particles allow for a larger specific surface area and thus for a higher gas sensitivity per area. The devices are designed such that they have a low fabrication complexity and a high contact area with the implementation of interdigitated electrodes. As an additional attempt

to amplify the gas response of the devices, the chemiresistors are converted to chemFETs by adding a third terminal to be used as their gates.

Metal oxide nanoparticle layers are synthesized in this work using spark ablation, a relatively new method that offers high purity, control over size and composition [4]. Two electrodes are placed close to each other and a spark occurs between them and vaporizes parts of the electrodes, forming aerosol nanoparticles that are ready to be deposited. Because of the simplicity of the setup, the method has relatively low costs and high scalability.

This thesis seeks for answers for whether spark ablated nanoparticles can provide a higher gas sensitivity compared to nanoparticles generated with other methods, how electrode width and gap size affect the sensitivity, and whether gate biasing can improve the response of metal oxide gas sensors. The focus of this thesis is on the gas sensing performance of spark ablated SnO_2 nanoparticles, and also on the characteristics of ZnO and CuO nanoparticles in a lesser degree.

1.2. Outline

The composition of this thesis is as follows: the next chapter (2) is a compilation of information found in literature, regarding the gas sensing mechanism, commonly used sensing metal oxides, nanoparticle synthesis methods, and sensing device structures. Chapter 3 describes the methods used in this thesis to obtain results, most notably nanoparticle synthesis and characterization methods, and test setups used to test the conductivity of nanoparticle layers. Chapter 4 presents the (lithography masks of) two designs made in this thesis and their purposes. The fabrication steps of the devices are explained in chapter 5. In chapter 6, the characterization results, most notably electron microscopy, x-ray diffraction, and conductance data of nanoparticles on test dice as well as on devices are shown and the optimal settings for producing sufficiently high quality nanolayers are chosen. In the final chapter (7), gas sensing results are given and conclusions are drawn regarding how spark ablated metal oxide nanoparticles compare with other synthesis methods in terms of sensing performance, what effect device geometry has on the gas response, and how much the presence of humidity can have an effect on the gas sensing performance.

2

Background Knowledge

This chapter serves as a compilation of state-of-the-art information regarding gas sensors. It explains the general mechanism behind metal oxide gas sensing and covers commonly used nanoparticle synthesis methods and device structures. The chapter ends with table 2.1 which lists the characteristics of existing metal oxide gas sensors and will be used later in this thesis for comparison purposes.

2.1. Gas Sensing Mechanism

Semiconductors are often categorized into n-type and p-type materials. The electrical conductance of n-type semiconductors increases for reducing gases and decreases for oxidizing gases, whereas the opposite is valid for p-type semiconductors [5]. The operation of semiconductor gas sensors is generally explained using the adsorption/desorption model [6]. When an n-type semiconductor is exposed to air, oxygen molecules get adsorbed into oxygen vacancies on the surface. The oxygen molecules consume electrons from the material, resulting in a depletion layer and a drop in conductivity. When a reducing gas from the environment reacts with the negative oxygen species, the consumed electrons return to the semiconducting material and the conductivity of the material gets restored. An oxidizing gas will result in a decrease in conductivity instead, as it will result in more adsorption of oxygen. For a p-type semiconductor, adsorption of oxygen molecules results in the formation of a hole accumulation layer and thus an increase in conductivity. Reducing and oxidizing gases thereafter decrease and increase the conductivity, respectively. The sensing mechanism of an n-type semiconductor for a reducing gas is schematically shown in figure 2.1.

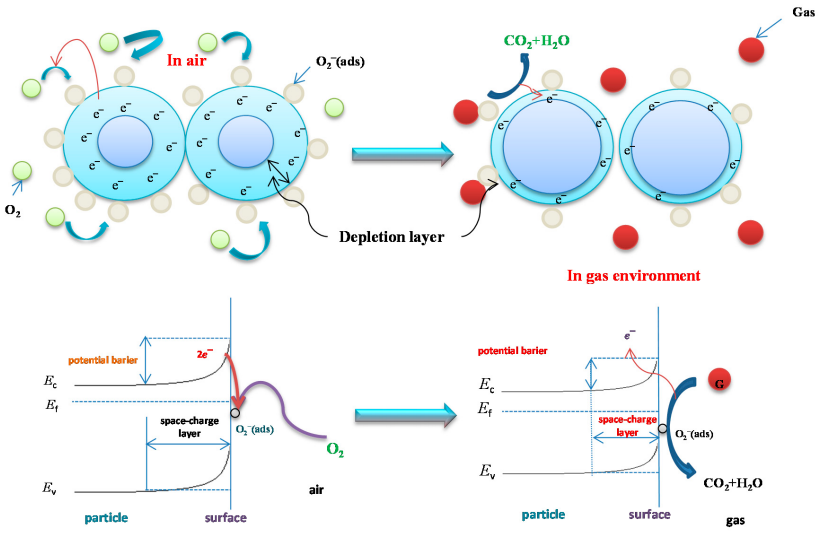

Figure 2.1: Gas sensing mechanism of an n-type semiconductor for a reducing gas [7].

Adsorption/desorption happens at the grains of the semiconductor. Therefore, control over the grain size

is essential in order to achieve optimal sensing performance [8]. Figure 2.2 [9] shows the relation between sensor response and grain size. For grain sizes much larger than twice the depletion width (caused by for instance oxygen adsorption), the grain size has minimal effect on the sensitivity as the depletion region does not overlap with the grains, and the sensitivity mostly depends on the grain boundaries. As the grain size gets smaller than twice the depletion width, the depletion region extends more and more into the grains and the sensitivity increases due to its dependence on the grain size. Having a smaller grain size (and thus a smaller crystallite size) also results in a larger specific surface area [6], which will be beneficial for the sensor response. Smaller grain sizes result in higher porosity which also plays an important role in the response of a gas sensor [10]. Having a large amount of nanopores increases the diffusion rate of gases into the semiconductor film.

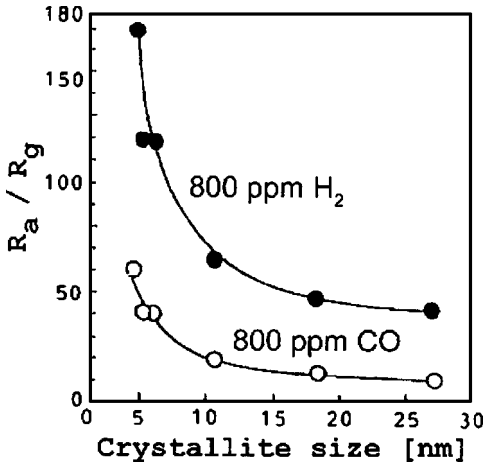

Figure 2.2: Effect of grain size on response of SnO2 nanoparticles for different gases [9].

2.2. Metal Oxides for Gas Sensing

Over decades, metal oxides have been used as sensing layers in gas sensors due to their low cost, ease of development and implementation, chemical sensitivity, and their ability to detect a wide range of gases [6, 11]. Some of the most commonly used metal oxides for gas sensing are tin oxide (SnO_2), zinc oxide (ZnO), copper oxide (CuO), tungsten oxide (WO_3), nickel oxide (NiO) and titanium oxide (TiO_2). A compilation of chemiresistors that use nanoparticles of these metal oxides is shown in table 2.1.

It can be seen in the table that most metal oxide gas sensors operate at elevated temperatures. This is done in order to stimulate the reversibility after gas exposure [2]. In order to maintain stable operation at higher temperatures, metal oxide samples are annealed beforehand. Annealing also increases the purity, conductivity and crystallinity of nanoparticles [12], and may even be required for some metals to oxidize [13].

2.2.1. Tin Oxide

Tin oxide (SnO_2) is by far the most extensively studied metal oxide for gas sensing, as it is a chemically stable n-type semiconductor [7] and has a relatively high sensitivity towards a range of gases, including NO_2, ethanol, ammonia, and H_2. While in some work dopants have been added to SnO_2 as an attempt to improve its electrical conductivity [14], pure SnO_2 has sufficient conductive properties for most gas sensing applications [6, 15–20].

2.2.2. Zinc Oxide

Since the introduction of modern nanotechnology, the usage of zinc oxide (ZnO) for gas sensing has been increasing. While zinc oxide nanoparticles share quite similar characteristics with tin oxide nanoparticles (n-type, wide bandgap, surface conducting), they can be made into a variety of nanostructure morphologies such as nanowires and nanorods to improve the sensing performance [7, 21]. Zinc oxide is sensitive to H_2, NO_2, ethanol, ammonia, and many other gases [6, 22–26].

2.2.3. Copper Oxide

Copper oxide (CuO) is a widely studied p-type semiconductor that is often used for sensing volatile organic compounds, H_2, and NO_2 [6, 27, 28]. Due to holes being the majority carriers in p-type materials, the response of a p-type metal oxide gas sensor such as a CuO sensor is roughly the square root of the response of an identical n-type sensor [8]. However, p-type sensors have better selectivity towards volatile organic compounds and are more tolerant to changes in humidity compared to n-type sensors [7].

Table 2.1: Overview of chemiresistor devices based on metal-oxide semiconductors.

Sensing Material	Fabrication Temp. (°C)	Operating Temp. (°C)	Sensitivity	Target Gas	Nanoparticle Prod. Method	Ref.
Tin Oxide (SnO2)	550	room	$\frac{Ra}{Rg} = 1.015$	1000 ppm ethanol	ACVD	[15]
	300	250	$\frac{Ra}{Rg} = 2.75$	1000 ppm ethanol	Gas-phase condensation	[16]
	-	250	$\frac{Ra}{Rg} = 6$	100 ppm ethanol	Mini-arc plasma	[17]
	700	200	$\frac{Rg}{Ra} = 1.19$	100 ppm NO2	Sol-gel	[18]
	100	room	$\frac{Ra}{Rg} = 4$	25 ppm NH3	Hydrothermal	[19]
	-	400	$\frac{Ra}{Rg} = 1.52$	500 ppm NH3	Hydrothermal	[20]
	-	425	$\frac{Ra}{Rg} = 1.72$	500 ppm ethanol	Hydrothermal	[20]
	500	400	$\frac{Ra}{Rg} = 4$	200 ppm ethanol	Spark ablation	[3]
Zinc Oxide (ZnO)	500	250	$\frac{Ra}{Rg} = 14.4$	50 ppm ethanol	Thermal evaporation	[22]
	500	250	$\frac{Ra}{Rg} = 4.2$	50 ppm ethanol	Simple heat treatment	[22]
	475	370	$\frac{Ra}{Rg} = 25$	1000 ppm ethanol	Sol-gel	[23]
	200	400	$\frac{Ra}{Rg} = 38.87$	250 ppm ethanol	Hydrothermal	[24]
	200	400	$\frac{Ra}{Rg} = 45.75$	250 ppm acetaldehyde	Hydrothermal	[24]
	200	300	$\frac{Rg}{Ra} = 18.42$	100 ppm NO2	Hydrothermal	[24]
	400	290	$\frac{Rg}{Ra} = 230$	40 ppm NO2	SNAS	[25]
	-	300	$\frac{Ra}{Rg} = 1.51$	50 ppm NH3	Drop coating	[26]
Copper Oxide (CuO)	500	250	$\frac{Ra}{Rg} = 1.51$	50 ppm NO2	Thermal decomposition	[27]
	-	220	$\frac{Rg}{Ra} = 5.3$	10 ppm acetone	Sol-gel	[28]
	-	220	$\frac{Rg}{Ra} = 5.9$	10 ppm methanol	Sol-gel	[28]
	-	220	$\frac{Rg}{Ra} = 5.3$	10 ppm ethanol	Sol-gel	[28]
Titanium Oxide (TiO2)	700	300	$\frac{Ra}{Rg} = 10$	3000 ppm H2	Flame spray	[29]
	700	356	$\frac{Ra}{Rg} = 2.9$	8 ppm acetone	Therm. & chem. oxidation	[30]
	800	100	$\frac{Ra}{Rg} = 1.49$	100 ppm ethanol	Sol-gel	[31]
Nickel Oxide (NiO)	500	150	$\frac{Ra}{Rg} = 2.15$	100 ppm ethanol	Microemulsion	[32]
	500	150	$\frac{Ra}{Rg} = 1.2$	500 ppm NH3	Microemulsion	[32]
Tungsten Oxide (WO3)	500	200	$\frac{Rg}{Ra} = 100$	1 ppm NO2	Spark ablation	[33]
	300	200	$\frac{Rg}{Ra} = 250$	1 ppm NO2	Sol-gel	[34]
	800	450	$\frac{Rg}{Ra} = 1.04$	400 ppm NH3	Sol-gel	[35]
	600	400	$\frac{Rg}{Ra} = 9.8$	100 ppm NH3	Vacuum evaporation	[36]

2.2.4. Titanium Oxide

Titanium oxide (TiO_2) is an n-type semiconductor that is also used for gas sensing. Some of the gases that TiO_2 is sensitive to are Cl_2, NO_2, ethanol and many volatile organic compounds [6, 29–31, 37]. TiO_2 is a bulk conductance material, resulting in a much higher operating temperature when used purely compared to that of surface conductance materials such as SnO_2 and ZnO [38]. Other drawbacks of using TiO_2 for gas sensing are low solubility of TiO_2 and instability of TiO_2 films, resulting in lower responses towards gases compared to SnO_2 and ZnO [21]. Therefore, TiO_2 is more often used in combination with dopants or noble metals to improve the sensing performance.

2.2.5. Nickel Oxide

Nickel oxide (NiO) is a p-type semiconductor that is often used to detect toxic gases such as H_2S, NO_2, and various VOCs [6]. However, the response is relatively low when it is used as pure nanoparticles, and is therefore more often combined with metals, dopants, and/or made into a different nanostructure [32].

2.2.6. Tungsten Oxide

Tungsten oxide (WO_3) is an n-type semiconductor that has high sensitivity towards various gases, similar to SnO_2 and ZnO. The main difference is in the selectivity towards certain gases, as the semiconductors are sensitive towards slightly different ranges of gases. WO_3 has high sensitivity towards NO_2 and H_2S, but slightly lower sensitivity towards ammonia compared to SnO_2 and ZnO nanoparticles [6, 33–35].

2.3. Nanoparticle Production Methods

Various methods exist that aim to produce well-defined, stable nanoparticles, and each method has its advantages that could be useful in different fields of application. This section reviews some of the most commonly used methods that are applicable for gas sensing purposes, i.e. methods that can provide structurally stable nanoparticles on solid surfaces.

2.3.1. Sol-gel

One of the most widely used methods for the synthesis of metal oxide nanoparticles is the sol-gel method. It is a bottom-up approach, meaning that the starting products are at molecular or atomic level and the end products are nanoparticles [39]. Sol-gel is done by first mixing precursors such as metal alkoxides in a liquid, performing hydrolysis to form a solvent (sol), followed by a condensation step resulting in the formation of metal oxide linkages and an increase in the viscosity resulting in the sol becoming a gel [40]. Polycondensation continues during an aging process afterwards, during which porosity decreases and the thickness between colloidal particles increases. After drying and calcination, nanoparticles are achieved.

Some of the advantages of the sol-gel method are the control over porosity during the aging and calcination steps, low processing temperature, and the scalability of the process [41]. Some of the disadvantages are the relatively longer reaction time and liquids being involved which may affect the purity.

2.3.2. Hydrothermal

Hydrothermal synthesis is another widely used technique for generating metal oxide nanoparticles [42]. The synthesis is done by chemical reactions in a sealed reactor at an elevated temperature and pressure. When the solvent is an organic instead of water, the method is referred to as "solvothermal synthesis". Inside the heated reactor, one end has a higher temperature than the other end. Nutrients get dissolved due to the hotter end and get added to the nanostructure due to the colder end. Metal oxide nanoparticles are usually synthesized in two steps: formation of metal hydroxides via a hydrolysis process and formation of metal oxides via a condensation reaction.

The main advantage of the hydrothermal method is controllability of particle size and morphology due to processing variables such as temperature, pH and additives. Disadvantages are the need for high temperatures and pressures, possibly high costs of autoclaves, limited purity (if organic solvents are used instead of water) and the impossibility of observing the synthesis process if the autoclave is not transparent.

2.3.3. Microemulsion

The oil-in-water microemulsion method is used for synthesis of metal and metal oxide nanoparticles with controlled size and shape [43]. Within a microemulsion, water and an oil that contains reactants coexist in one phase due to a surfactant. Nanoparticles are synthesized by combining multiple microemulsions, after which a reactant exchange takes place at the nanoscale and particles are formed.

The microemulsion synthesis allows generation of nanoparticles at room temperature. The presence of surfactants also provide protection to generated nanoparticles from agglomeration. Some disadvantages of the method are instability of microemulsions at different temperatures and pH levels, and solubility issues when substances with high melting points are used.

2.3.4. Laser Ablation

Laser ablation is a method that is used for generating nanoparticles from solid materials [44]. A powerful laser beam hits a surface of the target material, vaporizes it and results in formation of nanoparticles. The method allows tuning of nanoparticle size and distribution by adjustment of laser wavelength and fluence. Compared to commonly used nanoparticle generation methods such as the previously mentioned sol-gel method, laser ablation is able to produce nanoparticles at relatively high purity because of no liquid solvents being involved. However, the production costs are higher and the scalability suffers as the method requires the use of a powerful laser.

2.3.5. Spark Ablation

Spark ablation is a versatile technique for generating nanoparticles. It offers flexibility regarding size and composition of the materials [4]. Generation of nanoparticles is achieved by ablation of bulk materials, as is also the case with the laser ablation method. Electrodes that consist of the desired material for the particles to be generated are placed close to each other with a narrow gap in between. Sparks consisting of plasma are generated between the gap repeatedly, after which spots on the electrode are heated beyond the boiling point and become nanoparticles. An inert gas, usually nitrogen or argon, carries the formed particles away.

Spark ablation also allows mixing of different metals on the nanoscale. This can be achieved by having two different elemental electrodes, or two identical electrodes that are already alloyed [4].

Spark ablated nanoparticles have a relatively high purity because of the same reasons that were mentioned before for the laser ablation method [45]. However, compared to the laser ablation method, the costs for producing particles are lower and the scalability is better because of the need for a powerful laser being eliminated [46].

2.4. Electrodes for Gas Sensors

Most semiconductor gas sensors have a two-electrode type configuration in which the sensing semiconductor is placed between two metal electrodes [47]. Figure 2.3 shows an example of a two-electrode type chemiresistor configuration. Most electrodes used for gas sensors have an interdigitated geometry since it allows for a wide contact area and for the deposition of the sensing material directly on top of it without etching, as etching could potentially damage the sensing layer. The width of the electrode fingers and the gap between the two electrodes also affect the sensitivity of the sensor. If the gap is narrow, the current will flow through smaller areas of the sensing layer directly on top of the electrodes, resulting in smaller but more responsive spots. Increasing the gap width will result in the current spreading horizontally and vertically through the sensing layer, resulting in a larger sensing area that will be relatively less responsive to gases. It is found that wider gaps increase the sensitivity towards gases that are highly reactive with the sensing material, while narrower gaps increase the sensitivity towards less-reactive gases [48, 49].

While the interdigitated structure is the most often used layout for gas sensors, other types of electrode geometries also exist. Examples of these are the compressed pellet [49] and the one-electrode geometry [47]. The compressed pellet geometry shown in figure 2.4a is obtained by sintering a tablet consisting of a sensing material and forming electrodes on each side. Such a configuration does not offer the large contact area, ease of fabrication and flexibility regarding electrode width and gap that the interdigitated configuration does.

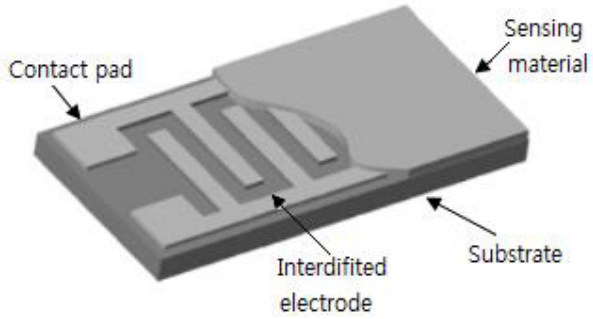

Figure 2.3: A chemiresistor configuration with two interdigitated electrodes [47].

The one-electrode geometry shown in figure 2.4b may offer the mentioned advantages as the sensing layer can be deposited directly on top of the electrode, and the thickness and meander dimensions of the electrode can affect the sensitivity of the sensor similar to the interdigitated geometry. However, such a device requires impedance matching between the sensing layer and the electrode, which takes away from the freedom to adjust the electrode dimensions as they depend on the impedance of the sensing layer.

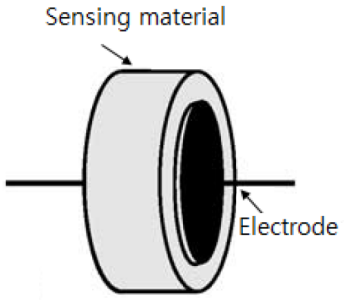

(a) Compressed pellet structure.

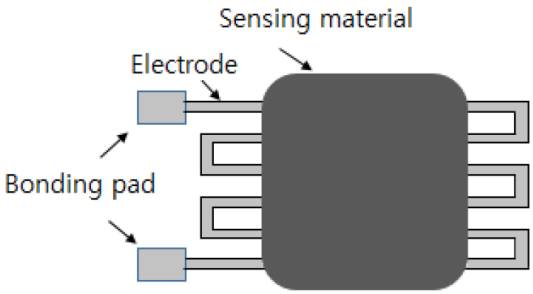

(b) One-electrode configuration.

Figure 2.4: Less often used electrode geometries (compared to the interdigitated structure in figure 2.3) for gas sensors [49] [47].

Materials that are most often used for electrodes in gas sensors are silver, gold and platinum. Silver is the least expensive material among those, but is often not suitable for long-term use due to degradation at higher temperatures. Gold has relatively high conductivity and stability, but can diffuse into silicon substrates and has poor adhesion to silicon. Platinum has the highest stability with little degradation over time, but it is more expensive and has similar adhesion issues as gold.

In order to counter adhesion issues of electrode materials, in many gas sensor designs the electrode is deposited on top of an adhesion layer [50]. This is often a layer of chromium [15, 37] or titanium [16, 26]. In many other cases, alumina [32, 35, 51, 52] is used as substrate instead of silicon which can eliminate the need for an adhesion layer.

2.5. ChemFETs

Most commercial metal oxide gas sensors are chemiresistors [2, 53]. These are two-terminal devices with which gas sensing is done by monitoring the change in resistance of the metal oxide. The main advantage of the chemiresistor is its simplicity of fabrication and operation. Drawbacks are low sensitivity and poor reversibility after gas exposure.

As worthwhile alternatives to the chemiresistor, chemFETs are introduced. ChemFETs are three-terminal devices that can sense chemicals. A chemFET that uses a metal oxide as its sensing layer has been introduced by Andringa et al (2014) [2]. The device is a back-gate chemFET, shown in figure 2.5. This structure is quite

similar to the chemiresistor except for the fact that an additional gate is present. The substrate underneath is used as the gate terminal which is insulated by a dielectric oxide layer and thus forms a parallel plate capacitor with the sensing semiconductor on top. The electrode geometry of such devices is usually interdigitated, similar to most chemiresistors as described in section 2.4. As seen in figure 2.5, applying a gate voltage results in charge getting trapped, resulting in a shift in the threshold voltage.

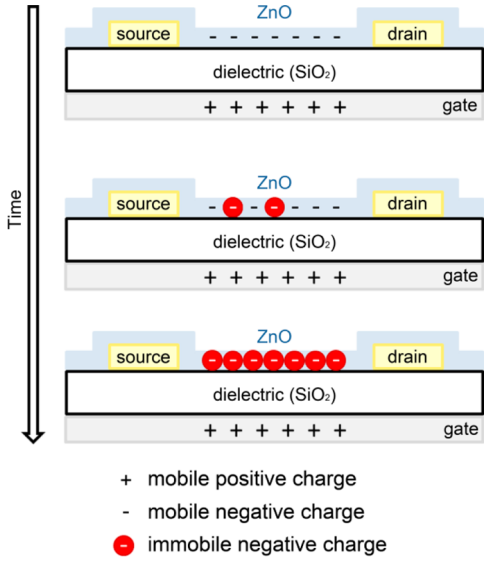

Figure 2.5: Charge trapping process of a back-gate zinc oxide chemFET [2].

The main advantage of the chemFET over the chemiresistor is the ability to amplify the response using the gate terminal. If a positive voltage is applied to the gate, charge carriers get accumulated (if the semiconductor is n-type) and the current flowing through the semiconductor increases. The current gets noticeably large for voltages higher than the threshold voltage of the device. This gives the freedom to modulate the charge carrier density in the semiconductor, which can result in more charge carriers to react with a gas, and thus a higher sensing response. A transfer curve showing the effect of gate biasing is given in figure 2.6.

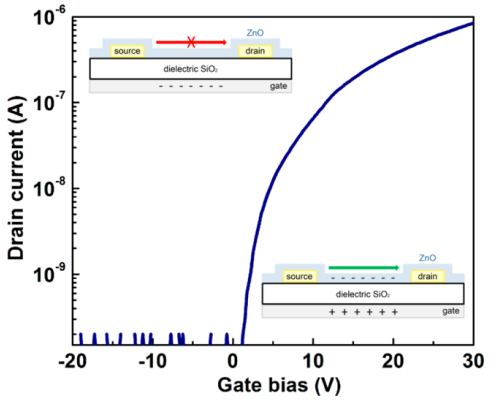

Figure 2.6: Transfer curve of a back-gate zinc oxide chemFET [2].

Gas detection with this structure can be related to the magnitude of the shift in the threshold voltage. The threshold voltage slowly shifts towards the applied gate voltage and shifts faster over time in the presence of a gas (in this case NO_2). This phenomenon is illustrated in figure 2.7.

As mentioned in section2.2, the recovery of metal oxide gas sensors, i.e. the release of charge carriers from traps is highly influenced by temperature. Therefore, in order to continue to use the sensor repeatedly, the operating temperature would need to be elevated and the gate bias should be switched off. As can be seen

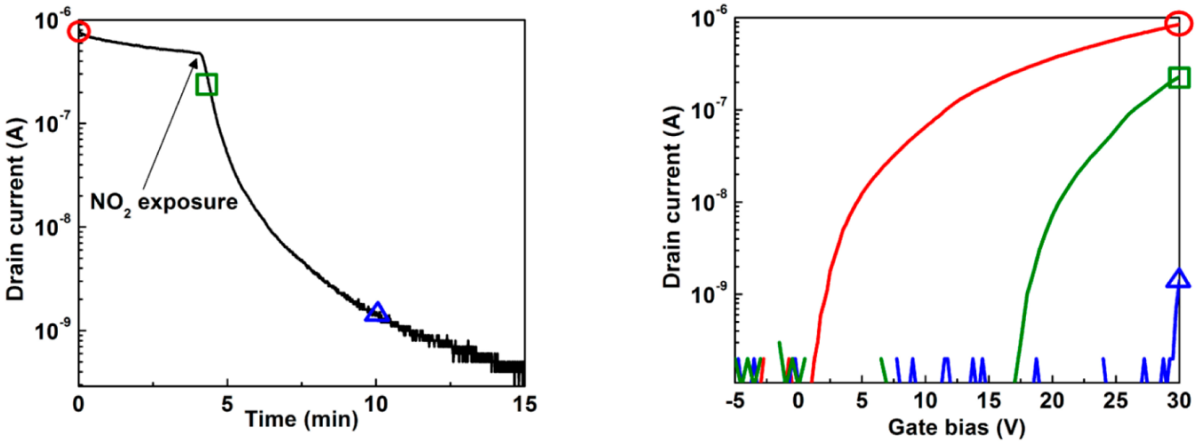

(a) (b)

Figure 2.7: The threshold voltage of a ZnO back-gate chemFET shifts depending on the applied gate bias and NO_2 exposure [2]. The colors red, green and blue in both figures indicate similar conditions, meaning that in (b) the red curve is measured in vacuum, the green curve is measured shortly after 250 ppb of NO_2 is admitted, and the blue curve is measured 6 minutes after the admission of 250 ppb of NO_2.

in figure 2.8, the threshold voltage only reverts back at an elevated temperature. The amount of detected gas can be read out from the amount of shift in the threshold voltage.

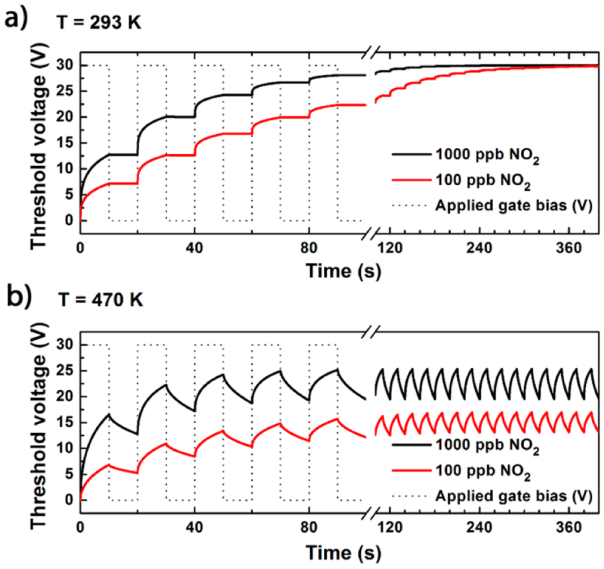

Figure 2.8: Comparison of the threshold voltage shift of a ZnO back-gate chemFET sensing NO2 at room temperature and at 470K [2].

Sensing by continuously calculating the threshold voltage can be make it impractical to measure gas in real-time. In other literature, the amount of gas is often read out by monitoring the shift in the drain current [54, 55].

The sensing-gate chemFET is another transistor structure that is used for gas sensing. It is mostly used for chemFETs for which an organic semiconductor or a noble metal is used as sensing material [56]. A comparison of the sensing-gate and back-gate FET is shown in figure 2.9 (with organic instead of metal oxide semiconductors).

A major difference between the two structures is in the number of elements the current passes through during operation. For the sensing-gate structure, the current passes through the buried drain, substrate and the

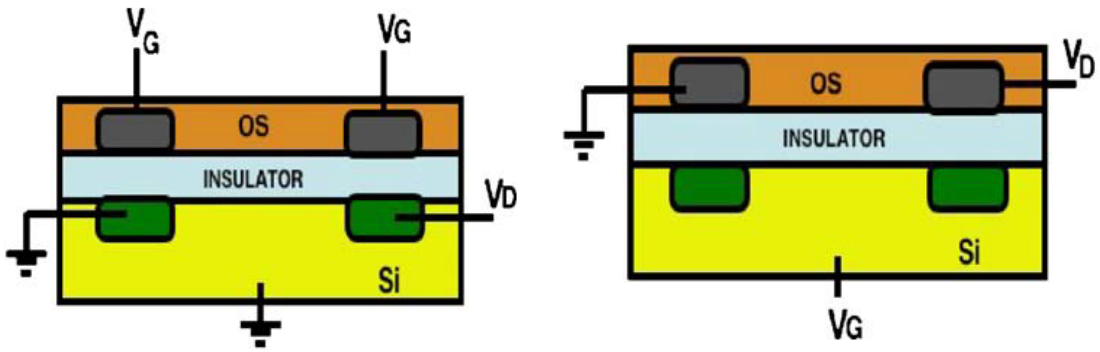

(a) (b)

Figure 2.9: Comparison of (a) a sensing-gate chemFET and (b) a back-gate chemFET [56].

source, and does not pass through any material exposed to the gas containing environment. For the back-gate chemFET structure, however, it passes through two exposed electrodes and the sensing semiconductor. Because it passes through three materials for which a change in work function due to the gas can occur, it may have more selectivity issues compared to the sensing-gate FET. The sensing layer that is used also needs to have sufficient conductivity for the current to pass through it (which is the case for most metal oxides). The sensitivity of the sensing-gate FET is said to be lower [57]. This is mostly attributed in literature to organic transistors having large threshold voltages. At the moment, there is no literature available in which a metal oxide is used on a sensing-gate structure.

2.6. Conclusion

Metal oxide semiconductors offer high sensitivity, high practicality, and low costs when applied on resistive gas sensors. They are often categorized as n-type and p-type semiconductors. The gas sensing mechanism works in an opposite way for n-type and p-type semiconductors, where an oxidizing gas increases the electrical resistance of an n-type semiconductor and reduces it of a p-type semiconductor. A reducing gas reduces and increases the resistance of n-type and p-type semiconductors respectively.

Metal oxides used as gas sensing materials are often used in the form of nanoparticles as that increases the specific surface area for reactions to take place. Several methods exist for generating metal oxide nanoparticles, of which sol-gel and hydrothermal are some of the most commonly used methods. Newer methods such as laser ablation and spark ablation offer advantages such as higher nanoparticle purity and control over composition.

In order to have a large electrode contact area and thus a low contact resistance, resistive gas sensors usually have interdigitated electrodes, with wide or narrow gaps in between, depending on the type of reaction occurring between the gas and the sensing material. In order to amplify the sensing response more, a third terminal can be added to the device, making it a field effect transistor. The added terminal, separated by an insulator, will act as the gate and may stimulate the charge transfer during operation. Potential future work is the use of metal oxides as the gate instead of the substrate of the sensing devices to improve their selectivity towards gases.

3

Methods

This chapter describes the methods used in this thesis for nanoparticle layer synthesis, characterization, and measurement that are put into practice in chapter 6. Furthermore it gives an overview of the gas sensing setup that is used to test the behavior of finalized devices during exposure to target gases, for which the results are provided in chapter 7.

3.1. Nanoparticle Synthesis

In this work, the VSP-G1 Nanoparticle Generator by VSPARTICLE [58] has been used for the generation of metal oxide nanoparticles. The setup generates particles using the spark ablation method covered in section 2.3.5. Two metallic electrodes are placed close to each other and are connected to a power supply and a capacitor as shown in the schematic in figure 3.1. A spark occurs between the electrodes when the capacitor discharges at breakdown voltages, vaporizing the electrode material [46]. A chemically inert or noble gas such as nitrogen or argon carries the vaporized nanoparticles to a nozzle in a vacuum chamber, after which they can be printed on a sample. Patterns are printed using scripts that define the movement of the nozzle using an XYZ-stage. Using a camera attached to the nozzle and visual alignment, a certain printing accuracy can be achieved. Parameters that affect the thickness of the deposited layer are the nozzle size, distance of the nozzle from the substrate, ablation power, movement speed and printing repetitions. The VSP-G1 nanoprinter is shown in figure 3.2, with the spark generator and the printing chamber highlighted.

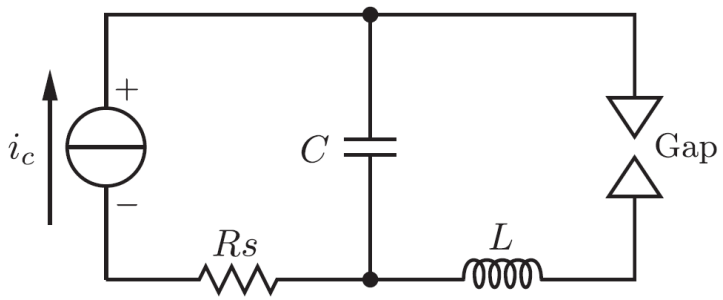

Figure 3.1: Simplified circuit of a classical spark ablation nanoparticle generator [46].

The voltage and current of the spark determine the ablation power. A larger current can provide a higher deposition rate, but can bring instability with it. Figure 3.3 shows that there is a limit for the spark current after which the spark mode enters the glow mode, in which no ablation occurs [4]. Close to the limit the spark tends to get unstable. Therefore, the voltage and current should be set such that stability and uniformity during deposition is maintained.

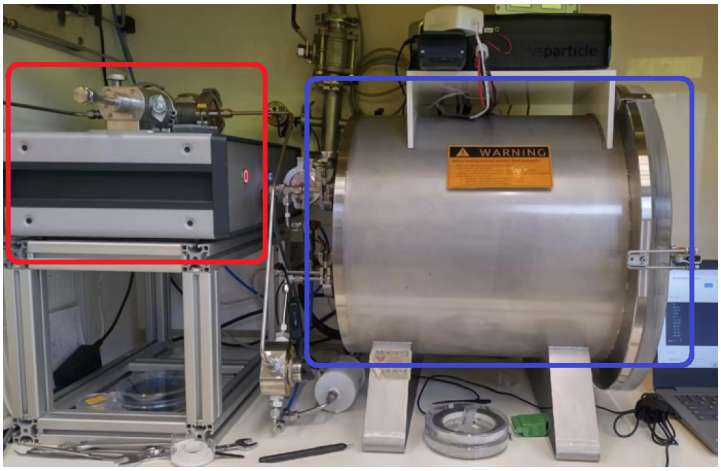

Figure 3.2: VSP-G1 nanoparticle generator by VSPARTICLE used in this study to produce sensing layers, consisting of the spark generator (red) and the printing chamber (blue).

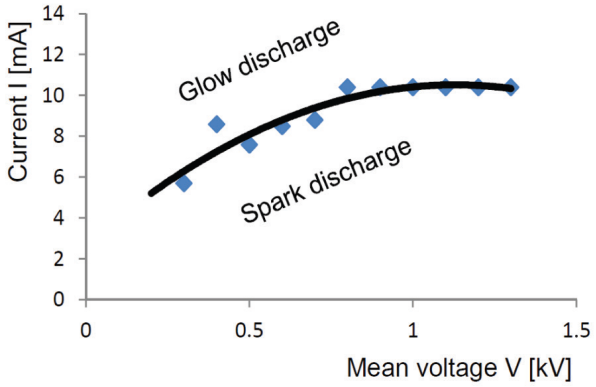

Figure 3.3: Spark discharge limit for VSPARTICLE G1 with nitrogen as carrier gas [4].

3.2. Nanoparticle Characterization Methods

Numerous methods exist that can be used to inspect the (deviations in) properties and composition of printed nanoparticles [59]. Inspection techniques could be categorized as on-line and off-line techniques [4]. On-line analysis happens during the production of particles and is integrated into the generation chamber. The main advantage of this is that analysis is done in the same gas atmosphere. Off-line analysis happens after deposition and is often done in a different atmosphere which may affect the accuracy of analysis. However, because samples will only be operated in atmosphere during this project, the focus will be on off-line methods due to their practicality.

3.2.1. Scanning Electron Microscopy

Scanning electron microscopy (SEM) is used for obtaining visual images containing information about the surface of samples [60]. Similar to other electron microscopy methods, SEM images are obtained by sending an electron beam towards the sample. Figure 3.4 illustrates the different signals that form when an electron beam comes in contact with a sample [4]. Many of these signals are used for different inspection techniques. SEM uses the SE (secondary electrons) and BE (backscatter electrons) signals to form an image. SEs are low energy electrons that return from the surface of the sample and contain high resolution information of the surface topology. BEs have a higher energy compared to SEs, travel deeper into the sample, and contain lower resolution information of the composition. SEM can achieve image resolutions smaller than 1 nanometer. Information about the surface of samples is particularly relevant in this project as gas sensing behavior is dependent on interaction spots at the surface of nanoparticles.

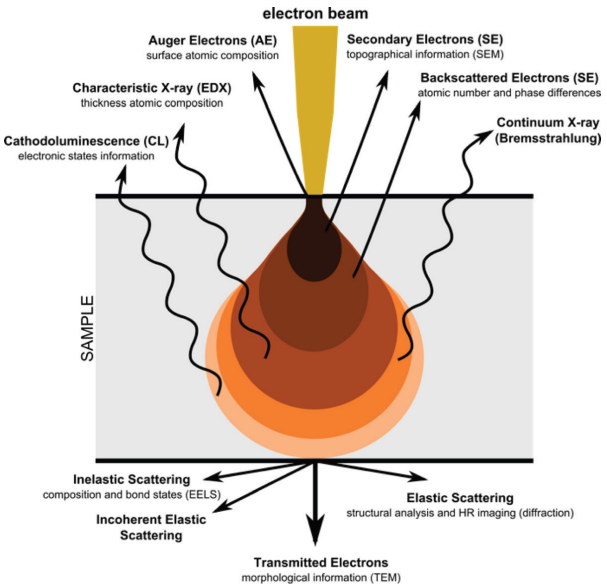

Figure 3.4: Signals formed during interaction between an electron beam and a sample [4].

3.2.2. Energy Dispersive X-Ray Spectroscopy

Energy dispersive x-ray spectroscopy (EDX) is a method used for detecting the elements that are present on a sample [61]. Similar to the SEM method described previously and as illustrated in figure 3.4, EDX uses an electron beam pointed towards the to-be-examined sample. The incident beam makes electrons eject from the shells surrounding the atoms on the sample. Electrons from higher energy shells replace the ejected electrons. The resulting difference in energy is released in the form of an x-ray. The energy of the x-ray gives an indication of the atomic structure. Using an energy dispersive spectrometer, the emitted x-rays are measured and elements present on the sample are found.

One limitation of EDX is its inability to detect phases of detected elements. As an example relevant to this work, on a sample containing tin oxide nanoparticles, EDX would be able to detect Sn and O atoms that are present, but it would not be able to detect whether the tin oxide pairs are SnO or SnO_2. However, atomic concentrations obtained from EDX data can provide an indication.

3.2.3. X-Ray Diffraction

X-ray diffraction (XRD) is a method used for determining the molecular structure of crystalline samples [4]. It uses a beam of x-rays directed onto the to-be-measured specimen. The x-rays are diffracted at the planes of crystalline structures into different directions. These diffracted rays may either add up in intensity or cancel each other out, depending on their phase difference. The detected intensities and their phases are plotted on a spectrum from which the molecular structures that are present can be identified from the resulting peaks.

XRD gives the clearest results for purely crystalline samples. However, aerosol nanoparticles that get deposited are usually randomly oriented. This could give lower or broader peaks on the spectrum, making it more difficult to analyze the contents of the sample. Annealing nanoparticles is known to improve the crystallinity of nanostructures as explained in section 2.2, and could therefore improve the results of XRD inspection.

3.3. Conductivity Measurement

In this work, the conductivity measurements on sensing devices are performed in order to confirm that they are suitable for gas sensing. This is done with the Cascade Summit 12000 probe station in combination with the HP 4156C Precision Semiconductor Parameter Analyzer. The probe system is shown in figure 3.5 has 6 probe needles that can apply and measure voltage and current. Measurments are performed in atmosphere and the chuck temperature can be adjusted between -40 $°C$ and 200 $°C$. The amount of available probe needles also allows for biasing and transmission line measurements (TLM), a method used for determining the

contact resistance between a metal and a semiconductor.

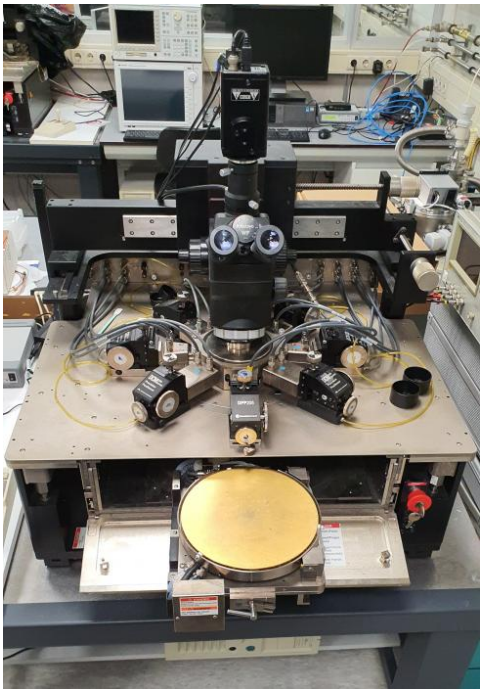

Figure 3.5: The Cascade Summit 12000 probe station used for conductivity measurements in atmosphere [62].

3.4. Gas Sensing Setup

For the generation and control of gas flows, a modular system consisting of the three Owlstone vapor generators [63] shown in figure 3.6 is used. The target gas is generated by the OVG-4 calibration gas generator (figure 3.6a) by heating up a permeation tube that contains the analyte of interest. The analyte then permeates through the tube at a rate depending on the temperature. By adjusting the sample flow and exhaust flow according to a calibrated permeation rate provided with the tube, the concentration of the target gas can be set. The OHG-4 humidity generator (figure 3.6b) is able to produce relative humidity concentrations between 1% and 99% (±1%) and is useful for testing the sensitivity of devices towards different concentrations of humidity. The OFC-1 flow controller (figure 3.6c) sets the flow of pure N_2 gas and can be used for additional dilution to reduce target gas or humidity concentrations even more, or to flush the other gases away to stimulate device recovery.

(a) Calibration gas generator. (b) Humidity generator. (c) Flow controller.

Figure 3.6: Owlstone vapor generators [63] used for controlling the flow/concentration of a target gas (a), flow/concentration of humidity (b), and the flow of nitrogen (c).

Another part of the gas sensing setup is a chamber in which the gas from the vapor generators flows through a shower head onto the to-be-tested die. The chamber contains 50 pins can be used as voltage/current sources or to perform voltage, current or resistance measurements. The chamber is designed for dice of 20x20mm with contact pads aligned according to the pins. As mentioned in chapter 2, metal oxide gas sensors usually need to be operated at elevated temperatures to recover. To achieve that, a hotplate is present in the chamber on which the die is placed.

Sourcing and measuring through the pins is done using the Keithley 2612B source measure unit [64], which is able to provide a voltage up to 200V and a current up to 10A. It can perform two-point and four-point measurements and can measure resistances between 500 $n\Omega$ and 100 $T\Omega$. The devices are measured sequentially and the switching is done using the Keysight 34970A data acquisition/data logger switch unit with a Keysight 34901A multiplexer module in one of its slots. The multiplexer module has 20 channels to which the pins of the sensing chamber are wired. Measurements can therefore be performed on 20 devices simultaneously if 2-point measurements are performed, and rewiring has to be done if other devices need to be measured.

4

Design of Gas Sensors

For this project, 2 die designs of 20x20mm are made using the software L-Edit [65], and both are applied for studying different device properties that can affect gas sensitivity. The total area of the dice is chosen according to the limitations of the gas sensing setup. The two designs, referred to as design A and design B, are made using 3 masks. In this chapter, the devices and test structures that are present on each design will first be covered in general. Then the purpose of each mask and the layout of the designs will be explained.

4.1. Devices

As described in chapter 3, the gas sensing setup allows for a total of 50 contact pads on a die to perform measurements on. Both designs have a total of 24 interdigitated electrode pairs each. Their structure is similar to the back-gate chemFET device covered in section 2.5. The silicon substrate is used as the gate, on which a silicon dioxide layer is deposited as the gate insulator. Interdigitated gold electrodes are placed on top of the oxide layer acting as source and drain, on which a gas sensitive metal oxide nanoparticle layer is meant to be deposited. A typical design of a back-gate chemFET is shown in figure 4.1a, showing an interdigitated electrode pair and an opening of an outer passivation layer on top of it. Figure 4.1b shows the cross section of a pair of electrode fingers of a device. The way the measurements are performed on these devices is schematically shown in figure 4.2, which applies for both the cascade system and the gas setup covered in chapter 3. The dimensions of the electrodes per device differ and are shown later in tables 4.3 and 4.4. The geometries are made to differ in order to be able to study the effect of electrode width and gap size on the gas sensitivity, as it was mentioned in chapter 2 that wider or narrower electrodes or gaps can provide a higher or lower sensitivity, depending on the gas and the sensing material.

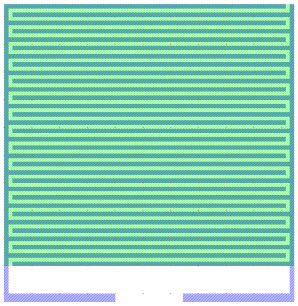

(a) Top-view of an interdigitated electrode pair (blue) and an opening in the outermost passivation layer (green) on top of it.

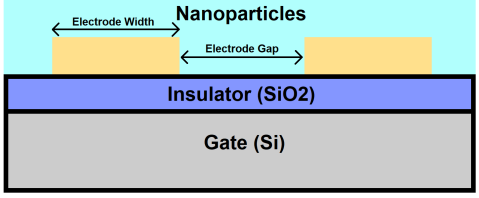

(b) Cross section of a pair of interdigitated electrode fingers on a device.

Figure 4.1: The design of interdigitated electrodes.

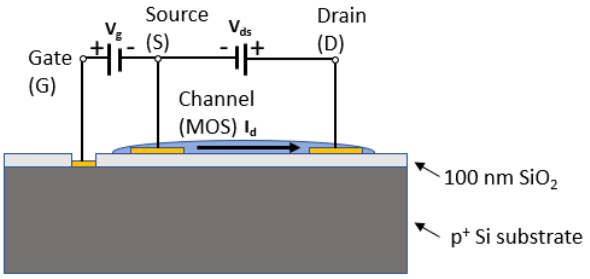

Figure 4.2: Device conductance measurement layout.

4.2. Test Structures

Besides the sensing devices, both designs also contain 2 types of TLM structures for performing resistance measurements on nanoparticle layers. Figure 4.3a shows a TLM structure with differing spacings between electrodes, with which a value for the sheet resistance of the nanoparticle layer can be obtained. Figure 4.3a shows a similar TLM structure, but with spacings that are identical, which can be used for checking for uniformity issues over a printed line by measuring over the same distance. The width of the spacings between the electrodes shown in figures 4.3a and 4.3b are provided in the tables 4.1 and 4.2 respectively. Each electrode has contact pads of $50x50\mu m$ and a line width of $10\mu m$.

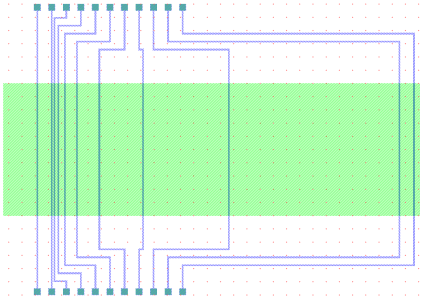

(a) Differing spacings between electrodes.

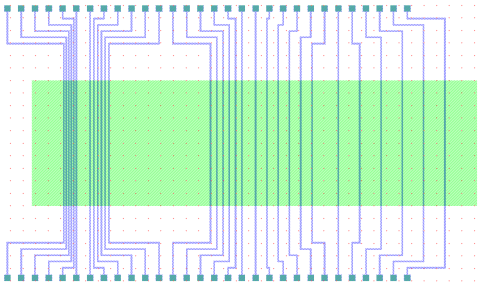

(b) Repeated identical spacings between electrodes.

Figure 4.3: Design of TLM test structures with electrodes (blue) and openings in the outermost passivation layer (green).

Table 4.1: Electrode spacing widths of the TLM structure with differing spacings shown in figure 4.3a from left to right (except for the most left and most right spacings which are $100\mu m$).

Electrode pair	Spacing width [μm]
1	10
2	20
3	40
4	80
5	160
6	320
7	640
8	1280

Table 4.2: Electrode spacing widths of the test structure with repeating identical spacings shown in figure 4.3b from left to right.

Compound of 6 electrodes	Spacing width
1	10
2	20
3	40
4	80
5	160

4.3. Mask 1: Substrate Contacts

Mask 1 is used for making 400x400 μm contact holes through the oxide layer that is used as the gate insulator. Each design has two of such contact holes that are needed for biasing the silicon substrate that is used as the gate of FETs. The mask's polarity is dark field and will be used with positive photoresist followed by plasma etching (steps described in chapter 5). The mask requires a resolution of at least 10 μm and is thus ordered

as a foil mask.

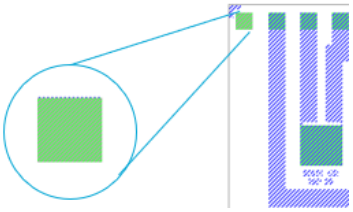

Figure 4.4: One of the two 400x400 μm substrate contacts of a design, patterned using mask 1.

4.4. Mask 2: Metalization

Mask 2 is used for patterning metal wires and the electrodes shown previously in the figures 4.1a, 4.3a and 4.3b in blue. It requires a resolution of at least 2 μm, and is thus ordered as a glass mask. The polarity is bright field and the mask is meant to be used with negative photoresist and lift-off.

4.5. Mask 3: Passivation

The third mask is used for openings in the outer passivation oxide layer that are shown in the figures 4.1a, 4.3a and 4.3b in green. The openings define the areas at which nanoparticle layers are meant to be deposited. The polarity is dark field and patterning will be done by application of positive photoresist followed by wet etching. The mask requires a resolution of at least 10μm and is thus ordered as a foil mask.

4.6. Design A

Design A contains 24 chemFETs with electrodes that have different dimensions from each. This design is meant for studying the effects that electrode specifications, such as finger/gap width and contact area have on gas sensitivity. Table 4.3 contains the specifications of each electrode pair present in design A (figure 4.5a). Identical L/W ratios or contact areas have been highlighted with colors in the table. Such devices with an identical ratio or contact area can be useful determining the effect of contact resistance, by for example testing whether a device with larger contact area but similar L/W ratio gives a larger response towards a gas.

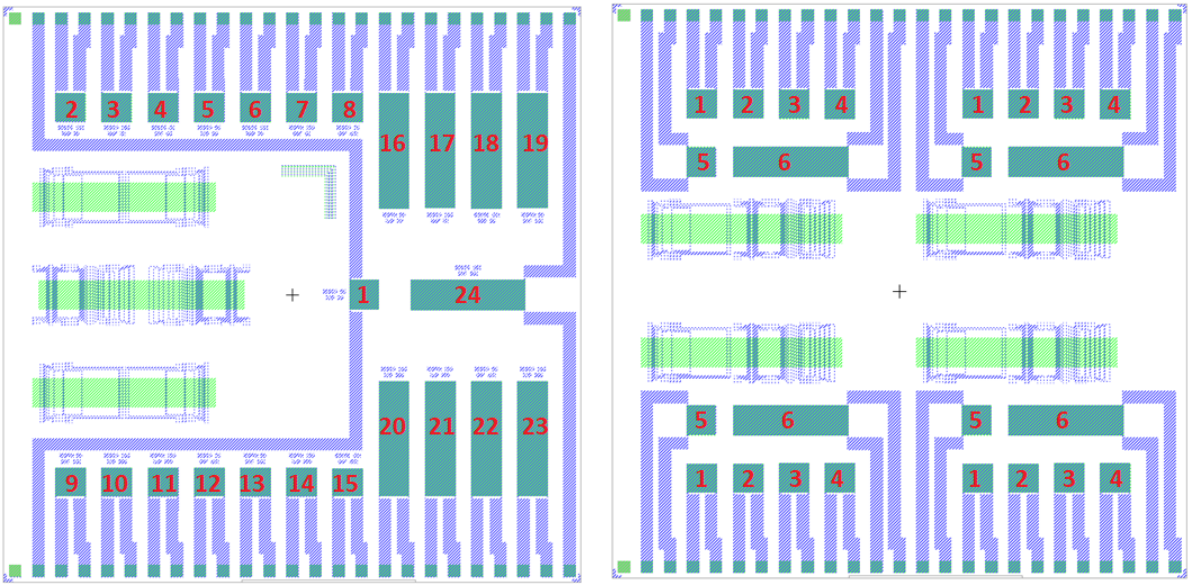

(a) Design A

(b) Design B

Figure 4.5: Layouts of design A and design B.

Table 4.3: Specifications of sensing device electrodes present in design A.

Electrode pair	Finger width [µm]	Finger gap [µm]	Finger length [mm]	Total width [mm]	Fingers per electrode	L/W	Area per electrode [mm2]
1	5	2	1	1	71	2.82E-05	0.355
2	10	2	1	1	41	4.88E-05	0.41
3	15	2	1	1	29	6.90E-05	0.435
4	2	5	1	1	71	7.04E-05	0.142
5	5	5	1	1	50	1.00E-04	0.25
6	10	5	1	1	33	1.52E-04	0.33
7	15	5	1	1	25	2.00E-04	0.375
8	2	10	1	1	42	2.38E-04	0.084
9	5	10	1	1	33	3.03E-04	0.165
10	10	10	1	1	25	4.00E-04	0.25
11	15	10	1	1	20	5.00E-04	0.3
12	2	15	1	1	29	5.17E-04	0.058
13	5	15	1	1	25	6.00E-04	0.125
14	10	15	1	1	20	7.50E-04	0.2
15	15	15	1	1	16	9.38E-04	0.24
16	5	5	1	4	200	2.50E-05	1
17	10	5	1	4	133	3.76E-05	1.33
18	15	5	1	4	100	5.00E-05	1.5
19	5	10	1	4	133	7.52E-05	0.665
20	10	10	1	4	100	1.00E-04	1
21	15	10	1	4	80	1.25E-04	1.2
22	5	15	1	4	100	1.50E-04	0.5
23	10	15	1	4	80	1.88E-04	0.8
24	15	15	1	4	66	2.27E-04	0.99

Table 4.4: Specifications of sensing device electrodes present in design B.

Electrode pair	Finger width [µm]	Finger gap [µm]	Finger length [mm]	Total width [mm]	Fingers per electrode	L/W	Area per electrode [mm2]
1	10	2	1	1	41	4.88E-05	0.41
2	2	5	1	1	71	7.04E-05	0.142
3	5	5	1	1	50	1.00E-04	0.25
4	2	10	1	1	42	2.38E-04	0.084
5	5	2	1	1	71	2.82E-05	0.355
6	5	5	1	4	200	2.50E-05	1

4.7. Design B

Design B contains four identical quarters as shown in figure 4.5b. The specifications of the electrodes of the chemFETs present in each quarter are shown in table 4.4. This design is meant for comparison of sensing performance of different sensing materials when printed on similar devices.

5

Device Fabrication

This chapter goes through the fabrication steps for obtaining the devices of which the designs were shown previously in chapter 4. The fabrication process is started with five 4-inch p-doped silicon wafers. A schematic overview of the processing steps is shown in figure 5.1. The steps can be summarized as follows: an insulating oxide layer is applied to the silicon wafers using thermal oxidation (figure 5.1b), after which bias openings are etched into it towards the silicon substrate (figure 5.1c). A negative photoresist layer is applied and patterned (figure 5.1d), followed by a deposition of gold (figure 5.1e). Using the lift-off technique, the photoresist is removed together with parts of the gold layer, after which patterns of gold electrodes remain (figure 5.1f). Finally a passivating oxide layer is deposited and openings are etched into it (figures 5.1g and 5.1h). The following sections in this chapter describe these fabrication steps in more detail.

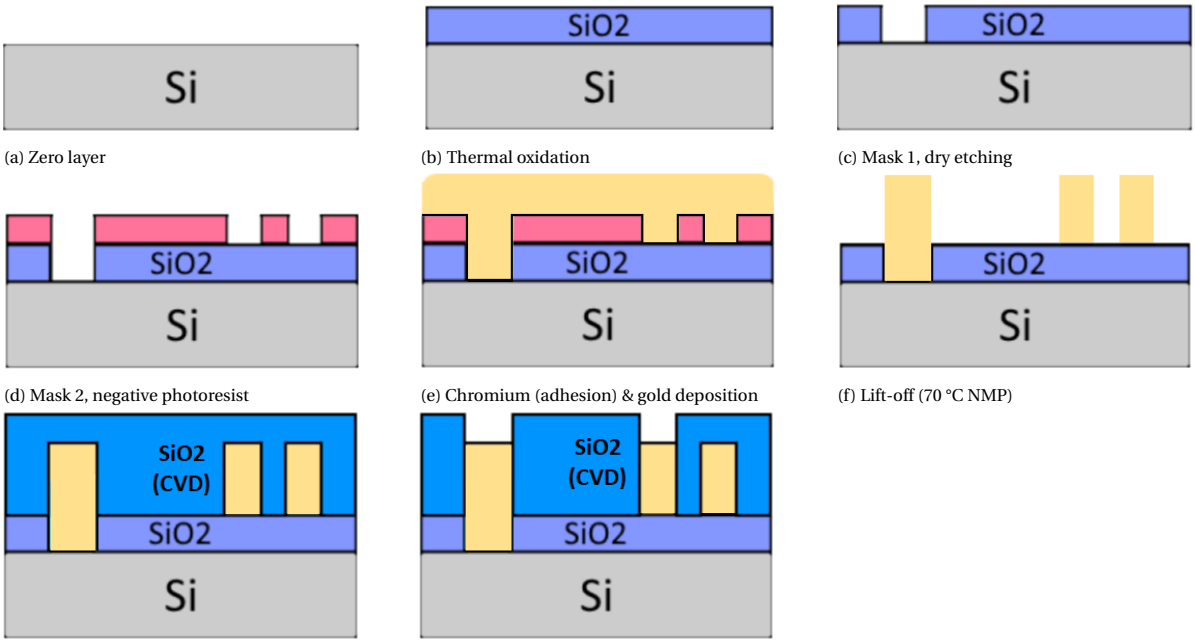

(a) Zero layer

(b) Thermal oxidation

(c) Mask 1, dry etching

(d) Mask 2, negative photoresist

(e) Chromium (adhesion) & gold deposition

(f) Lift-off (70 °C NMP)

(g) CVD silicon dioxide

(h) Mask 3, BHF(1:7) etching

Figure 5.1: Schematic overview of fabrication steps.

5.1. Thermal Oxide Formation

Thermal oxidation is applied to 5 wafers using a tube furnace operating at 1000 °C. The desired oxide thickness is 100nm. The required oxidation time is calculated using the Deal & Grove model [66]. For wet oxidation the required time is calculated to be 10 minutes and 4 seconds. The steps of the oxidation program are pro-

vided in table 5.1.

Table 5.1: Furnace C1; Program name: WET1000

PROCESS	TEMPERATURE (in °C)	GASES & FLOWS (in liter/min)	TIME (in minutes)	REMARKS
boat in	600	nitrogen: 6.0	5	
stabilize	600	nitrogen: 6.0	10	
anneal	600	nitrogen: 6.0	15	
heat up	+10 °C/min	nitrogen: 3.0 oxygen: 0.3	40	
stabilize	1000	nitrogen: 3.0 oxygen: 0.3	2	
oxidation	1000	oxygen: 2.25 hydrogen: 3.85	10:04	Target 100nm oxide thickness
cool down	-7 °C/min	oxygen: 2.25 hydrogen: 3.85	60	
boat out	600	nitrogen: 3.0	5	

After thermal oxidation, the thickness of the formed oxide on each wafer has been measured using Woollam Ellipsometer. The results are shown in table 5.2

Table 5.2: Oxide thickness per wafer measured using Woollam Ellipsometer

WAFER #	OXIDE THICKNESS (nm)
1	108.64
2	109.36
3	109.51
4	109.1
5	109.46

5.2. Substrate Contacts

Using the EVG120, the wafers are coated using Shipley SPR3012 positive photoresist with a thickness of 1.4 μm. Then mask 1 is used for the exposure with the MA8 contact aligner, with a dose of $140 mJ/cm^2$. After development, the substrate contacts are etched using the Drytek Triode 384T. Figure 5.2 shows one contact hole through the oxide to the substrate.

5.3. Metallization

Using the EVG120, the wafers are coated using AZ NLOF2035 negative photoresist with a thickness of 3.5 μm. Then mask 2 is used for the exposure with the MA8 contact aligner, with a dose of 55 mJ/cm^2. Choosing the dose is essential for this step as lift-off will follow. An exposure dose that is too large will result in too little undercut of the photoresist, making the lift off process more difficult. A dose that is too little will increase the undercut of the photoresist, which can result in small features to come off during development. Figure 5.3 shows a case in which photoresist lines with a width of 2 μm are disrupted after an x-link bake job followed by an x-dense development job. Processing is continued for wafer 5 while it remained such results, as the larger features were not affected. For wafers 1-4, the lithography steps were redone, but with twice the amount of time for the x-link bake step. Due to the increased strengthening of the photoresist, most of the features with 2 μm lines of photoresist ended up correctly, as shown in figure 5.4a. After removal of native oxide using Triton X100 and 0.55% HF, a 10 nm adhesion layer of chromium followed by a 100 nm layer of gold has been deposited on all 5 wafers using a CHA Solution evaporator. Then lift-off has been performed on all wafers using NMP at 70 °C until all gold has been removed from the areas it should be lifted off. Figure 5.4b shows a result after the lift-off process. Dicing is done to the wafers 1 and 5 after lift off in order to test devices already while processing is continuing for wafers 2-4.

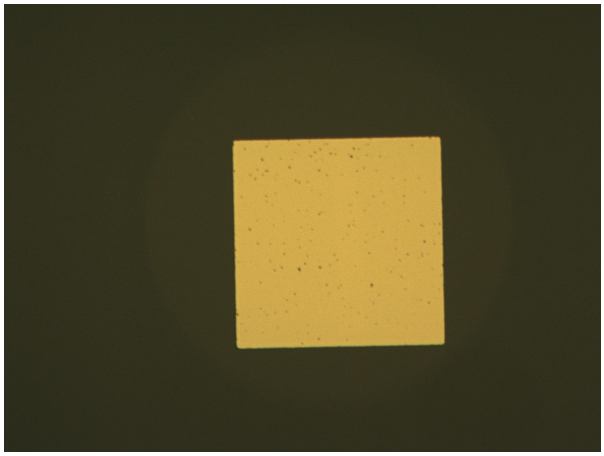

Figure 5.2: Substrate contact hole through the oxide layer.

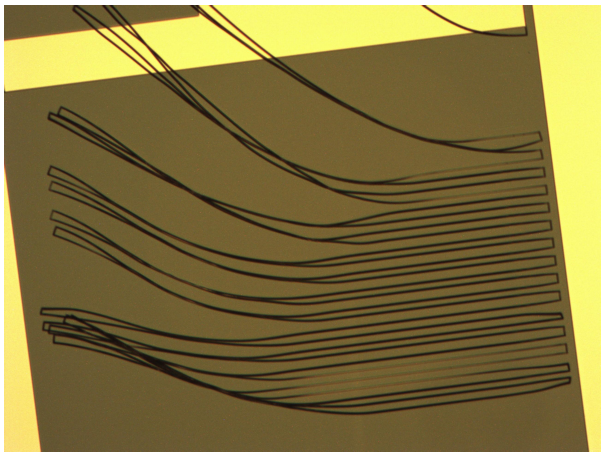

Figure 5.3: Faulty result of a negative photoresist pattern of an electrode pair with widths of $15\mu m$ and gaps of $2\mu m$.

5.4. Passivation Layer

Using CVD with the PlasmaLab 80, a layer of SiO_2 has been deposited on wafers 2-4, with a desired thickness of 300nm. The thickness is measured to be 321nm. The wafers are coated afterwards with Shipley SPR3012 positive photoresist with a thickness of $2.1\mu m$. The coated needs to be done manually as the previously deposited gold may otherwise contaminate the lab equipment. Using mask 3, exposure is then done with the MA8 contact aligner with a dose of $300 mJ/cm^2$. After post-exposure baking at 115 °C for 60 seconds and manual developing with Shipley MF322 for 60 seconds, the photoresist patterns shown in figure 5.5 are obtained. After the development, wet etching is done with BHF(1:7) to make openings in the oxide. Timing is essential for this step as overetching may also etch parts of the thermal oxide underneath, while with underetching the electrodes will stay buried under the oxide. According to etch rate data provided by the Else Kooi Lab in TU Delft, the etch rate of BHF(1:7) for the Novellus CVD SiO_2 is between 250-300nm/min, while for thermal SiO_2 it is between 60-90nm/min. This means that for a CVD oxide layer with a thickness of 321nm, the total etch time is between 64-77 seconds. Assuming worst case, etching for 77 seconds would etch at most 20nm of the thermal oxide layer underneath according to the given data. Because the narrowest electrodes are $2\mu m$ wide, an overetch of 20nm will not affect the functionality of the devices, and is therefore acceptable. Figure 5.6 shows microscope images of the CVD oxide etching process using BHF(1:7) for wafer 2 over time. According to the given etch rates, the maximum overetch should be 24nm after 80 seconds of etching. However, oxide thickness measurements with the FR-scanner reflectometer show that only around 15nm of thermal oxide is left at the etched areas. This large difference in etch rate is likely due to the fact that the CVD oxide in this work is obtained using a different equipment than what is used for obtaining the etch rates (Novellus Concept 1). For the rest of this thesis, measurements are continued on the dice on which no passivation layer is applied due to time limitations. Therefore no further wet etching is performed.

(a) Correct result of a negative photoresist pattern (yellow) over oxide (dark green) of an electrode pair for device W10G02, improved by increased time for x-link bake.

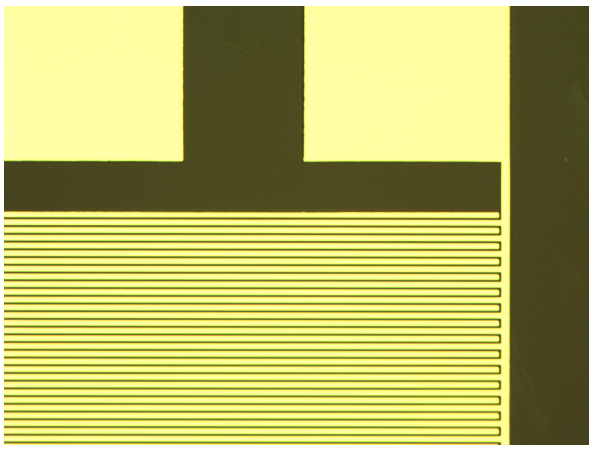

(b) Result after lift-off showing a gold electrode pair with widths of 15μm and gaps of 2μm.

Figure 5.4: Successful patterning results after a longer bake time is used.

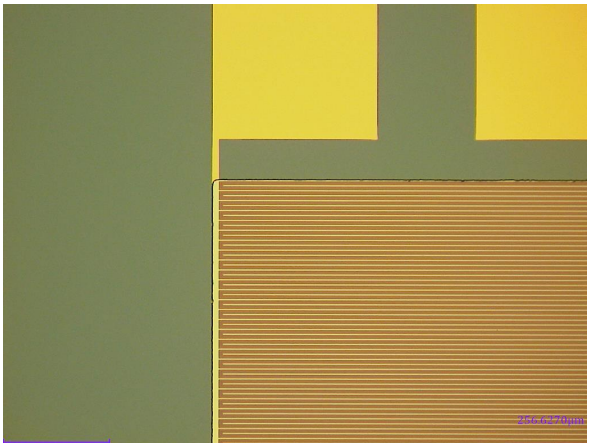

(a) Opening on device electrodes

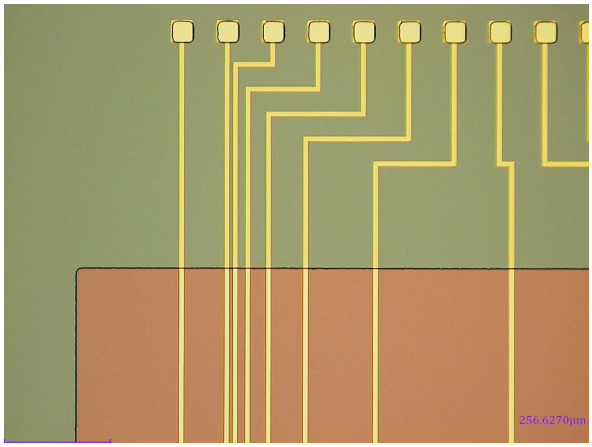

(b) Opening on a test structure

Figure 5.5: Openings (red areas) in the photoresist on wafer 2 after patterning with mask 3.

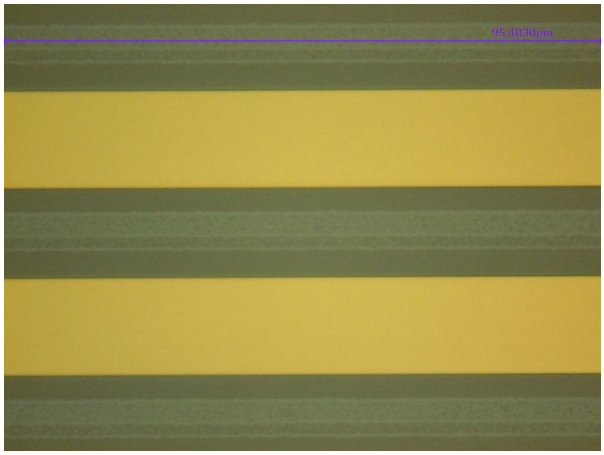

Figure 5.6: Wet echting result of CVD oxide using BHF(1:7) after 80 seconds of wet etching (wafer 2). At this point all of the passivation oxide is etched and the different shades of green are assumed to be caused by thickness differences of the thermal oxide.

6

Nanoparticle Characterization & Optimization

Before testing the gas sensing performance of metal oxide nanoparticles on devices, their characteristics are studied in this chapter. The deposition parameters are optimized such that nanoparticle layers with higher uniformity, conductivity and without cracks can be obtained. The methods covered in chapter 3 are applied in this chapter, starting with visual inspection of nanoparticles followed by more thorough inspection of their microstructure, material composition and electrical properties. To get a basic level of understanding regarding the properties of metal oxide nanoparticles, most of the inspection and characterization is done on tin oxide nanoparticles, followed by zinc oxide and copper oxide inspection in a lesser degree. It is worth mentioning that during deposition of tin and zinc layers on the test dice, stability issues with the spark are experienced and reported. Therefore, the thickness and uniformity of the deposited test layers may differ slightly from the usual case with similar printing settings.

6.1. Visual Inspection

As explained in chapter 3, parameters that can have an effect on the generated nanoparticle layers are spark voltage, spark current, nozzle size, nozzle height, movement speed over the printed area, and number of printing cycles. Since it is unknown what the effect of each parameter is on the sensing performance of the layers, a search is done for the most ideal printing settings by means of trial-and-error in this section. As a start, tin (oxide) is deposited over an area of 1x1 mm repeatedly as shown in figure 6.1a. Each square is deposited using different printing settings which are shown in table 6.1. The two deposited dots are there for nozzle alignment purposes. For this initial test the nozzle size is chosen such that it allows a gas flow of 0.32 L/min, as a larger nozzle could reduce the uniformity when printing over small areas and a smaller nozzle could reduce the coverage. Only the spark current and the distance between deposited lines are varied between depositions while other parameters are kept constant. The spark voltage is kept at 1 kV, the nozzle movement speed at 1 mm/min, and all lines are printed in 1 cycle at 1 mm nozzle height. It seems that the settings used for the first 4 depositions have a better coverage than the last 4 depositions. Since the difference here is in the distance between printed lines, this test confirms that a distance of 0.2 mm provides a higher coverage compared to a distance of 0.4 mm. The two alignment dots show a denser center with a diameter of around 0.1 mm, suggesting that spacings of 0.1 mm could provide higher coverage and uniformity. Therefore the choice has been made to set the spacings to 0.1 mm for future tin depositions.

While the deposition test with tin provides a (basic) level of coverage information, it does not provide any information regarding differences in uniformity. Zinc depositions seem to have a much higher level of transparency and therefore seem to be much more suitable for uniformity tests. Zinc nanoparticles are deposited as lines on another die as shown in figure 6.1b. For this test, only the nozzle movement speed and the number of printing cycles have been changed as shown in the printing settings provided in table 6.2.The spark voltage is set to 1 kV and the current is set to 3 mA. Differences in uniformity are clearly visible between the zinc depositions. For the first 5 lines, the deposition time is similar and the total deposited amount of particles is theoretically similar. However, the uniformity seems to improve as the nozzle movement speed and

the number of cycles is increased. It is expected that tin depositions would experience similar improvements with these settings regarding uniformity, despite not being visually observable. Therefore, a printing speed of 40 mm/min and printing cycles of 40 are chosen for now as settings to be applied for future tin and zinc depositions. In the following sections it will become clear whether the chosen settings provide nanoparticles with characteristics in terms of microstructure and conductance suitable for gas sensing.

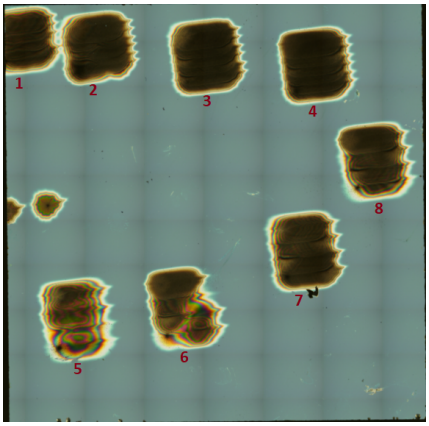

(a) Tin squares.

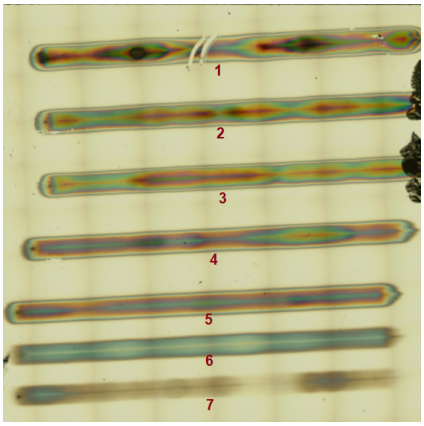

(b) Zinc lines.

Figure 6.1: Patterns of tin and zinc deposited for printing optimization.

Table 6.1: Printing conditions for each tin oxide pattern printed on dies shown in figure 6.1a.

Deposit Number	Current (mA)	Line Distance (mm)
1	8	0.2
2	10	0.2
3	5	0.2
4	3	0.2
5	8	0.4
6	10	0.4
7	5	0.4
8	3	0.4

Table 6.2: Printing conditions for each zinc oxide pattern printed on the die shown in figure 6.1b.

Deposit Number	Movement Speed (mm/min)	Cycles
1	5	5
2	10	10
3	15	15
4	20	20
5	40	40
6	40	20
7	10	3

6.2. Microstructure

Further inspection is done in this section using the scanning electron microscope (SEM) to check if the previously chosen printing settings provide sufficient coverage and particle connectivity on the micro/nano scale. As an additional material, a copper sample has also been deposited. Because of low deposition rate being noticed for copper, the spark current during copper deposition has been increased to 8 mA, while all other settings are kept similar (1 kV, 40 cycles, 40 mm/min movement speed). Figure 6.2 shows SEM images of tin, zinc and copper nanoparticles. There are no cracks visible in any of the layers, which suggests that the layer thickness for each test pattern is less than the maximum attainable layer thickness without cracks. All three depositions seem to have a relatively high coverage. For the zinc sample in figure 6.2b, the connections between the particles seem narrow, while for the other two materials the particles seem more clustered. For this reason, it is expected that the zinc layer has a lower conductivity as it depends on the amount of these shown connections.

During SEM inspection of tin nanoparticle layers without annealing, it is observed that the electron beam causes melting. This is shown in figure 6.3, where clearly melting has occurred at a previously zoomed in

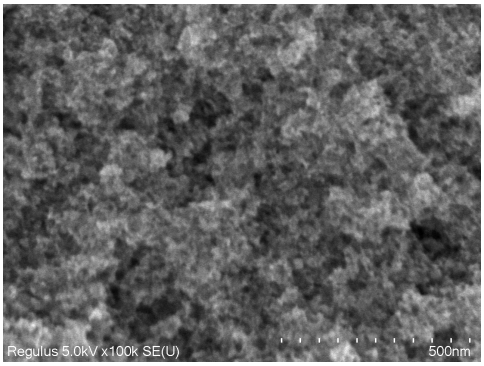

(a)

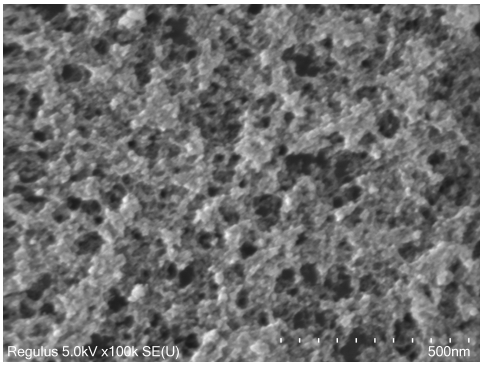

(b)

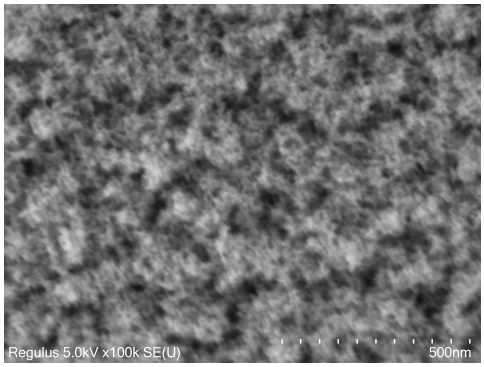

(c) Copper

Figure 6.2: SEM images of non-annealed tin, zinc and copper nanoparticles at x100k magnification.

area. This is not seen during SEM inspection of zinc. Sn and Zn have much lower melting points compared to SnO_2 and ZnO. Therefore, the observed melting could suggest that tin nanoparticle layers do not oxidize sufficiently when exposed to air at room temperature, while zinc does. After annealing the samples at 500 $°C$ for 2 hours, SEM inspection is performed again on the samples. No notable difference is observed before and after annealing at x100k magnification. However, the melting phenomenon is not present anymore, meaning that it is very likely that annealing has contributed to the oxidation process of tin. This effect is studied more thoroughly in the next two sections using EDX and XRD.

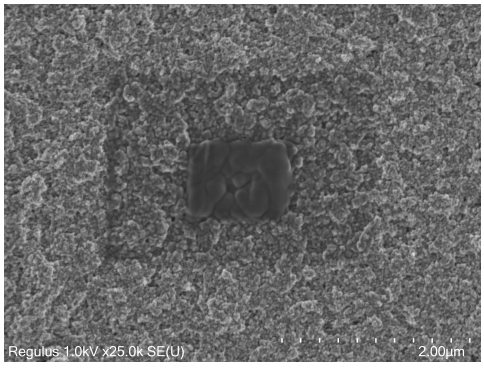

Figure 6.3: Melting of non-annealed tin due to the electron beam during SEM inspection.

6.3. Material Composition of Tin (Oxide)

As described in chapter 3, two methods used for inspection of material composition are EDX and XRD. Both provide different types of information and have their limitations. While EDX could make it clear whether any oxidation takes place during annealing, it would not provide information regarding the phase after oxidation. XRD does provide data regarding phase, but is only able detect crystalline materials. However, combined

usage of these two methods is expected to provide an indication whether oxidation took place and which phases the samples contain.

6.3.1. EDX

Table 6.3 shows EDX results for a tin oxide sample before annealing. The results show an almost one-on-one atomic ratio for Sn and O. This could mean that perhaps the sample has not fully oxidized at that point, or that it has only oxidized to SnO, meaning a metastable initial oxidation stage has been reached that occurs before SnO2 is formed [13]. EDX inspection is also applied to a tin sample after an annealing process at 500 °C for 2 hours, of which the results are shown in table 6.4. The annealing step does not seem to have influenced the atomic ratio between Sn and O. However, the melting phenomenon shown in 6.3 not occurring after annealing does suggest that oxidation has occurred due to annealing. It could therefore be the case that either SnO2, Sn3O4 or SnO is being formed during annealing, or that a core-shell structure is formed of which the core consists of Sn or Sn2O3 and the shell consists of Sn2O3, SnO2 or SnO [67]. Because the EDX results do not provide any relevant information here other than the Sn:O ratio, XRD inspection is done in the next section in order to obtain the phases that are present before and after annealing.

Table 6.3: EDX results of an Sn/SnO2 sample before annealing.

Element	Weight %	Atomic %
C K	16.88	53.31
O K	9.81	23.27
SnL	73.31	23.43

Table 6.4: EDX results of an tin/tin oxide sample after annealing at 500 °C for 2 hours.

Element	Weight %	Atomic %
O K	11.37	48.77
SnL	88.63	51.23

6.3.2. XRD

An XRD pattern of a non-annealed tin sample is shown in figure 6.4. It shows that pure Sn nanoparticles are present that are stable in air. No phases of tin oxide are detected at all. This could be either due to no oxidation having occurred at all, the oxide layer being too thin to be detected, or all oxide being amorphous. The broad bumps at the peaks may suggest that amorphous phases are present. An annealing step, however, is expected to increase the crystallinity and thus provide more accurate XRD data as explained in chapter 2.

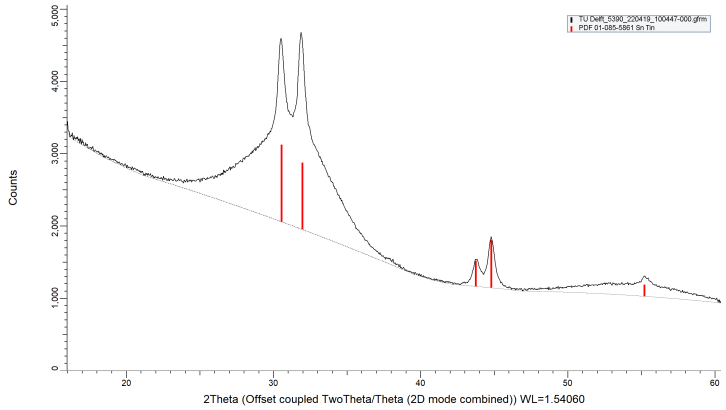

Figure 6.4: XRD results of a tin/tin oxide sample before annealing.

To see if annealing has an effect on oxidation and crystallinity, XRD has also been performed on an annealed tin sample. The result of this is shown in figure 6.5 and it clearly shows higher, somewhat narrower peaks at phases that are typical for SnO_2. Smaller peaks of SnO are shown, but no pure Sn is found. The broad peaks may indicate small crystallites. Annealing at a higher temperature or for a longer time could perhaps eliminate the present SnO in order to increase the purity of SnO_2 nanoparticles. A second annealing step of 2 hours at 500 °C is applied on the sample to test this. A similar XRD result is obtained after the second annealing process as the one shown in figure 6.5, where the SnO phase is still present and the crystallinity is not improved further. It is concluded from this that a single annealing process at 500 °C for 2 hours is

sufficient for having stable SnO_2 nanoparticles and that no further oxidation will take place during operation at temperatures lower than 500 °C.

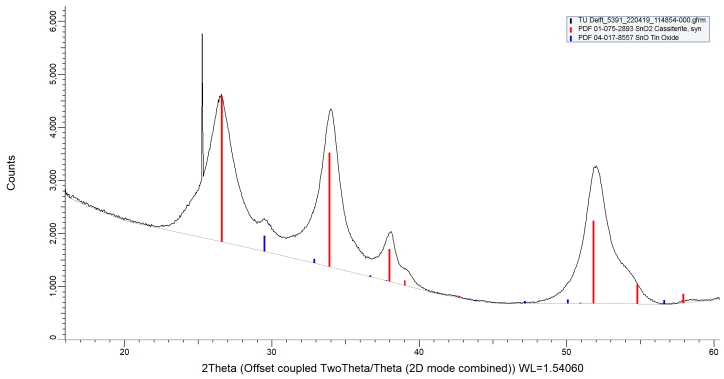

Figure 6.5: XRD results of a tin/tin oxide sample after annealing at 500 °C for 2 hours.

6.4. Conductance Measurement

Now that it is known that with the chosen printing settings and annealing process, nanoparticles can be obtained that have no cracks, high coverage, and stability at high temperatures until 500 °C (at least for SnO_2), conductance measurements are performed in this chapter to test if further adjustments to the settings are required. Nanoparticles are first deposited on a test sample that is suitable for four-point measurements to eliminate contact resistance. Then they are deposited on a couple of chemiresistors that were designed in chapter 4. From this it will become clear whether the current approach of generation nanoparticles is applicable on actual devices.

Figure 6.6a shows the test sample with deposited zinc oxide (lines 1-5) and tin oxide (lines 6 and 7) nanoparticle lines. The printing conditions are provided in table 6.5. This time the layer thicknesses, measured using the Dektak 150, are also provided. There is a clear difference in thickness between zinc oxide and tin oxide layer for similar printing settings. Layer 2 was even too thin to be able to be measured by the equipment. At the same time, tin is deposited on five chemiresistors, of which three are shown in figure 6.6b. The printing settings are similar for all of the five devices (1kV, 3mA, 40mm/s, 40 cycles, 0.1mm spacings). However, there are clear differences in uniformity between devices that can be attributed to stability issues of the generator that were mentioned in the beginning of the chapter. Absolute numbers of conductance obtained from these measurements are therefore not useful. However, the devices are useful for examining the effect of gate biasing and temperature differences on them.

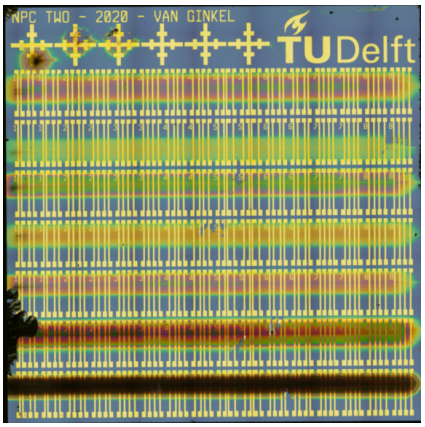

(a) Test die with zinc oxide (top 5 lines) and tin oxide (bottom 2 lines). Printing settings in table 6.5.

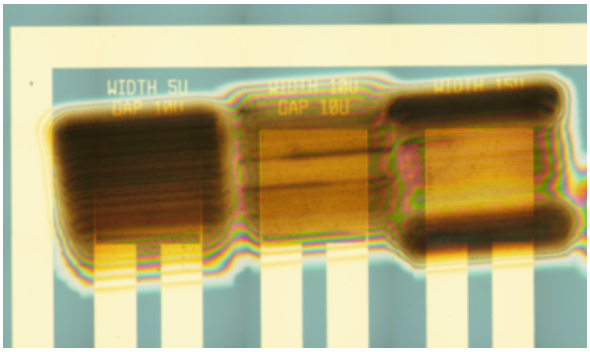

(b) Three of the five devices that is printed on (W05G10, W10G10, W15G10).

Figure 6.6: Samples used for conductance tests.

Table 6.5: Printing settings for the zinc and tin nanoparticle layers on the test die in figure 6.6a

Deposit Number	Electrode Material	Voltage (kV)	Current (mA)	Movement Speed (mm/min)	Cycles	Thickness (nm)
1	Zinc	1	3	40	40	180
2	Zinc	1	3	40	20	N/A
3	Zinc	1	3	40	60	220
4	Zinc	1	3	60	40	140
5	Zinc	1	3	60	60	300
6	Tin	1.3	3	40	20	580
7	Tin	1.3	3	40	40	1350

6.4.1. Effect of Annealing

For the Zn depositions (lines 1 to 5), conductance measurements do not provide I-V curves at all, presumably because there is barely conductance. This could be because of a lack of available current paths through the layers. It was mentioned previously in section 6.2 that the microstructure of ZnO nanoparticles is likely to affect the conductivity negatively. For the Sn depositions however, clear results are obtained regarding their conductivity. Figure 6.7 shows the I-V curves of the tin depositions on the test die in figure 6.6a before and after annealing once. It can be seen that annealing improves the conductance of the Sn layers significantly. Despite the fact that pure tin has a higher conductivity than tin oxide, the additional connectivity between particles caused by annealing appears to be dominating. It is worth noting that for line 6, the measurements after annealing suffer from nonlinearity. This indicates that the printing settings used for line 6 might not be suitable for stable conductance, while those used for line 7 are.

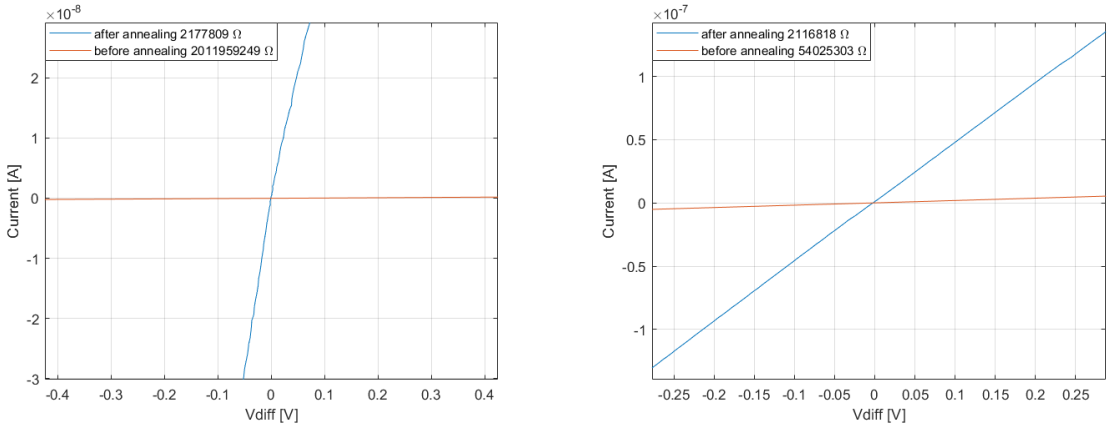

(a) Line 6.

(b) Line 7.

Figure 6.7: Measured conductance data of lines 6 and 7 (Sn) on the test die in figure 6.6a, before and after annealing at 500 °C for 2 hours.

6.4.2. Effect of Operating Temperature

Since metal oxide gas sensors are operated at higher temperatures (~200 °C), conductivity measurements are performed at different temperatures between 25 °C and 200 °C on the tin samples on the test die and on the devices. It is expected that the elevated temperatures do not cause physical changes in the layers as annealing is done previously at 500 °C. Figure 6.8a shows I-V curves of line 7 of the test die at different temperatures, and it clearly shows that the conductance is largely dependent on the operating temperature. Temperature coefficient of resistance (TCR) calculations are performed as shown in figure 6.9. The TCR is found to be in the range between -0.028 /°C and -0.0057 /°C for temperatures between 25 °C and 200 °C.

Similar measurements at different temperatures are performed on one of the chemiresistors without gate biasing to test if there is any difference in temperature dependence between a single line and a chemiresistor. Figure 6.8b shows the operation of a device at different temperatures. It shows that the resistance of the

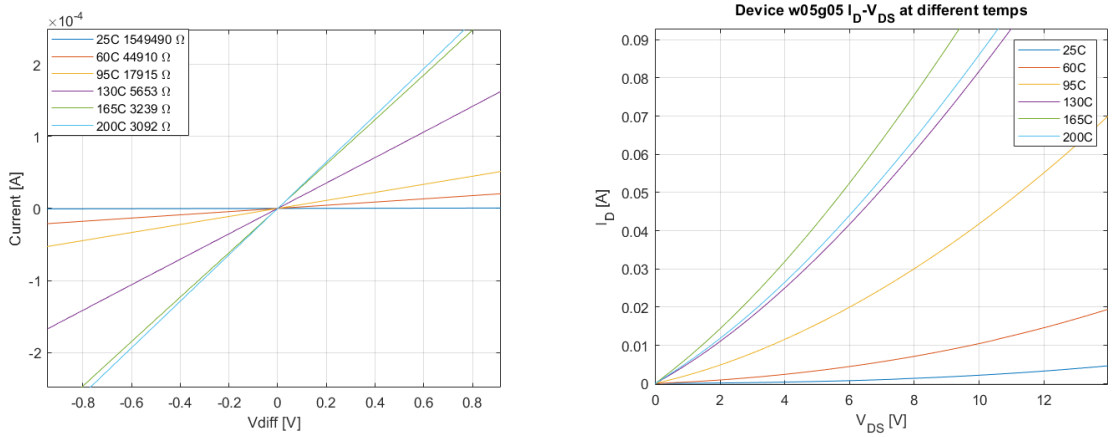

(a) 7th deposited (SnO_2) line from figure 6.6a.

(b) Device W05G05 with SnO_2.

Figure 6.8: Conductance data of SnO_2 at temperatures between 25 °C and 200 °C, showing that the conductance of the nanoparticles highly depends on the operating temperature.

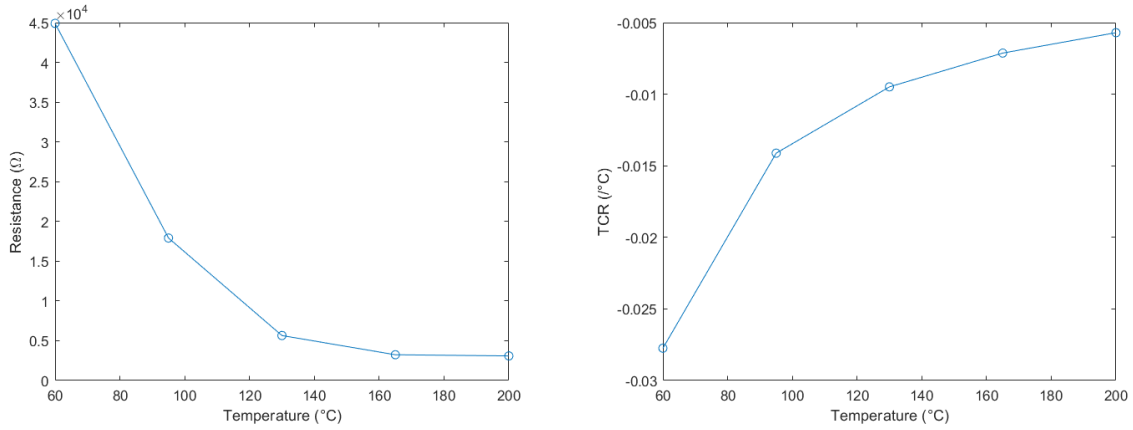

(a)

(b)

Figure 6.9: Resistance versus temperature (a) and temperature coefficient of resistance (TCR) versus temperature (b) of the 7th line (Sn) on the test die shown in figure 6.6a.

device drops to values close to 100 Ω at higher temperatures. Such low resistances being achieved can be attributed to the large contact area of the interdigitated electrodes. Despite the large difference in resistance between the single line and the chemiresistor, the TCR for the chemiresistor seems to be very similar to what is calculated for the line in figure 6.9b. It is concluded from this fact that nanoparticle coverage and electrode geometry have no influence on the temperature dependency of metal oxides. However, it will be important during gas sensing measurements to keep the operating temperature constant, as it seems here that even small variations of temperature can affect the resistance and therefore the gas sensing behavior.

6.4.3. Gate Biasing

Since very low values for resistance (~100 Ω) on a particular device (W05G05) with SnO_2 are measured in the previous section, the question remains whether gate biasing will reduce it further. It was explained in chapter 2 that a higher gas response could be achieved if that is the case. A bias is applied to the gate of device W05G10 at three different temperatures in figure 6.10. For each I-V curve the bias is first incremented from 0V to 50V and then decremented from 50V to 0V with steps of 5V. This gives multiple results per value and helps to see if the conductance is affected by the measurement itself. If the difference between two curves with the same biasing voltage is large, self-heating is likely involved. Only the results of biasing with 0V and 50V are plotted for simplicity.

In figure 6.10a, it can be seen that applying a gate bias on the device operating at room temperature gives

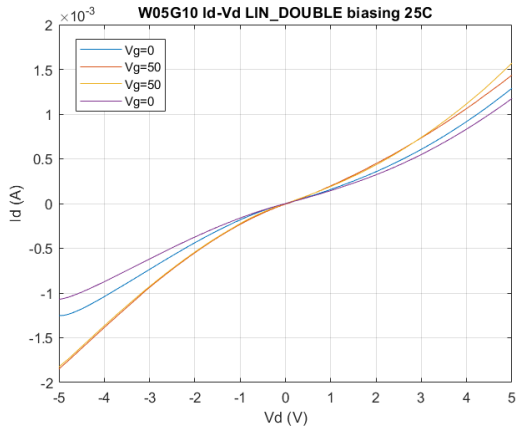

(a) 25 °C

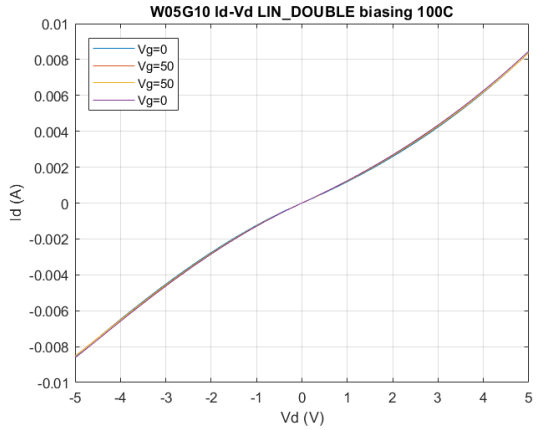

(b) 100 °C

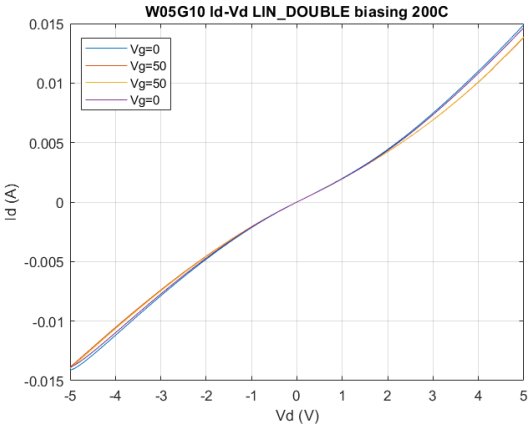

(c) 200 °C

Figure 6.10: Biasing of the gate of device W05G10 at different temperatures. The biasing voltage is incremented with steps of 5V between 0V-50V and decremented again from 50V to 0V. Only results of 0V and 50V biasing are given for simplicity.

a slightly higher conductance. The asymmetry of the curves at positive and negative drain voltages and the difference in curves with the same biasing voltages do suggest that self-heating is involved. Figures 6.10b and 6.10c show that biasing has less influence at higher temperatures for this device. This shows that perhaps gate biasing does not improve the performance of sensing devices with SnO_2 as sensing material. To test if biasing could have a bigger influence on p-type semiconductors, CuO nanoparticles have been printed on two devices. It is found that the deposition rate of copper nanoparticles is around six times lower relative to the deposition rate of tin nanoparticles. Therefore, copper has been deposited in 240 cycles and with a spark current of 5 mA, while all other settings are kept similar to those which are used for tin. The results are shown in figure 6.11, where the two CuO devices are operated at room temperature. Biasing seems to barely cause any difference in conductance for the two CuO devices, even at room temperature. Since it is only proven so far during these tests that biasing causes a measurable difference for an SnO_2 device at room temperature, it is not applied during the gas sensing measurements in chapter 7.

6.4.4. Self-heating Damage

Significant damage has been observed on two SnO_2 devices after conductance tests. Figure 6.12a shows the device with the most severe damage. It is likely the case that the damaged pattern follows a current path through the semiconductor layer. The damage occurred after the application of drain-source voltages of up to 20 V. Considering that resistances were reached with these devices as low as around 100 Ω, the applied power is 4 W, highly likely to cause damage due to local heating. Figure 6.12b shows an SEM image of what is assumed to be melted SnO_2 in the destroyed area. SEM inspection of other areas on the device suggests that those areas are not damaged at all. This could mean that there are no current paths there, or that not enough time has passed for damage to occur at those areas. After the damage has occurred, remaining measurements

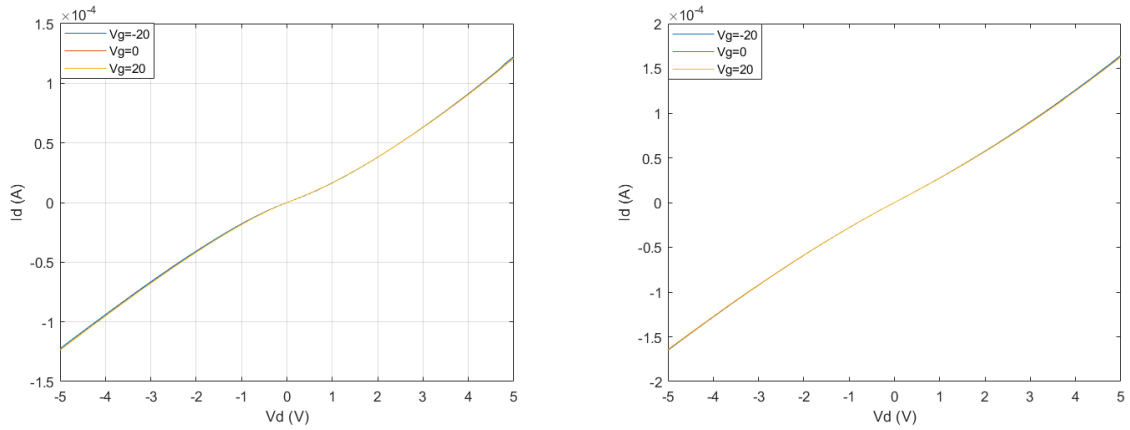

(a) W02G05

(b) W10G02

Figure 6.11: Two devices with CuO at room temperature with gate bias applied between -20 V and 20 V.

have been performed with drain-source voltages not higher than 5 V.

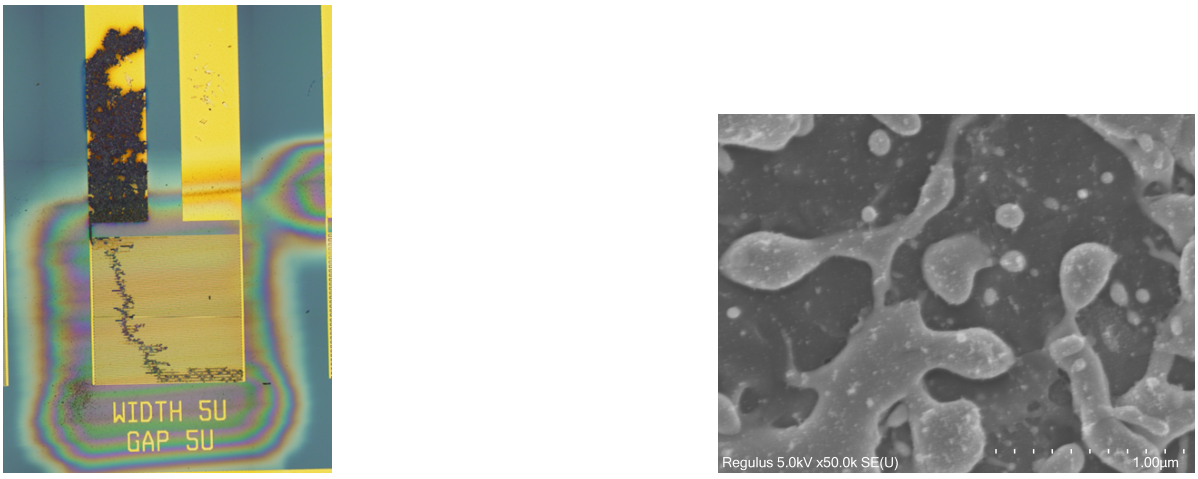

(a) Optical view

(b) Higher magnification SEM image of damaged area

Figure 6.12: Damaged device due to heat caused by applied power.

6.5. Conclusion

Starting with a trial-and-error approach, printing settings have been chosen for generating nanoparticles with high coverage, uniformity and without the presence of cracks through the layers. SnO_2 is deposited with a variety of settings for coverage comparisons, followed by ZnO depositions that allow for basic uniformity checks due to their transparency. The chosen settings for tin and zinc are as follows: 1 kV spark voltage, 3 mA spark current, 40 cycles, 40 mm/min printing speed, 1 mm nozzle height, and 0.32 l/min nozzle through flow. It is observed that the deposition rate of copper is relatively low, and therefore the spark current is increased to 5 mA and depositions are performed in 120 cycles, while other settings are kept similar. Melting of tin being observed during microstructure inspection due to the electron beam of the SEM suggested that tin nanoparticles do not oxidize at room temperature in air, since there is a large difference between the melting points of Sn and SnO_2. Measurements on the material composition using EDX and XRD confirmed that this was indeed the case, and that annealing stimulates the oxidation. The conductance of nanoparticles seems to be temperature dependent and has a TCR between -0.028 /°C and -0.0057 /°C, but this dependence is not influenced by coverage area or device geometry. Gate biasing only resulted in a notable difference for SnO_2 at room temperature, and did not cause any increase in conductance at temperatures at which metal oxide gas sensors are usually operated at. Working with ZnO devices is discontinued as no conductance is detected

during measurements.

7

Results & Discussion

This chapter presents and discusses experimental results obtained during gas sensing tests. Due to limited time and availability of the setup and the lab, only one metal oxide semiconductor is chosen for these tests, which is SnO_2 as it is the most extensively characterized material in chapter 6 and is therefore the material with the most information regarding microstructure, material composition, and conductance data at different temperatures. In this chapter, the response of an (n-type) SnO_2 device is defined as $\frac{Ra-Rg}{Rg} \cdot 100\%$ for reducing gases and $\frac{Rg-Ra}{Ra} \cdot 100\%$ for oxidizing gases, where Ra is the resistance measured without the target gas (usually in air, but nitrogen in this study) and Rg is the resistance measured during exposure to the target gas.

It should be noted that for some of the measurements in this chapter, the operating temperature is 250°C, while for other measurements it is 200°C. The reason for this is that initially the choice is made to operate the devices at 250°C to stimulate device recovery, but eventually damage is found in the test setup that may be caused by heat. Therefore the chosen operating temperature is reduced to 200°C.

The gas sensing setup described in section 3.4 that consists of three gas vapor generators (target gas, humidity and pure nitrogen), a sensing chamber with a hotplate and 50 probe needles, a sourcemeter and a multiplexer, is used to obtain the results in this chapter. Setting bias values and switching between devices is controlled using a modified version of a LabVIEW script provided by Hanxing Meng [68]. The setup and the fabricated samples allow for simultaneous two-point measurements of up to 24 devices. However, due to needles of the setup not aligning properly with the contact pads of the samples, the initial tests are only done on single devices. The alignment is fixed during maintenance right before ethanol tests, after which tests are done on multiple devices simultaneously with all devices operating under similar conditions. The switching frequency of the multiplexer is 2 Hz, and therefore the density of data points per device depends on the number of channels used. Gate biasing is not applied for the tests in this chapter as it was clear from chapter 6 that it barely has an influence on the conductivity at elevated temperatures.

7.1. Humidity Test

As mentioned in chapter 2, n-type metal oxide semiconductors, which includes SnO_2, tend to be sensitive towards humidity. This is undesirable for practical gas sensing as variations in humidity can disturb the selectivity towards a desired target gas. However, if the response towards humidity is significant, it can provide an indication of the response and recovery time of a device in general. Humidity is provided by the OHG-4 humidity generator that was described in chapter 3, and is carried by nitrogen. For the recovery of devices, the humidity generator is disconnected and the OFC-1 flow controller is connected to provide pure nitrogen gas onto the devices as a drying method. In this section, the sensitivity of devices with SnO_2 towards various concentrations of relative humidity is tested.

Figure 7.1 shows the responses of an SnO_2 device to three cycles of 35% relative humidity. The figure clearly shows that humidity causes a significant drop in resistance when it reacts with SnO_2. This means that water acts as a reducing agent in this particular reaction (since SnO_2 is an n-type semiconductor). Despite sensi-

tivity towards humidity is generally undesirable for gas sensors, this result confirms that the devices are able to sense. The three cycles in the figure have a response of 1300%, 1150% and 1000% from left to right respectively. These numbers are significantly higher than the responses of any of the sensors from literature with SnO_2 towards various target gases in table 2.1. It is therefore very likely that the sensitivity towards humidity of this sensor will affect its selectivity towards target gases, if the response is smaller towards those gases.

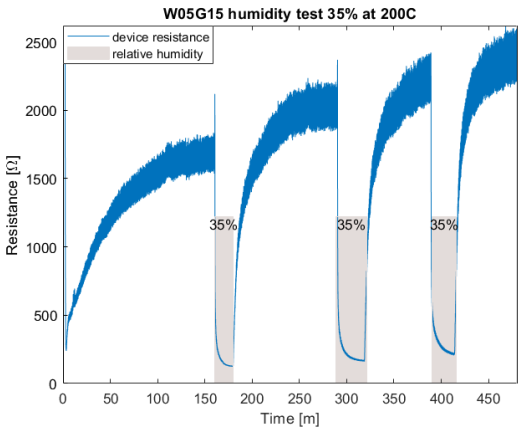

Figure 7.1: Humidity testing on a 1x1mm SnO_2 gas sensor with electrode widths of 5μm and gaps of 5μm at 200°C. Pulses of 35% relative humidity are applied in order to test repeatability. The cycles show a response of 1300%, 1150% and 1000% from left to right respectively.

There does seem to be a shift present in the baseline of the resistance in figure 7.1. After every recovery phase, the value at which the resistance settles is larger than before, and the resistance during exposure also seems shift to some extent. It is unlikely that further oxidation of the tin into tin oxide is causing this shift, as the XRD results in chapter 6 show that further annealing of SnO_2 has no effect on its composition. A possible explanation for this behavior is that a change occurs to the path of the current flowing through the semiconductor layer. The visible damage to a device shown previously in figure 6.12 in chapter 6 shows what seems to be a burnt current path. A change in the resistance of the layer is expected as soon as such a path ceases to be available, and the current flows through an alternative path. According to literature, drift in metal oxides can be the result of either reorganization of the sensor surface due to aging, or irreversible binding of measured gases or contamination [69].

Another phenomenon that can be observed from the resistance curve in figure 7.1 is the time it takes for the device to recover and stabilize, which is significantly longer than what is practical for real-world gas sensing. Initially after reaching the operating temperature of 200°C while flushing with nitrogen, it takes around 160 minutes for the resistance to stabilize. After the first exposure to humidity, it takes around 80 minutes to stabilize. Not enough time is given for full recovery after the second and third sensing phase due to the closing time of the laboratory. The long recovery time is associated with the surface reactions being slow [70], and is the reason for elevating the operating temperature as specified in chapter 2.

Now that the effect of a certain concentration of humidity on the resistance of SnO_2 nanoparticles is known, a second humidity test is performed. Different percentages between 30% and 97% of relative humidity are tested in this case and the results are shown in figure 7.2. Four concentrations for the humidity are predetermined and it is increased and decreased in steps. Because the humidity concentration is set using two manual knobs for wet and dry flow instead of a digital interface like for the target gas concentration (shown in figure 3.6), the transition between humidity levels does not happen abruptly and it can take a longer time to reach the desired level. This test is therefore not suitable for finding the response time of the sensor for humidity level transitions, but it is useful for finding the values the resistance settles at for certain humidity levels.

At around minute 50 with the relative humidity set to 50%, the resistance seems to either experience a drift similar to the previous humidity test, or the actual humidity in the chamber has not settled yet. After the first transition, the resistance seems to be stabilize at each humidity level until around 160 minutes in with

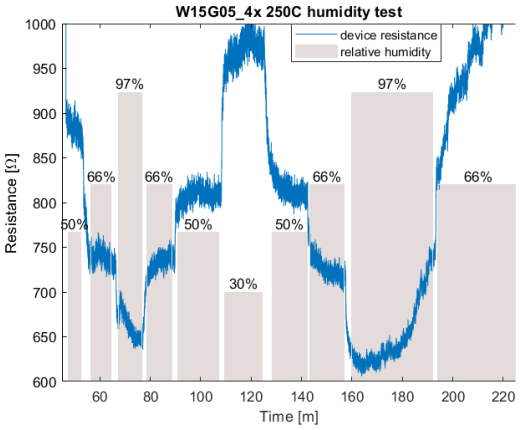

Figure 7.2: Humidity testing on a 4x1mm gas sensor with electrode widths of 15 μm and gaps of 5 μm at 250 °C.

the exception of when the relative humidity is set to 97%. However, it is realized after this measurement is done that the humidity generator can only accurately (±1%) generate a relative humidity between 1% and 90% according to its datasheet [63]. The instability of the resistance at minute 70 is therefore likely caused by variations in humidity during that period. Until 160 minutes in, the resistance settles at similar values for similar humidity levels at different times, suggesting that the sensor has repeatability within the time interval between minutes 55-160. After that time interval, the resistance experiences a sudden drift that may be caused by the same reason that caused the drift during the previous humidity measurement in figure 7.1.

7.2. NO2 Sensing

NO_2 is an oxidizing agent, which means that the exposure of SnO_2 to NO_2 gas is expected to increase its resistance as explained in chapter 2. A first attempt to sense NO_2 gas using a sensor with SnO_2 is shown in figure 7.3. Surprisingly, the resistance of the device reduces as soon as NO_2 is admitted. However, it becomes clear that it is not the exposure to NO_2 that is causing the drop in resistance as the drop also occurs at 160 minutes in when there is 0 ppm of NO_2 being admitted. In this particular experiment, the flow during admittance of NO_2 carried by nitrogen is set to 100 mL/min, while during the recovery phase the flow of pure nitrogen gas is set to 1000 mL/min. As around minute 160 there is no NO_2 and the only difference between the sensing phase and the previous recovery phase is the flowrate, it is clear that this is causing the response. As seen in the previous section, SnO_2 nanoparticles have a high sensitivity towards humidity. It can be concluded from this experiment that the flowrate used for providing the target is insufficient to eliminate humidity and therefore an increase in humidity is experienced after flushing during recovery.

Despite no meaningful data regarding NO_2 sensing being provided by this experiment, it has made it clear that the approach is prone to be affected by changes in humidity. Therefore the methodology for sensing target gases has been adapted for the rest of the measurements as follows: using the three vapor generators, the total flow entering the chamber is set to be equal throughout entire measurements. The humidity generator is set to 2000 mL/min for both sensing and recovery phases in order to maintain an equal concentration of humidity during both phases. The flow of the pure nitrogen source is set to 1000 mL/min during recovery to promote dilution more. When sensing a target gas, the flow of the nitrogen is reduced by the same rate that the target gas source flow is increased. This way the total flowrate is stays at 3000 mL/min, the humidity is constant, and the only change between sensing and recovery is the concentration of the target gas.

The improved methodology has been applied during the NO_2 experiment shown in figure 7.4. The relative humidity is maintained at 45% in order to prevent abrupt changes in humidity during measurements as was seen before, and to promote the freeing of oxygen vacancies for NO_2 to react, as humidity acts as a reducing gas here. There is an increase and a decrease in resistance during every sensing and recovery phase respectively, just as expected. This means that the new approach has been successful in detecting target gases. During the third admittance of NO_2 between minutes 25-40, it seems that sensing happens in two phases, where there is a steeper increase during the first phase (~27 minutes) and a milder increase during the second

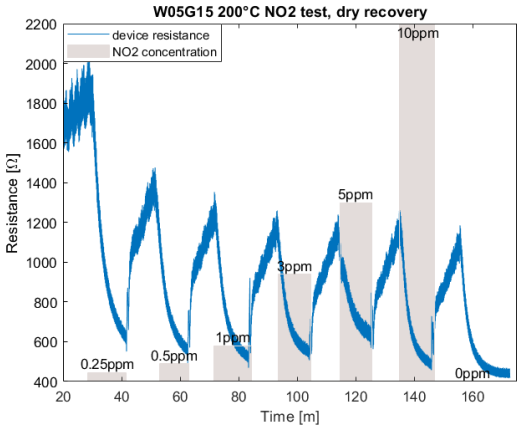

Figure 7.3: First attempt to sense NO_2 where actually change in humidity is being sensed instead. Despite the fact that no meaningful result regarding NO_2 is obtained here, this experiment plays an essential role in this project leading to an improved methodology for the gas sensing experiments hereafter.

phase (minutes 28-40). This suggests that most of the reactions take place on the surface of the semiconductor initially, after which most reactions take place deeper underneath the surface as the gas diffuses through the porous surface. It can be seen that the milder increase has not settled, and it is unclear how long it would take for that to happen. Due to the limited availability of the laboratory, the sensing phase is not continued for that to be observed. The settling point after recovery for the resistance also seems to shift over time, similar to what was observed during the humidity tests in section 7.1. The reason for this shift is expected to be similar to what caused it during the humidity tests, presumably because of changes in the current paths through the nanoparticle layer during operation. Due to these shifts and the fact that the resistance has not settled during the sensing phases, it is not straightforward to obtain a value for the gas response form this experiment. However, it can be concluded that the steeper increase at around minute 27 presumably due to surface reactions has a response of 5%. Because the response is relatively small, the settling time during sensing is relatively long, and the laboratory access is limited, NO_2 tests are discontinued here, and more extensive experiments are performed in the rest of the chapter with ethanol instead.

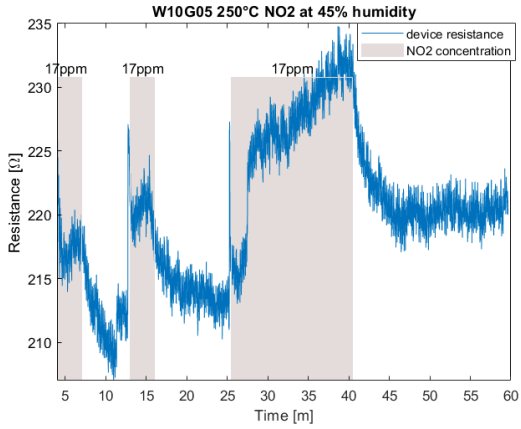

Figure 7.4: NO_2 testing on an SnO_2 device with the new measurement approach where the total flow and humidity level is maintained throughout the entire measurement. The expected increase and decrease in resistance is finally observed during the sensing and recovery phases.

7.3. Ethanol Sensing

Ethanol is a reducing gas and is therefore expected to make the resistance of SnO_2 decrease. As it was observed in 7.1, humidity also acts as a reducing gas when it reacts with SnO_2 nanoparticles. It is expected therefore that the presence of humidity is expected to reduce the response when performing ethanol tests, as

both gases behave similarly by removing oxygen atoms from the semiconductor. For this reason, the humidity level for ethanol is maintained at 35%, lower compared to what was used for NO_2 sensing. This way the focus of the measurements can be more on the response of ethanol with less noise caused by humidity reactions. As mentioned in the beginning of this chapter, alignment issues with the probe needles are experienced and the number of usable needles is limited. Therefore this section begins with ethanol experiments performed on single devices only, where information is obtained on the stability, response and recovery of SnO_2 devices. Simultaneous ethanol experiments on multiple devices have been performed after repair work has been done on the chamber, of which the results can be used to compare the sensing performance of devices with different electrode geometries.

7.3.1. Single Device Tests

Figure 7.5 shows the first test with ethanol gas on a device operating at 250 °C. A continuous downwards drift in the resistance is present throughout the experiment, most notably during the first 120 minutes of it. Presumably this is caused by more current paths becoming available or contaminants are present that increase the conductivity. Similar to the NO_2 test, gas exposure causes an abrupt change in resistance due to surface reactions, followed by a milder change caused by reactions deeper underneath the surface. The abrupt drop seems to be somewhat consistent for both exposure cycles (~25-30Ω). The decrease in resistance afterwards is faster for the first exposure compared to the second, but this is likely due to the fact that more drift is involved during the first exposure. The data between minutes 135-170 shows a full cycle where the resistance approaches stability during both the sensing phase and recovery phase. The response here is around 39%.

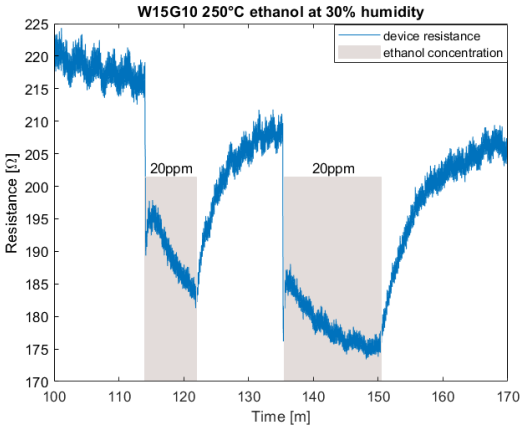

Figure 7.5: Ethanol gas sensing experiment with repeated admittance of 20 ppm ethanol. A drift in resistance is present as can be seen from the beginning until around minute 113, but also from the values that the resistance seems to settle during recovery after every exposure. Ethanol exposure causes an abrupt resistance change, followed by a milder decrease similar to the NO_2 experiment in figure 7.4. The response during the full cycle (minutes 135-170) is 39%.

Now that it is clear that ethanol can be sensed by devices with SnO_2 with a relatively large response, a second experiment is done in which different concentrations of ethanol are admitted as shown in figure 7.6. The operating temperature is reduced to 200 °C as damage due to heat is observed in the sensing chamber after the previous measurements. Interestingly, there is less drift in resistance during this experiment than the ones before, with a shift of only 1 Ω between minutes 36-142 (right before admittance of ethanol). This is likely due to a large amount of available current paths (hence the low resistance). Both concentrations cause a similar initial drop in resistance (~10 Ω), suggesting that both concentrations are sufficient for all oxygen atoms on the surface to react. 20 ppm of ethanol appears to react with atoms that are deeper underneath the surface, hence the further decrease in resistance at minute 40, with a total response of about 28%. Exposure of the device to 5 ppm of ethanol does not seem to cause reactions underneath the surface, as the resistance dwells around the value it ended up at after the sudden drop.

7.3.2. Damage After Usage

It has become clear from the experiments that the gas sensors suffer from resistance drifts during operation. In some cases the drift is as small as single ohms (figure 7.6), while in other cases it can render the device use-

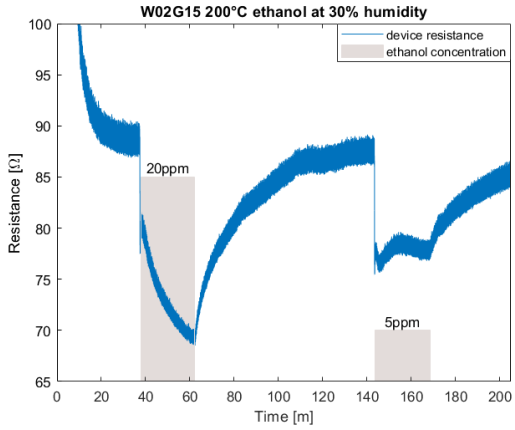

Figure 7.6: Ethanol testing with different concentrations on a 1x1mm gas sensor with electrode widths of $2\mu m$ and gaps of $15\mu m$ at 200 $°C$ and 30% relative humidity. The response for 20 ppm ethanol is 28%.

less (figure 7.2). The presence of these drifts makes the baseline of the resistance unpredictable and therefore affect the reliability of the sensors. Furthermore, if it is the case that the drifts are irreversible, they will have an impact on the total lifetime of the sensors. Figure 7.7 shows a SEM image of cracks on a device on the die that was used during the gas sensing measurements. The cracks were not present prior to the measurements and may be caused by differences in thermal expansion of the materials underneath the nanoparticle layer causing it to get deformed. Interestingly, this is the only device with visible cracks and no physical damage is observed with the SEM on any of the other devices on the same die. However, damage might still be present underneath the surface that is not detectable using the SEM, as the SEM only provides surface level information as described in chapter 3.

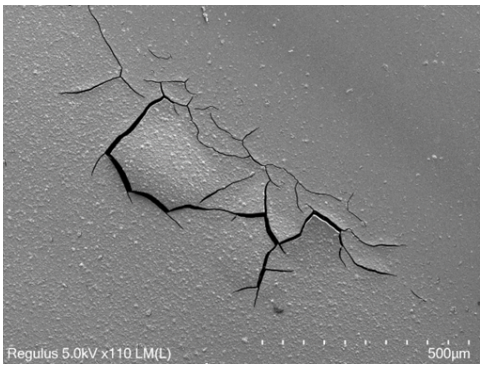

Figure 7.7: SEM image of cracks detected on device W02G10 after several gas sensing experiments have been performed on the die, likely caused by differences in thermal expansion of the materials underneath (gold, silicon and silicon dioxide) resulting in deformations and cracks.

As explained in chapter 2, annealing is known for increasing the conductivity of metal oxide nanoparticle layers. Since one possibility is that the drifts in resistance during the experiments are caused by reduction in the amount of current paths, an additional annealing process at 500 °C for 2 hours has been applied to the die for which the drifts were detected. An experiment comparing device behavior before and after annealing has not been performed due to the limited availability of the equipment, but the results in the following chapters should be able to prove whether annealing can result in reduction of drifts or reversal of resistance shifts.

7.3.3. Geometry Comparison Experiments

As mentioned in the beginning of this chapter, most of the probe needles in the chamber had alignment issues and required repair work. All previous experiments have therefore been performed on single devices by shifting the die according to a pair of needles that did align properly. Repair work on the needles has been performed, providing the opportunity to do experiments on multiple devices simultaneously. This method

is expected to provide data that is more suitable for making comparisons between devices than single device measurements, as all measured devices are exposed to similar conditions in terms of gas, temperature and humidity at the same time. There is a downside of such simultaneous measurements, however, as the number of data points obtained per device will be less compared to single device measurements. With the channel switching frequency of 2 Hz of the multiplexer, an experiment with 20 devices would provide a measurement frequency of 0.1 Hz for each device.

After the previously mentioned annealing process has been performed on the die that experienced resistance drifts, and repair work has been performed on the probe needles in the chamber, an experiment with ethanol gas has been performed on 13 devices simultaneously. The resistance curves obtained from this experiment are shown in appendix D. The results of two devices among the 13, of which the electrode width and gap size is equal but the sensing area is different, are shown in figure 7.8. There is a significant difference in response towards 20 ppm of ethanol gas, which is 12% in figure 7.8a and 55% in 7.8b. There seems to be noise present in both figures, with a period of around 13-15 minutes. Despite the dependence of the resistance of SnO_2 to temperature (as observed in chapter 6), it is unlikely that this noise is caused by fluctuations in temperature, as the period of temperature fluctuations is in seconds rather than minutes. Changes in target gas concentration can also not be the source of the shown noise, as it is also present during the absence of the gas during recovery. A possible cause for the noise is variations in humidity. Despite the relative humidity being set to 30% throughout all ethanol experiments, the accuracy is defined as ±1% according to the datasheet of the humidity generator used in the setup [63]. The drift in resistance is present for both devices, and also for most of the other 11 measured devices, suggesting that the annealing step might have not have reverted damage.

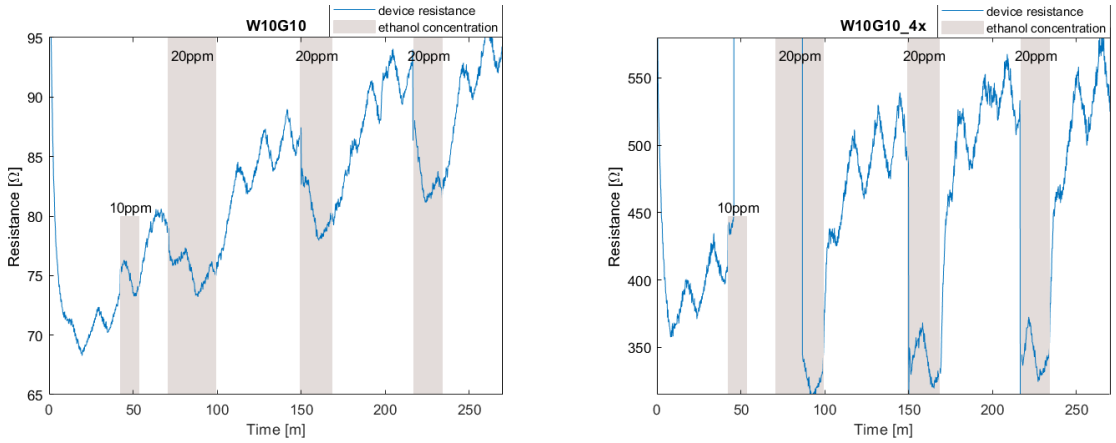

(a) 1x1mm

(b) 4x1mm

Figure 7.8: 2 out of 13 devices (appendix D) which are exposed to ethanol gas simultaneously. Both devices have similar electrode widths (10 μm) and gap sizes (10 μm). In terms of geometry the only difference between the devices is their sensing area (1 mm^2 vs 4 mm^2). The response of the 4 mm^2 device (55%) is significantly higher than the 1 mm^2 device (12%). An upwards drift is present for both devices.

Since it is assumed that devices have gotten damaged during operation and the annealing process may not have reverted it, and therefore the obtained data might not be reliable for device comparisons, an additional experiment has been performed with a new, previously unused set of devices. Two devices are exposed to different concentrations of ethanol as shown in figure 7.9. Periodic fluctuations in resistance are also present here, but the magnitude seems to differ here between the devices and suggests that there is difference in sensitivity towards humidity between the devices. It is unclear what causes the spike at minute 25, but it is likely setup related as it occurs for both devices. The spike makes it more difficult to obtain the response towards 20 ppm of ethanol for these devices, but with interpolation a value for response is still obtained that may give an indication regarding sensing performance. Because of the noise, it is not be confirmed whether there is a resistance drift in figure 7.9b or not. However, it can be seen in figure 7.9a that the drift is less than most of the results shown in appendix D, suggesting that the resistance drifts increase as devices are operated over time.

To find a relation between electrode geometry and gas response, the responses obtained from all measure-

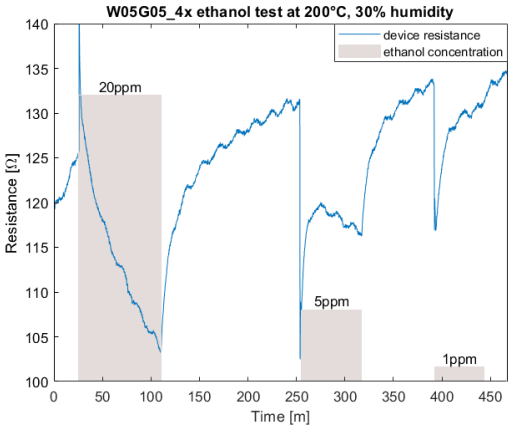

(a) Width 5μm, gap 5μm, (interpolated) response 17% for 20 ppm.

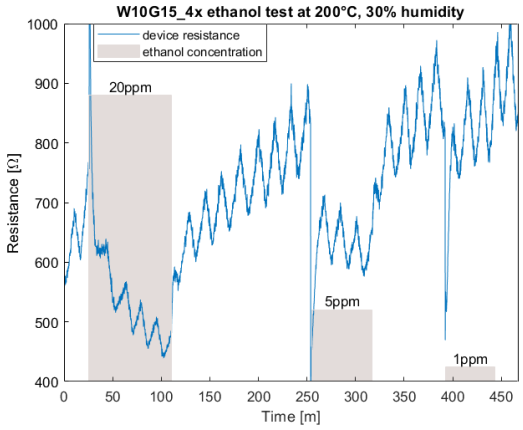

(b) Width 10μm, gap 15μm, (interpolated) response 67% for 20 ppm.

Figure 7.9: Two previously unused devices operating at the same time, exposed to different concentrations of ethanol. There are significant differences between the devices in terms of response and noise (presumably due to sensitivity towards humidity). The spike at minute 25 is likely related to the setup itself as it occurs for both devices.

ments towards 20 ppm ethanol in this chapter have been compiled and plotted over electrode dimensions in figure 7.10. The response values written in red are obtained from the single device measurements performed right in section 7.3.1, the values in black are obtained from appendix D after the additional annealing step, and the values in green belong to the new devices that were not operated before. While there are significant differences in response between devices, no clear relation between electrode width or gap size and response towards ethanol is observed. The differences in response per device are likely caused by variations in nanoparticle layers, despite the printing settings being similar for all devices (chapter 6). Larger responses are achieved for the values in red and green, meaning that devices that have been operated for a longer time are less sensitive to ethanol. It can also be confirmed from the plots that larger devices (figure 7.10b) have on average a higher sensitivity compared to the smaller devices (figure 7.10a) due to their larger specific surface area allowing more gas molecules to cause a change in resistance.

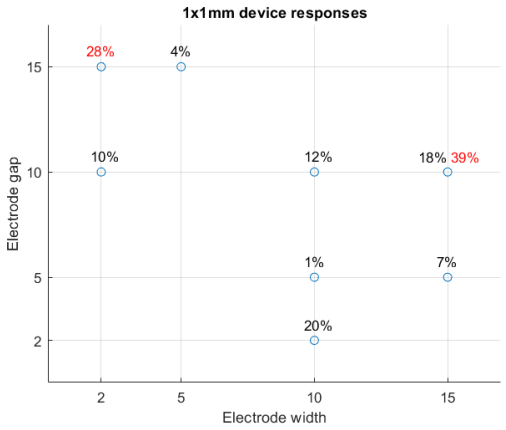

(a) 1x1mm devices.

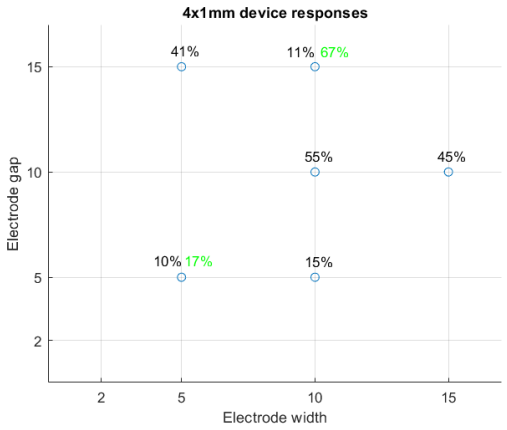

(b) 4x1mm devices.

Figure 7.10: 20 ppm ethanol response data over electrode dimensions compiled from measurements in this chapter and in appendix D.

7.4. Discussion

The gas sensing experiments in this chapter showed that detection of humidity, NO_2 and ethanol has been successful using most of the interdigitated geometries with SnO_2. Despite sensitivity towards humidity being regarded as a disadvantage for gas sensors in general, a very high sensitivity is observed for 35% humidity, meaning that perhaps the devices fabricated in this thesis might be suitable for humidity sensing. Drift is

observed during pretty much all measurements and the source of it is not clear. Some of the possible sources according to literature are reorganization of the sensor surface over time or irreversible (or slowly reversible) contamination. It is very unlikely that oxidation of the nanoparticles is still occurring during measurements, as it became clear from chapter 6 that no changes in the material composition occurs during an additional annealing step at 500 °C. As an attempt to restore the conductivity caused by these drifts, the devices were annealed again after usage. It does not seem like the annealing step resulted in any reversal of these drifts as the gas responses ended up to be lower compared to newly fabricated devices.

From the obtained results, there seems to be no relation between electrode geometry and gas response, suggesting that the range within electrode widths and gap sizes are varied (2-15 μm) is not sufficient to observe a difference, or that variations in deposition between devices might be dominating. The gas sensitivity of some of the devices, most notably the ones that have not experienced aging or contamination related drifts yet, does not seem to be far off from those of similar devices in literature, and even seem to outperform some. For example, Kennedy et al. [71] presented a 1x1 mm tin oxide nanoparticle sensor with interdigitated electrodes with widths and gap sizes of 2 μm with a sensitivity of 35% towards 100 ppm ethanol at 250 °C. A higher sensitivity is achieved in this thesis using a device with a similar area and operating temperature towards an even lower concentration of ethanol (20 ppm) as shown in figure 7.5. Lu et al. [17] cite the work of Kennedy et al. and claim to have a higher sensitivity and faster response time due to smaller particle sizes and narrower electrode gaps.

It is indeed known that smaller particles sizes provide a higher sensitivity and faster response time, since the response depends on the number of reactions on the surface and smaller particles provide a larger specific surface area [72]. The results in this chapter show that the devices do suffer from long response times, in some cases even hours long. From SEM inspection, the particle size in this work seems to be around 20 nm. Since the focus was on high nanoparticle coverage and uniformity when choosing printing parameters in chapter 6, perhaps higher responses and smaller recovery times would have been achieved if particle size would also have been taken into account. It is believed that the nanoparticle size is (one of) the limitation(s) since no correlation is found in this chapter between electrode geometry and gas response. A higher operating temperature is also expected to improve the recovery time as recovery is a process known to be dependent on temperature. However, this was not possible in this work as parts in the sensing chamber are not able to withstand high temperatures without getting damaged.

8

Conclusion & Recommendations

Metal oxide semiconductor gas sensors are widely used for their various advantages, including their low costs, low complexity, and high sensitivity towards a wide range of gases. SnO_2, ZnO and CuO are among the most commonly used metal oxides for gas sensors and are used in the form of nanoparticles in order to maintain a high specific surface area. There are various methods for generating such nanoparticles, with each having their advantages and disadvantages. The focus of this study is on the gas sensing performance of metal oxide nanoparticles generated using spark ablation. First chemFETs are designed and fabricated. Each designed device has an interdigitated electrode structure with varying widths and gap sizes to test the effect of electrode geometry on the gas sensing performance. The main difference between chemiresistors and the devices fabricated in this thesis is the fact that a third terminal is added for gate biasing. Using a trial-and-error approach, nanoparticle deposition settings are optimized for achieving high coverage, uniformity and conductance for SnO_2, ZnO and CuO layers. Gas sensing experiments are performed using devices with SnO_2 only, as the lab equipment has limited availability and SnO_2 showed the highest conductivity among the tested metal oxides.

Sensitivity values are obtained towards ethanol that are comparable to devices with similar sizes in literature, proving that spark ablated nanoparticles can be a viable alternative to other nanoparticle generation methods. Towards 20 ppm of ethanol, a maximum sensitivity of 39% and 67% is achieved using a 1x1 mm and 4x1 mm device respectively. There is no correlation found between different electrode widths and gaps (varied between 2-15 μm) and gas response, and it is assumed that differences in response are caused by differences between nanoparticle depositions. The SnO_2 devices seem to have a very high sensitivity towards changes in humidity (1300% for 35% RH). Drifts in resistance are also observed over time for a majority of the devices, most likely caused by aging or irreversible contamination. The devices seem to suffer from long recovery times, which can be reduced with a higher operating temperature if the measurement setup would be able to withstand that. Smaller particle sizes also lead to higher responses and faster response times. As it is observed that the particle sizes in this thesis are around 20 nm, perhaps different deposition settings would have provided higher responses and faster recovery times. Gate biasing only resulted in an increase in conductivity for devices with SnO_2 operated at room temperature. It did not result in any notable improvements for elevated temperatures. However, since very low resistances are achieved at 200 $°C$ (~100 Ω), potential improvements caused by gate biasing are not expected to improve the gas sensing performance significantly.

This work proves that spark ablated nanoparticles can be a viable alternative to metal oxides generated using other methods, and since the focus has been on pure, undoped or non-decorated metal oxides, there is room for improvement for potential future work. It is proven in literature that the addition of dopants (usually noble metals) to metal oxide nanoparticles can provide significant advantages in terms of gas response [6]. The incorporation of two or more metal oxides to form so-called heterojunctions is a method that can provide complementary advantages and can therefore improve both sensitivity and selectivity [14]. Since one of the major issues with the devices fabricated in this work is the drift in resistance, and the source of this resistance still remains unknown, perhaps fabricating and using similar devices in a cleaner environment could prove if contamination is an influencing factor in the drift. Since the measurement setup in this work is limited in achievable temperatures, the effect of operating temperature on recovery time can be studied with a setup that is able to withstand higher temperatures. To find the correlation between electrode geometry and gas

response, perhaps a larger range of electrode widths and gaps could be tested.

A

Flowchart

A.1. Part 1: Cleaning Step

A.1.1. Cleaning Procedure: HNO3 100% and 65%

Cleaning:

- 10 minutes in fuming nitric acid (Merck: HNO3 100%) at ambient temperature.
- Use wet bench "HNO3 (100%)" and the carrier with the red dot.

QDR:

- Rinse in the Quick Dump Rinser with the standard program until the resistivity is $5 M\Omega$.

Cleaning:

- 10 minutes in concentrated nitric acid (Merck: HNO3 65%) at 110 °C.
- Use wet bench "HNO3 (65%)" and the carrier with the red dot.

QDR:

- Rinse in the Quick Dump Rinser with the standard program until the resistivity is $5 M\Omega$

Drying:

- Use the Semitool "rinser/dryer" with the standard program, and the white carrier with a red dot.

A.2. Part 2: Creation of Zero Layer

A.2.1. Coating and Baking

Use the EVG 120 wafertrack to coat the wafers with resist, and follow the instructions specified for this equipment.

The process consists of a treatment with HMDS (hexamethyldisilazane) vapor with nitrogen as a carrier gas, spin coating with Shipley SPR3012 positive photoresist, and a soft bake at 95degC for 90 seconds.

Always check the temperature of the hotplate and the relative humidity (48 ± 2 %) in the room first.

Use coating **Co – SPR3012-1.4um – no-EBR** (resist thickness: 1.400 µm).

A.2.2. Alignment and Exposure

Processing will be performed on the ASM PAS 5500/80 automatic waferstepper.

Follow the operating instructions from the manual when using this machine.

Use **COMURK mask**.
1st Job: litho/20-20 COMURK0.0, 120 mJ/cm2
2nd Job: litho/fwamtoze, 120 mJ/cm2

A.2.3. Development

Use the EVG 120 wafertrack to develop the wafers, and follow the instructions specified for this equipment. The process consists of a post-exposure bake at 115 degC for 90 seconds, followed by a development step using
Shipley MF322 developer (single puddle process), and a hard bake at 100 degC for 90 seconds.
Always check the temperature of the hotplates first.

A.2.4. Inspection: Linewidth

Visually inspect the wafers through a microscope, and check the linewidth. No resist residues are allowed.

A.2.5. Plasma Etching of Alignment Marks

Use the Trikon Omega 201 plasma etcher and follow the operating instructions from the manual when using this machine.

The process conditions of the etch program may not be changed!

Use sequence URK_NPD and set the platen temperature to 20 °C to etch 1200 Å deep ASM URK's into the silicon

A.2.6. Cleaning Procedure: Tepla + HNO3 100% + 65%

Plasma strip:

- Use the Tepla plasma system to remove the photoresist in an oxygen plasma.
- Follow the instructions specified for the Tepla stripper, and use the quartz carrier.
- Use program 1

Cleaning:

- 10 minutes in fuming nitric acid (Merck: HNO3 100%) at ambient temperature.
- Use wet bench "HNO3 (100%)" and the carrier with the red dot.

QDR:

- Rinse in the Quick Dump Rinser with the standard program until the resistivity is 5 $M\Omega$.

Cleaning:

- 10 minutes in concentrated nitric acid (Merck: HNO3 65%) at 110 °C.
- Use wet bench "HNO3 (65%)" and the carrier with the red dot.

QDR:

- Rinse in the Quick Dump Rinser with the standard program until the resistivity is 5 $M\Omega$.

Drying:

- Use the Semitool "rinser/dryer" with the standard program, and the white carrier with a red dot.

A.3. Part 3: Oxidation

A.3.1. Oxidation

Furnace no: C1 or D1
Program name: WET1000

PROCESS	TEMPERATURE (in °C)	GASES & FLOWS (in liter/min)	TIME (in minutes)	REMARKS
boat in	600	nitrogen: 6.0	5	
stabilize	600	nitrogen: 6.0	10	
anneal	600	nitrogen: 6.0	15	
heat up	+10 °C/min	nitrogen: 3.0 oxygen: 0.3	40	
stabilize	1000	nitrogen: 3.0 oxygen: 0.3	2	
oxidation	1000	oxygen: 2.25 hydrogen: 3.85	10:04	Target 100nm oxide thickness
cool down	-7 °C/min	oxygen: 2.25 hydrogen: 3.85	60	
boat out	600	nitrogen: 3.0	5	

A.3.2. Measurement: Oxide Thickness

Use the Leitz MPV-SP measurement system to measure the oxide thickness:

Program: Th. SiO2 on Si, >50nm auto5pts

Oxide thickness: 100 nm on the process wafers

A.4. Part 4: Substrate Contact

A.4.1. Coating and Baking

Use the EVG 120 wafertrack to coat the wafers with resist, and follow the instructions specified for this equipment.

The process consists of a treatment with HMDS (hexamethyldisilazane) vapor with nitrogen as a carrier gas, spin coating with Shipley SPR3012 positive photoresist, and a soft bake at 95degC for 90 seconds.

Always check the temperature of the hotplate and the relative humidity (48 ± 2 %) in the room first.
Use coating **Co –SPR3012-1,4um- no-EBR** (resist thickness: 1.400 µm).

A.4.2. Alignment and Exposure

Processing will be performed on the MA8 and follow the operating instructions from the manual when using this machine.

Mask: substrate contacts (foil mask)

Exposure time: check logbook (140 mJ equivalent)

A.4.3. Development

Use the EVG 120 wafertrack to develop the wafers, and follow the instructions specified for this equipment. The process consists of a post-exposure bake at 115 degC for 90 seconds, followed by a development step using Shipley MF322 developer (double puddle process), and a hard bake at 100 degC for 90 seconds. Always check the temperature of the hotplates first.

Use development program Dev – SP

A.4.4. Inspection
Visually inspect the wafers through a microscope, and check openings.

A.4.5. Plasma Etching of Substrate Contacts
Use the Drytek Triode 384T and follow the operating instructions from the manual when using this machine.

Use the recipe stdoxide and check the logbook for the etching rate, typ 8-10 mm/s

A.4.6. Cleaning Procedure: Tepla + HNO3 100% + 65%
Plasma strip:

- Use the Tepla plasma system to remove the photoresist in an oxygen plasma.
- Follow the instructions specified for the Tepla stripper, and use the quartz carrier.
- Use program 1

Cleaning:

- 10 minutes in fuming nitric acid (Merck: HNO3 100%) at ambient temperature.
- Use wet bench "HNO3 (100%)" and the carrier with the red dot.

QDR:

- Rinse in the Quick Dump Rinser with the standard program until the resistivity is 5 $M\Omega$.

Cleaning:

- 10 minutes in concentrated nitric acid (Merck: HNO3 65%) at 110 $°C$.
- Use wet bench "HNO3 (65%)" and the carrier with the red dot.

QDR:

- Rinse in the Quick Dump Rinser with the standard program until the resistivity is 5 $M\Omega$.

Drying:

- Use the Semitool "rinser/dryer" with the standard program, and the white carrier with a red dot.

A.5. Part 5: Metalization
A.5.1. Coating and Baking
Use the EVG 120 wafertrack to coat the wafers with resist, and follow the instructions specified for this equipment.

The process consists of a treatment with HMDS (hexamethyldisilazane) vapor with nitrogen as a carrier gas, spin coating with AZ NLOF2020 negative photoresist, and a soft bake at 95degC for 90 seconds.

Always check the temperature of the hotplate and the relative humidity (48 ± 2 %) in the room first.

Use coating Co –nlof2020 – 3,5um – no EBR (resist thickness: 3.500 µm).

A.5.2. Alignment and Exposure
Processing will be performed on the EVG420 and follow the operating instructions from the manual when using this machine.

Mask: metal contacts (glass mask)

Exposure time: check logbook (55 mJ equivalent)

A.5.3. Development
Use the EVG 120 wafertrack to develop the wafers, and follow the instructions specified for this equipment.

The process consists of a post-exposure bake at 115 degC for 90 seconds, followed by a development step using Shipley MF322 developer (double puddle process), and a hard bake at 100 degC for 90 seconds.

Always check the temperature of the hotplates first.

Use development **program Dev – Only X-link Bake**

Use development **program xDens-Dev-Lift-Off**

A.5.4. Inspection
Visually inspect the wafers through a microscope, and check openings.

A.5.5. Native Oxide Removal: Triton X100 + HF
Dip the wafers in Triton X100 (Si Etching Line). Time: 60 sec.

Use 0.55% HF for 4 min to remove the native oxide.

Use the QDR and dry using the dryer in the etching line.

A.5.6. Cr/Au evaporation
This step should be performed within 30 min of the previous step!

Use the CHA evaporator in CR10000 to deposit 10/100 nm of Cr/Au. Contaminated after this step.

A.5.7. Lift-off
Perform lift-off in SAL using NMP heated bain-marie to 70°C in an ultrasonic bath. Apply ultrasonic till all Au is removed from the areas it should be lifted off. Rinse in DI water for 5 min and dry the wafers using the contaminated chuck.

Use dedicated beakers for lift-off

A.5.8. HNO3 Cleaning Procedure
Manually clean the wafers in SAL by using contaminated 99% HNO3 to remove organic residues. Rinse the wafers with water for 5 minutes afterwards. Dry the wafers in the spinner using the contaminated chuck.

A.6. Part 6: Passivation Layer
A.6.1. SiO2 CVD
Location: Kavli Equipment: PlasmaLab 80 Recipe:?

This will be done by PhD students who have access to Kavli Lab.

A.6.2. Manual Coating and Baking
Use the Convac Spinner MEMS in the Polymer Lab to manually coat the wafers with resist, and follow the instructions specified for this equipment.

The coating is done with Shipley SPR3012 positive photoresist with a thickness of 2.1µm, spin speed of 1500rpm, and a spin time of 30-60 sec (online calculator http://www.laurell.com/support/spin-speed-calculator.php), and a soft bake at 95 °C for 90 seconds.

Use the chuck for Cu contaminated samples and the hotplate for contaminated wafers

A.6.3. Alignment and Exposure
Processing will be performed on the EVG420 and follow the operating instructions from the manual when using this machine.

Use the contaminated chuck.

Mask: passivation (glass mask)

Exposure time: 300mj/cm2 (exposure time: check calibration log of Suss s) Always check the corresponding exposure energy with the thickness of the photoresist.

A.6.4. Manual Development
Use a hotplate to manually develop the wafers.

Post-exposure bake: 115 ^{o}C for 60 seconds on hotplate for contaminated wafers.

Development: Shipley MF322 developer for 60 sec.

Hard bake: 100 ^{o}C for 90 seconds on hotplate for contaminated wafers.

A.6.5. Inspection
Visually inspect the wafers through a microscope, and check openings. Put a tissue underneath the wafer.

A.6.6. Wet Etching of Passivation Layer
Use the wet bench for red metals in SAL to etch SiO2 by using BHF(1:7). Rinse the wafers with water for 5 minutes afterwards. Dry the wafers in the spinner using the contaminated chuck.

A.6.7. Manual Cleaning Procedure
Manually clean the wafers in SAL by using acetone to strip the photoresist. Rinse the wafers with water for 5 minutes afterwards. Dry the wafers in the spinner using the contaminated chuck.

B

Conductance Data

B.1. Design A with SnO2

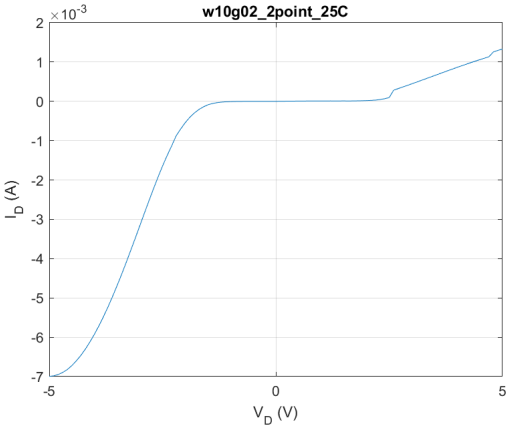

Figure B.1: W10G02

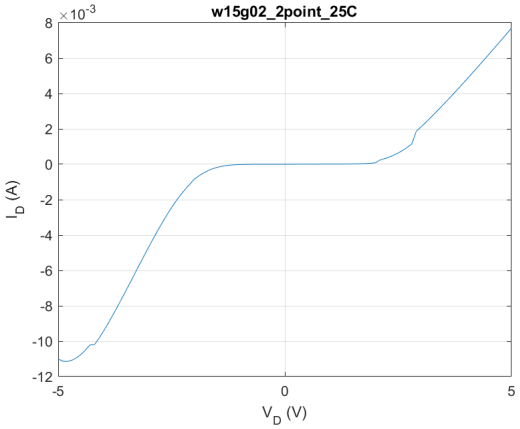

Figure B.2: W15G02

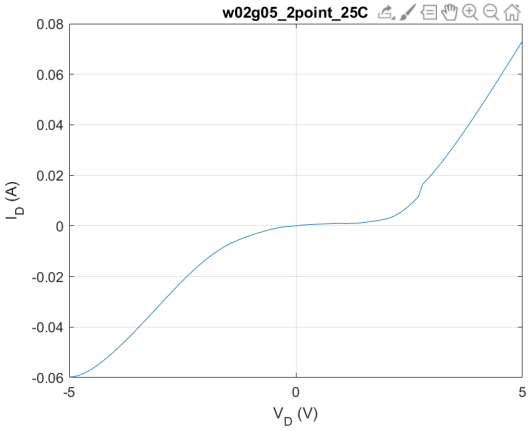

Figure B.3: W02G05

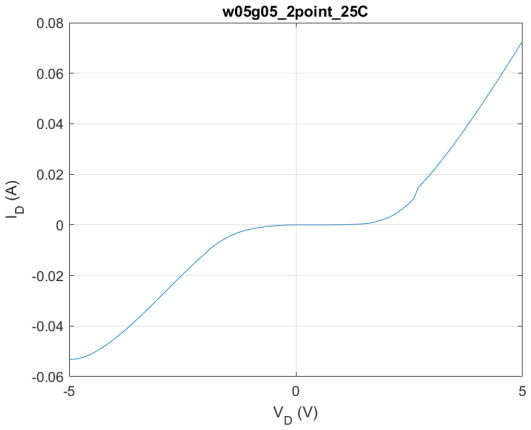

Figure B.4: W05G05

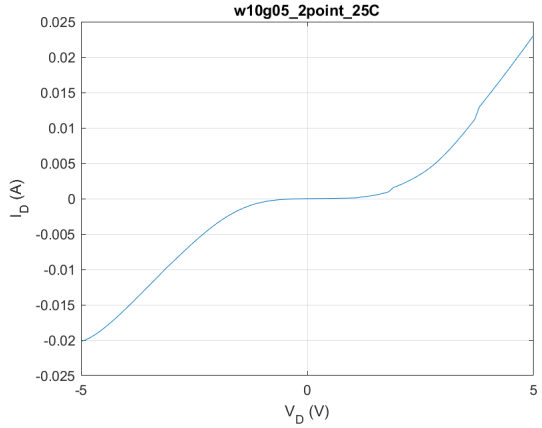

Figure B.5: W10G05

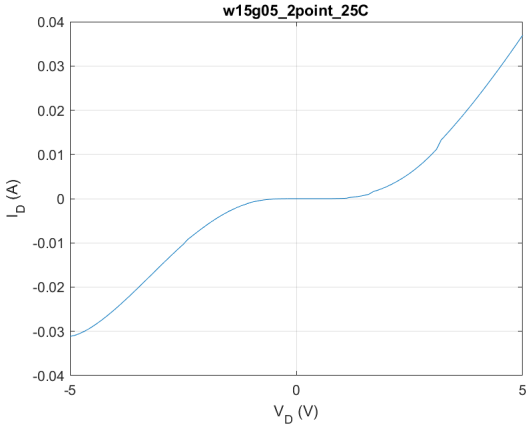

Figure B.6: W15G05

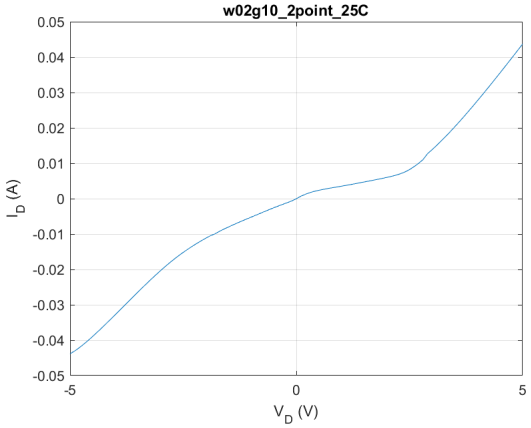

Figure B.7: W02G10

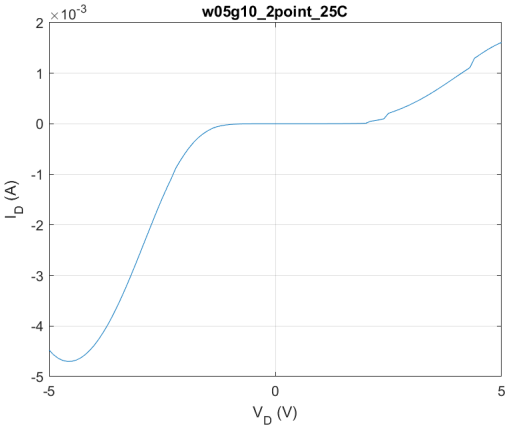

Figure B.8: W05G10

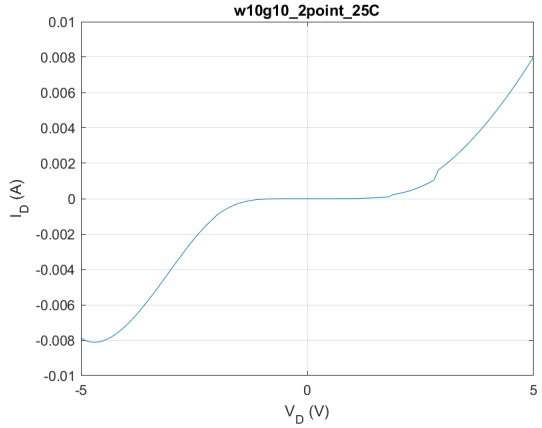

Figure B.9: W10G10

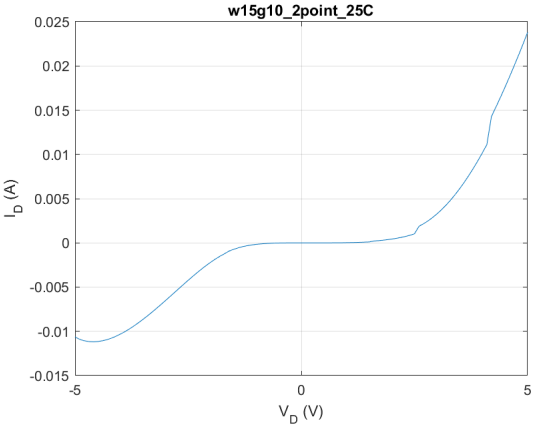

Figure B.10: W15G10

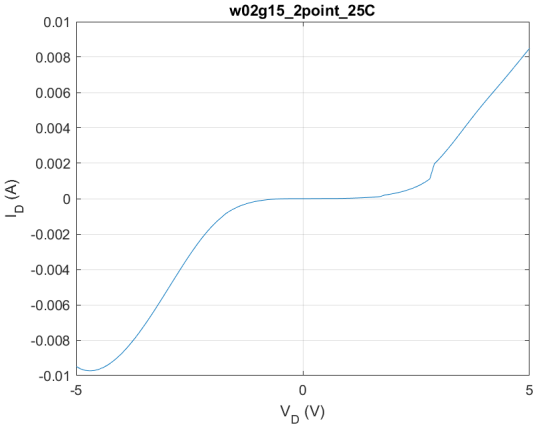

Figure B.11: W02G15

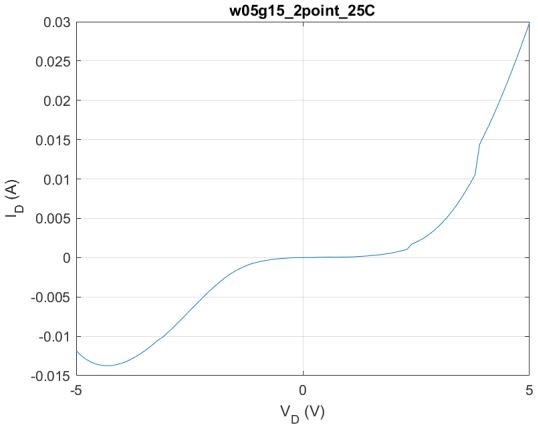

Figure B.12: W05G15

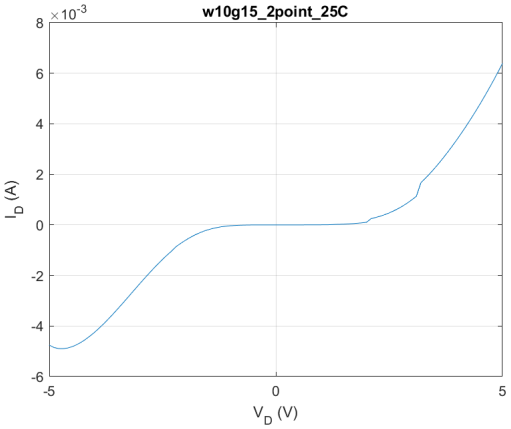

Figure B.13: W10G15

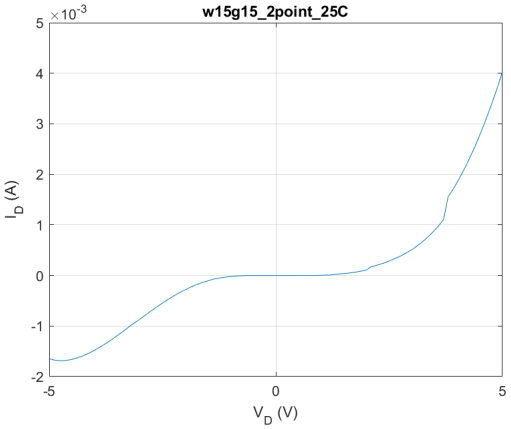

Figure B.14: W15G15

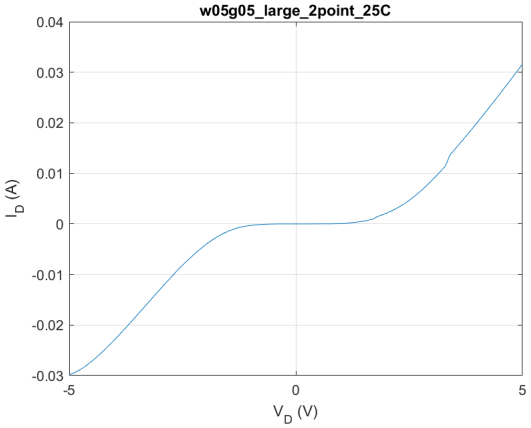

Figure B.15: W05G05 4x1mm

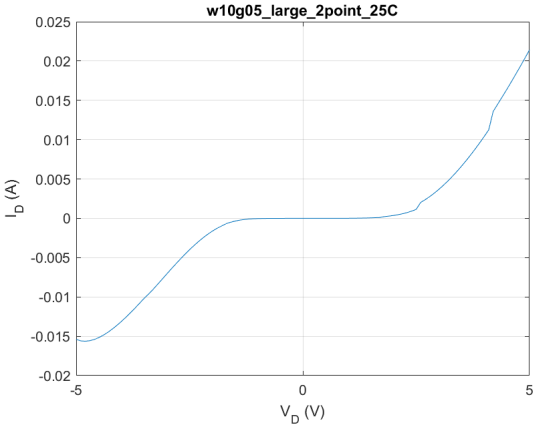

Figure B.16: W10G05 4x1mm

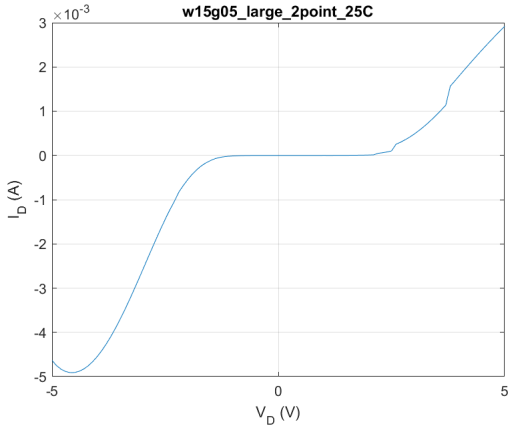

Figure B.17: W15G05 4x1mm

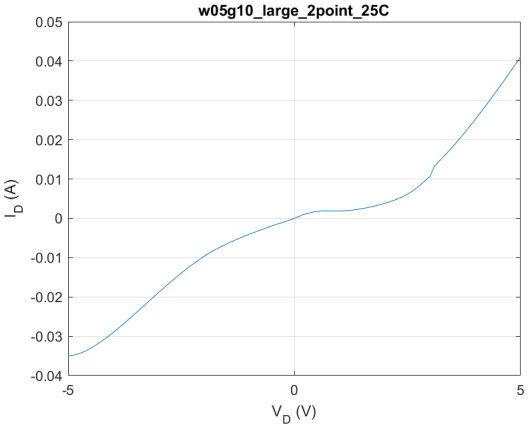

Figure B.18: W05G10 4x1mm

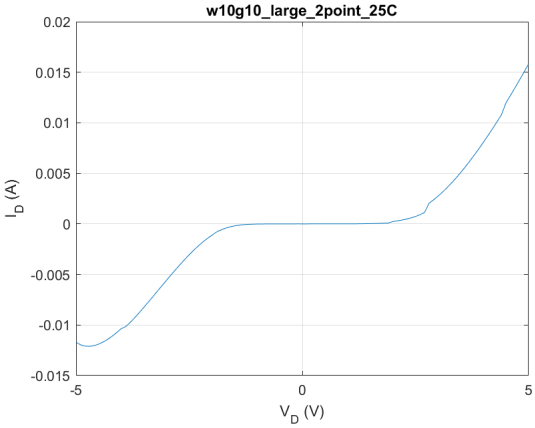

Figure B.19: W10G10 4x1mm

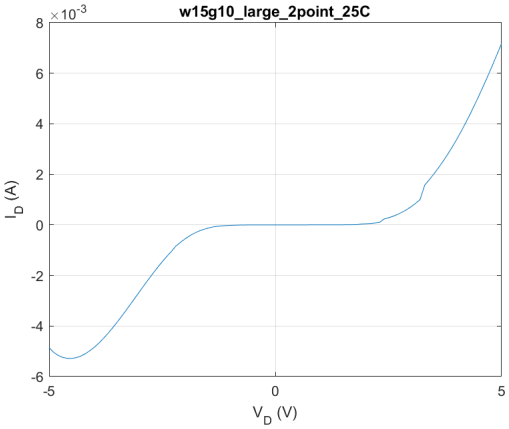

Figure B.20: W15G10 4x1mm

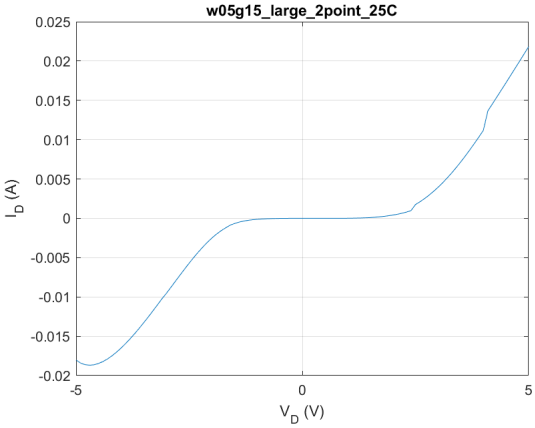

Figure B.21: W05G15 4x1mm

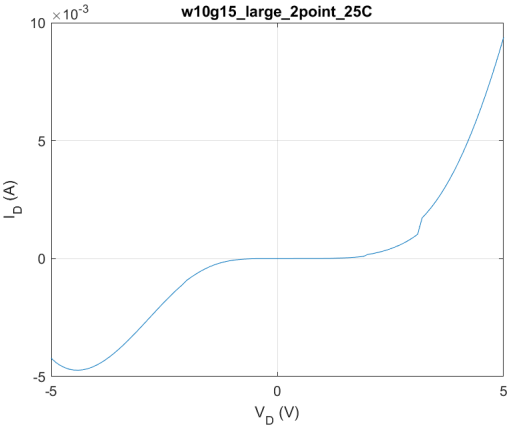

Figure B.22: W10G15 4x1mm

C

Lithography Mask Designs

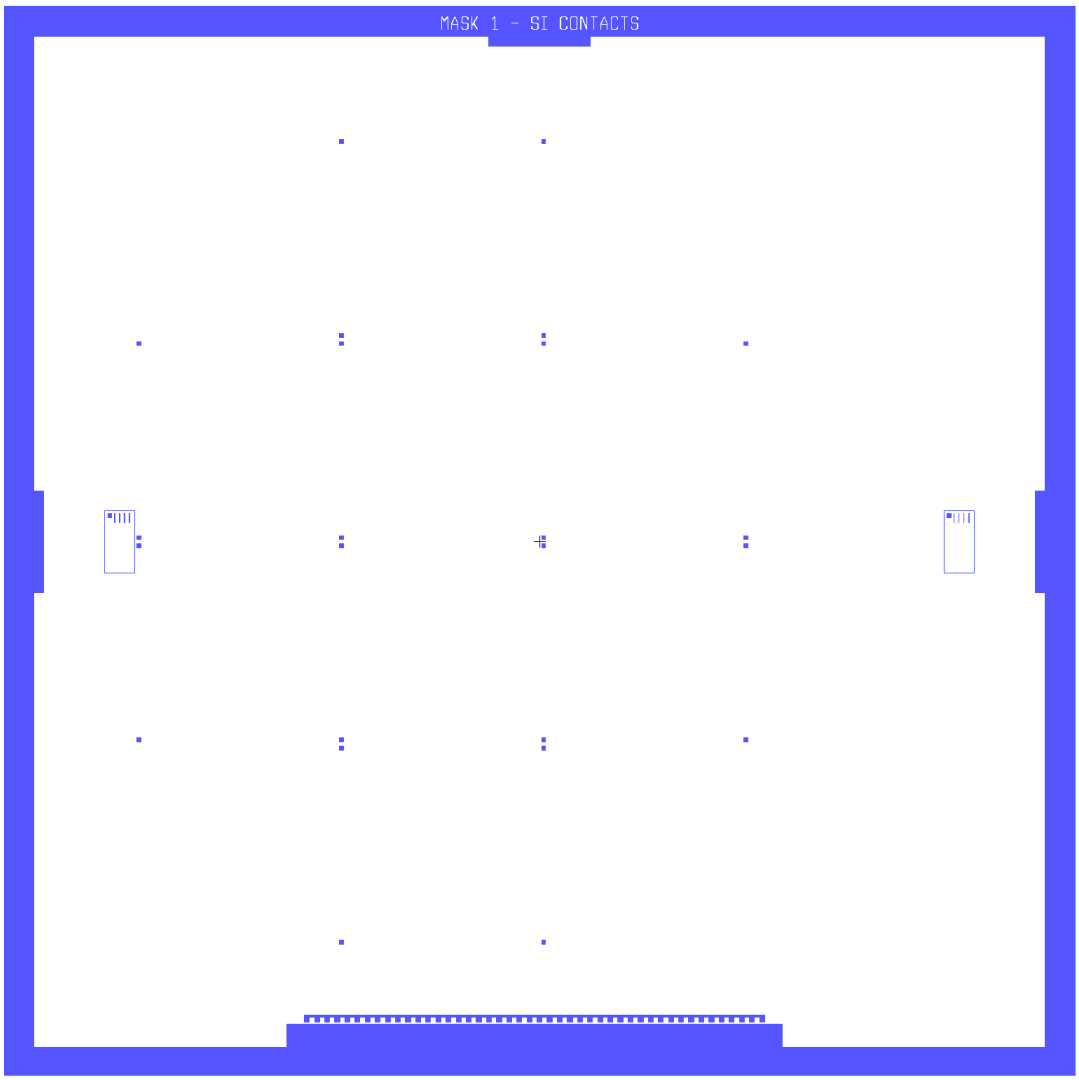

Figure C.1: Mask 1: Bias Contacts.

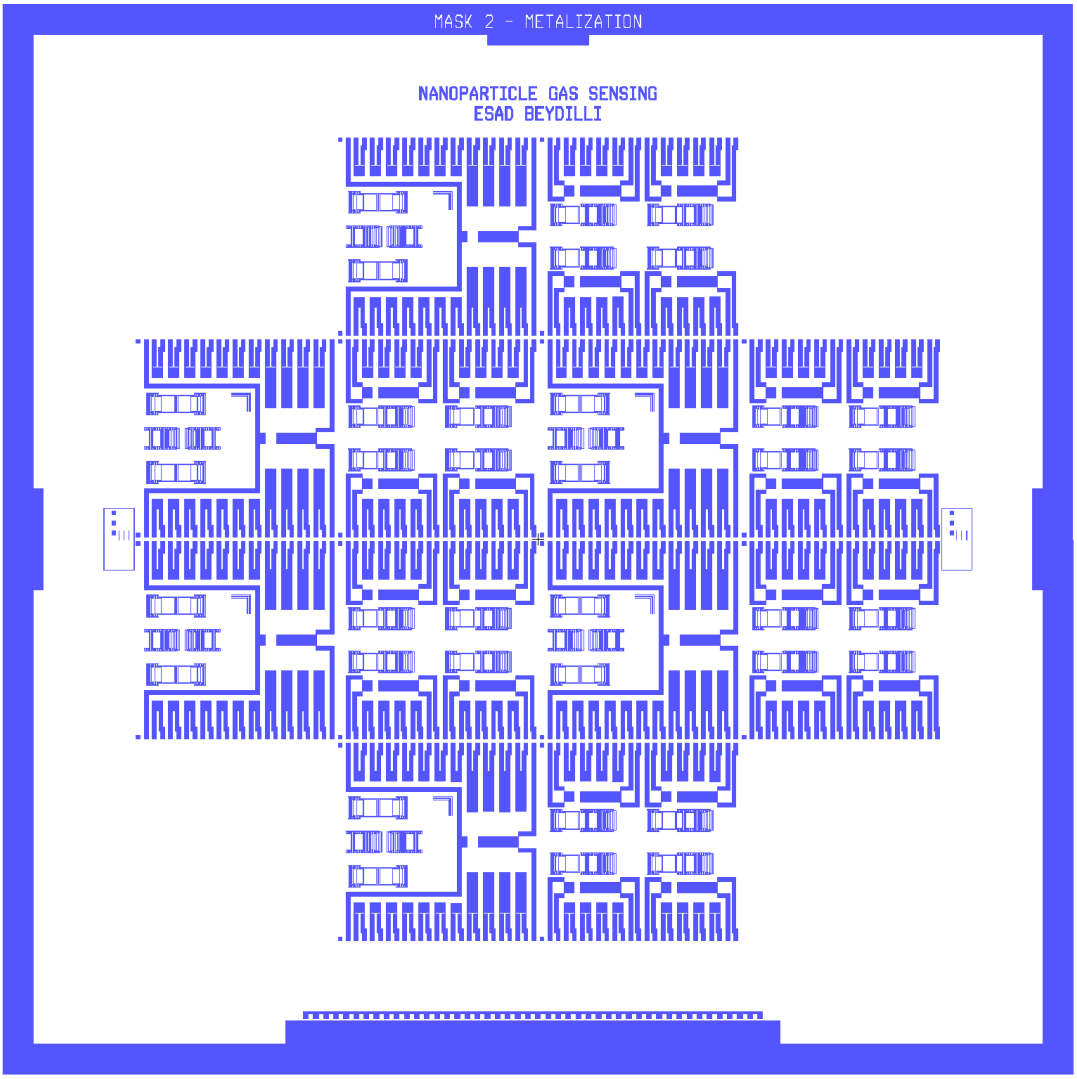

Figure C.2: Mask 2: Metallization.

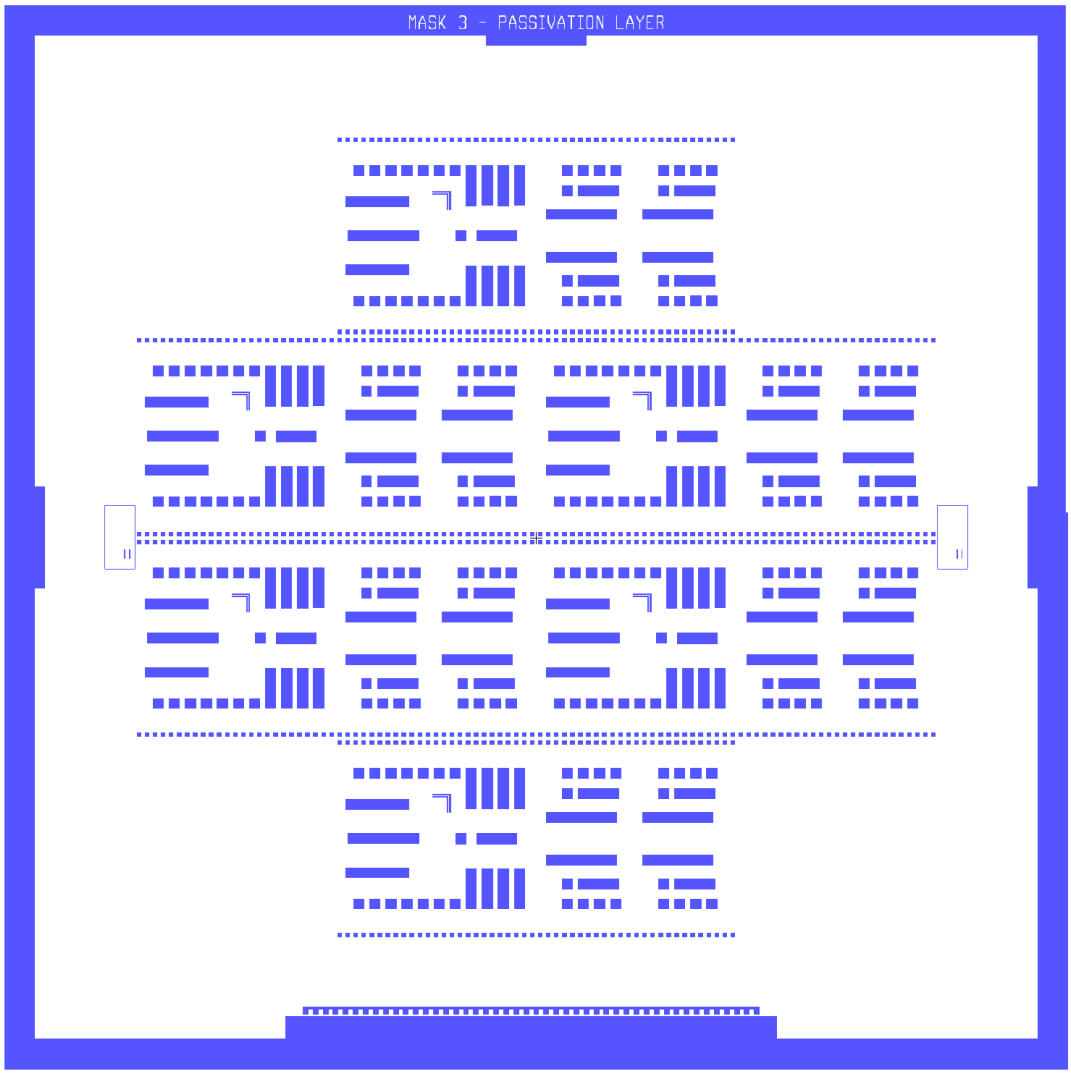

Figure C.3: Mask 3: Passivation Layer.

D

Ethanol Test Results

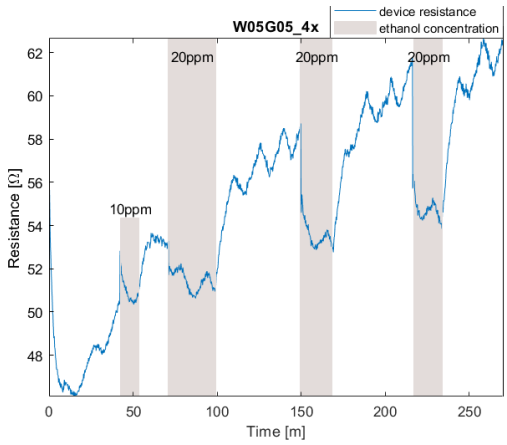

Figure D.1: Width 5μm, gap 5μm, response 10%.

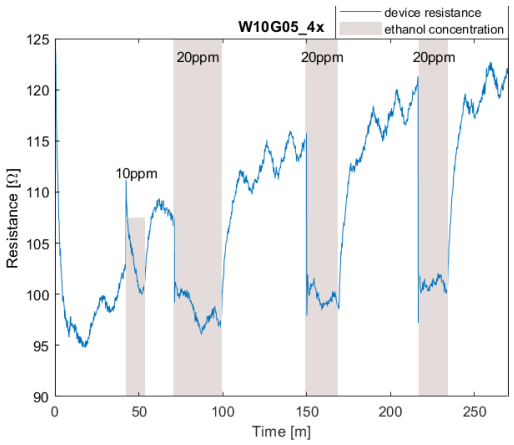

Figure D.2: Width 10μm, gap 5μm, response 15%.

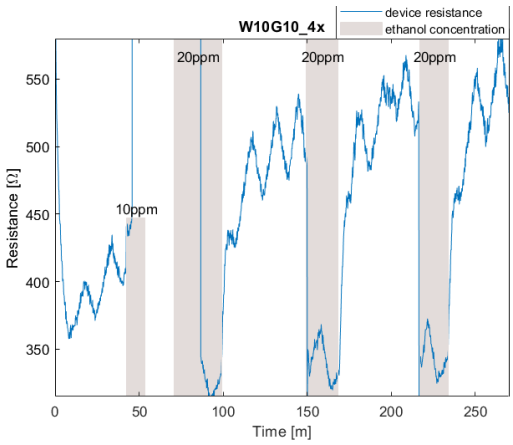

Figure D.3: Width 10μm, gap 10μm, response 55%.

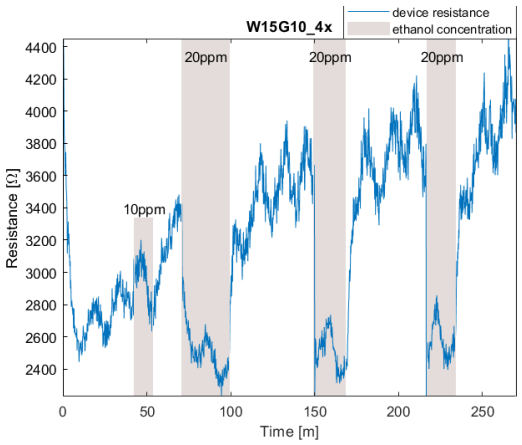

Figure D.4: Width 15μm, gap 10μm, response 45%.

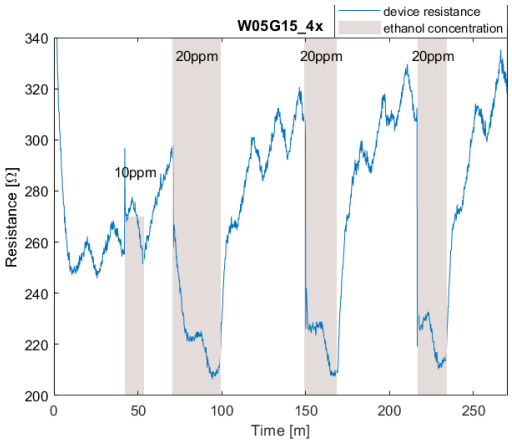

Figure D.5: Width 5μm, gap 15μm, response 41%.

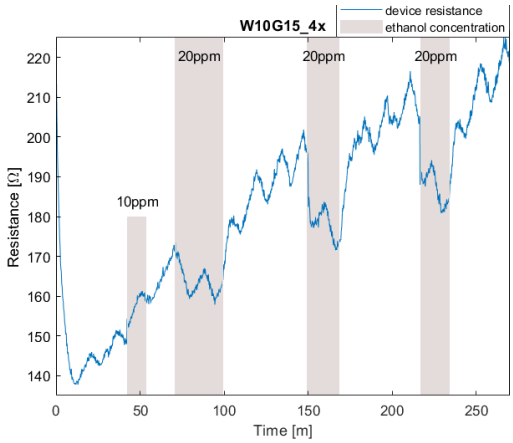

Figure D.6: Width 10μm, gap 15μm, response 11%.

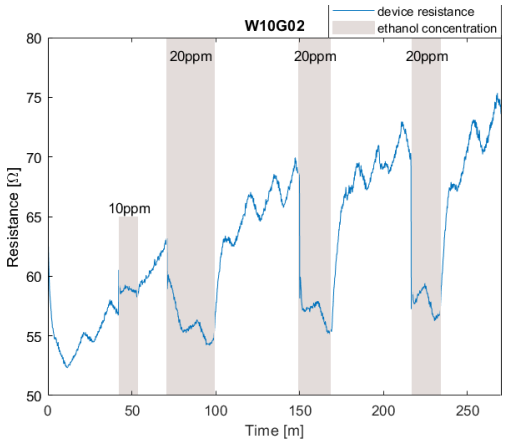

Figure D.7: Width 10μm, gap 2μm, response 20%.

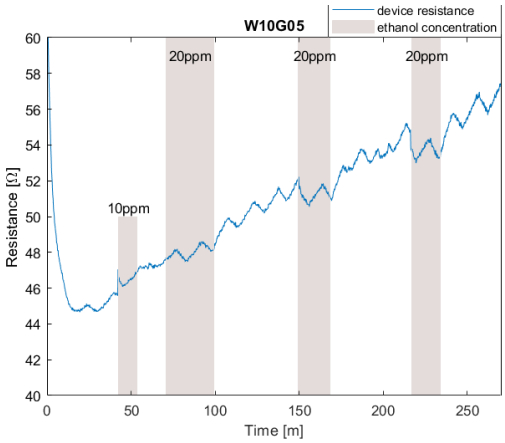

Figure D.8: Width 10μm, gap 5μm, response 0%.

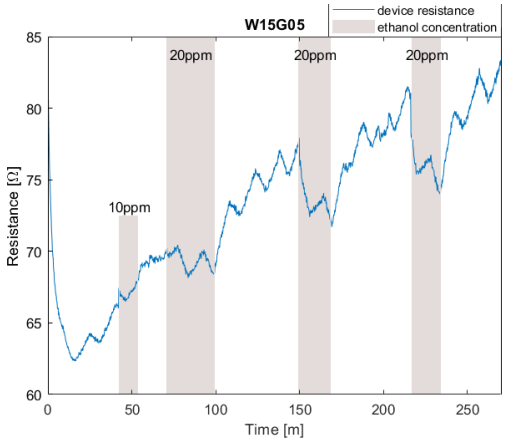

Figure D.9: Width 15μm, gap 5μm, response 7%.

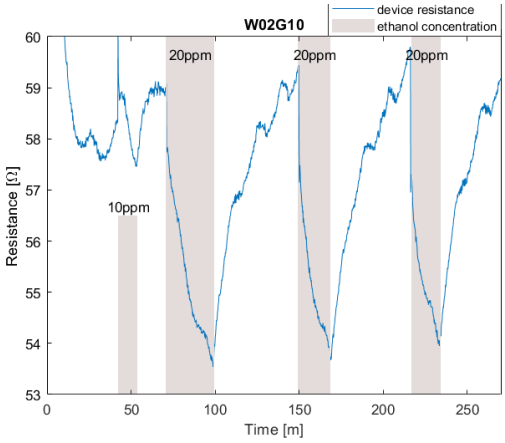

Figure D.10: Width 2μm, gap 10μm, response 10%.

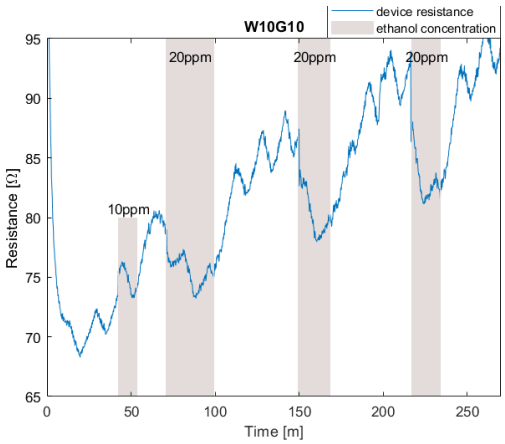

Figure D.11: Width 10μm, gap 10μm, response 12%.

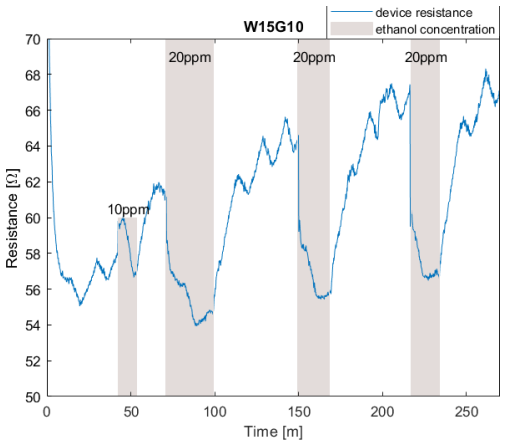

Figure D.12: Width 15μm, gap 10μm, response 18%.

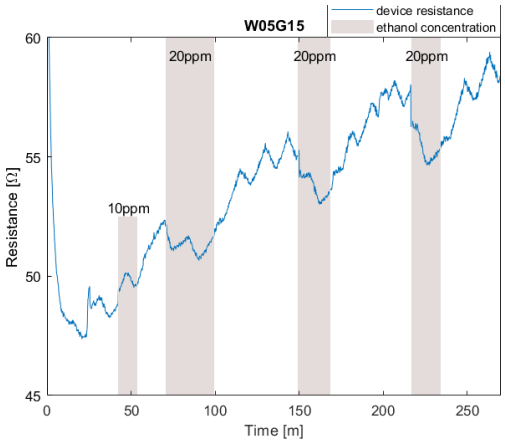

Figure D.13: Width 5μm, gap 15μm, response 4%.

Bibliography

[1] Erik Stokstad. Nitrogen crisis threatens dutch environment and economy. *Science*, 366(6470):1180–1181, 2019. doi: doi:10.1126/science.366.6470.1180. URL https://www.science.org/doi/abs/10.1126/science.366.6470.1180.

[2] Anne-Marije Andringa, Claudia Piliego, Ilias Katsouras, Paul W. M. Blom, and Dago M. de Leeuw. No2 detection and real-time sensing with field-effect transistors. *Chemistry of Materials*, 26(1):773–785, 2014. ISSN 0897-4756. doi: 10.1021/cm4020628. URL https://doi.org/10.1021/cm4020628.

[3] M. Ramachandrappa Venkatesh. *Functional materials for MEMS based gas sensors*. PhD thesis, Delft University of Technology, 2022.

[4] Andreas Schmidt-Ott. *Spark Ablation : Building Blocks for Nanotechnology*. Jenny Stanford Publishing, Singapore, 2020. ISBN 9789814800822 9781000730203 9781000730449. URL http://search.ebscohost.com/login.aspx?direct=true&db=nlebk&AN=2345843&site=ehost-live.

[5] Patrick T. Moseley. Progress in the development of semiconducting metal oxide gas sensors: a review. *Measurement Science and Technology*, 28(8):082001, 2017. ISSN 0957-0233 1361-6501. doi: 10.1088/1361-6501/aa7443. URL http://dx.doi.org/10.1088/1361-6501/aa7443.

[6] Haocheng Ji, Wen Zeng, and Yanqiong Li. Gas sensing mechanisms of metal oxide semiconductors: a focus review. *Nanoscale*, 11(47):22664–22684, 2019. ISSN 2040-3364. doi: 10.1039/C9NR07699A. URL http://dx.doi.org/10.1039/C9NR07699A.

[7] Maria Vesna Nikolic, Vladimir Milovanovic, Zorka Z. Vasiljevic, and Zoran Stamenkovic. Semiconductor gas sensors: Materials, technology, design, and application. *Sensors (Basel, Switzerland)*, 20(22):6694, 2020. ISSN 1424-8220. doi: 10.3390/s20226694. URL https://pubmed.ncbi.nlm.nih.gov/33238459https://www.ncbi.nlm.nih.gov/pmc/articles/PMC7700484/.

[8] Jian Zhang, Ziyu Qin, Dawen Zeng, and Changsheng Xie. Metal-oxide-semiconductor based gas sensors: screening, preparation, and integration. *Physical Chemistry Chemical Physics*, 19(9):6313–6329, 2017. ISSN 1463-9076. doi: 10.1039/C6CP07799D. URL http://dx.doi.org/10.1039/C6CP07799D.

[9] Avner Rothschild and Yigal Komem. The effect of grain size on the sensitivity of nanocrystalline metal-oxide gas sensors. *Journal of Applied Physics*, 95:6374–6380, 2004. doi: 10.1063/1.1728314.

[10] Min Ah Han, Hyun-Jong Kim, Hee Chul Lee, Jin-Seong Park, and Ho-Nyun Lee. Effects of porosity and particle size on the gas sensing properties of sno2 films. *Applied Surface Science*, 481:133–137, 2019. ISSN 0169-4332. doi: https://doi.org/10.1016/j.apsusc.2019.03.043. URL https://www.sciencedirect.com/science/article/pii/S0169433219306555.

[11] Chengxiang Wang, Longwei Yin, Luyuan Zhang, Dong Xiang, and Rui Gao. Metal oxide gas sensors: sensitivity and influencing factors. *Sensors (Basel, Switzerland)*, 10(3):2088–2106, 2010. ISSN 1424-8220. doi: 10.3390/s100302088. URL https://pubmed.ncbi.nlm.nih.gov/22294916https://www.ncbi.nlm.nih.gov/pmc/articles/PMC3264469/.

[12] A. N. Mallika, A. Ramachandra Reddy, and K. Venugopal Reddy. Annealing effects on the structural and optical properties of zno nanoparticles with pva and ca as chelating agents. *Journal of Advanced Ceramics*, 4(2):123–129, 2015. ISSN 2227-8508. doi: 10.1007/s40145-015-0142-4. URL https://doi.org/10.1007/s40145-015-0142-4.

[13] Pengxiang Song and Dongsheng Wen. Experimental investigation of the oxidation of tin nanoparticles. *The Journal of Physical Chemistry C*, 113(31):13470–13476, 2009. ISSN 1932-7447. doi: 10.1021/jp902580s. URL https://doi.org/10.1021/jp902580s.

[14] Derek R. Miller, Sheikh A. Akbar, and Patricia A. Morris. Nanoscale metal oxide-based heterojunctions for gas sensing: A review. *Sensors and Actuators B: Chemical*, 204:250–272, 2014. ISSN 0925-4005. doi: https://doi.org/10.1016/j.snb.2014.07.074. URL https://www.sciencedirect.com/science/article/pii/S0925400514009149.

[15] Kelsey Haddad, Ahmed Abokifa, Shalinee Kavadiya, Byeongdu Lee, Sriya Banerjee, Baranidharan Raman, Parag Banerjee, Cynthia Lo, John Fortner, and Pratim Biswas. Sno2 nanostructured thin films for room-temperature gas sensing of volatile organic compounds. *ACS Applied Materials & Interfaces*, 10 (35):29972–29981, 2018. ISSN 1944-8244. doi: 10.1021/acsami.8b08397. URL https://doi.org/10.1021/acsami.8b08397.

[16] Marcus Kennedy Dr. *Investigation of tin oxide (SnOx) gas sensors based on monodisperse nanoparticle films*. Thesis. URL https://duepublico2.uni-due.de/receive/duepublico_mods_00005525.

[17] Ganhua Lu, Kyle L. Huebner, Leonidas E. Ocola, Marija Gajdardziska-Josifovska, and Junhong Chen. Gas sensors based on tin oxide nanoparticles synthesized from a mini-arc plasma source. *Journal of Nanomaterials*, 2006:060828, 2006. ISSN 1687-4110. doi: 10.1155/JNM/2006/60828. URL https://doi.org/10.1155/JNM/2006/60828.

[18] G. D. Khuspe, R. D. Sakhare, S. T. Navale, M. A. Chougule, Y. D. Kolekar, R. N. Mulik, R. C. Pawar, C. S. Lee, and V. B. Patil. Nanostructured sno2 thin films for no2 gas sensing applications. *Ceramics International*, 39(8):8673–8679, 2013. ISSN 0272-8842. doi: https://doi.org/10.1016/j.ceramint.2013.04.047. URL https://www.sciencedirect.com/science/article/pii/S0272884213004380.

[19] Dasari Sunil Gavaskar, P. Nagaraju, Yelsani Vijayakumar, P. S. Reddy, and M. V. Ramana Reddy. Low-cost ultra-sensitive sno2-based ammonia sensor synthesized by hydrothermal method. *Journal of Asian Ceramic Societies*, 8(3):605–614, 2020. ISSN null. doi: 10.1080/21870764.2020.1769820. URL https://doi.org/10.1080/21870764.2020.1769820.

[20] K. Govardhan and Andrews Nirmala Grace. Temperature optimized ammonia and ethanol sensing using ce doped tin oxide thin films in a novel flow metric gas sensing chamber. *Journal of Sensors*, 2016: 7652450, 2016. ISSN 1687-725X. doi: 10.1155/2016/7652450. URL https://doi.org/10.1155/2016/7652450.

[21] Jaise Mariya George, Arun Antony, and Beena Mathew. Metal oxide nanoparticles in electrochemical sensing and biosensing: a review. *Microchimica Acta*, 185(7):358, 2018. ISSN 1436-5073. doi: 10.1007/s00604-018-2894-3. URL https://doi.org/10.1007/s00604-018-2894-3.

[22] Sonik Bhatia, Neha Verma, and R. K. Bedi. Ethanol gas sensor based upon zno nanoparticles prepared by different techniques. *Results in Physics*, 7:801–806, 2017. ISSN 2211-3797. doi: https://doi.org/10.1016/j.rinp.2017.02.008. URL https://www.sciencedirect.com/science/article/pii/S2211379716307756.

[23] Ahmad Ahmadi daryakenari, Mohammad Ahmadi Daryakenari, Yaser Bahari, and Hamid Omidvar. Preparation and ethanol sensing properties of zno nanoparticles via a novel sol-gel method. *ISRN Nanotechnology*, 2012, 2012. doi: 10.5402/2012/879480.

[24] Prabhakar Rai and Yeon-Tae Yu. Citrate-assisted hydrothermal synthesis of single crystalline zno nanoparticles for gas sensor application. *Sensors and Actuators B: Chemical*, 173:58–65, 2012. ISSN 0925-4005. doi: https://doi.org/10.1016/j.snb.2012.05.068. URL https://www.sciencedirect.com/science/article/pii/S0925400512005382.

[25] Faying Fan, Yongjun Feng, Shouli Bai, Junting Feng, Aifan Chen, and Dianqing Li. Synthesis and gas sensing properties to no2 of zno nanoparticles. *Sensors and Actuators B: Chemical*, 185:377–382, 2013. ISSN 0925-4005. doi: https://doi.org/10.1016/j.snb.2013.05.020. URL https://www.sciencedirect.com/science/article/pii/S0925400513005832.

[26] Mónica Acuautla, Sandrine Bernardini, Laurent Gallais, and M. Marc Bendahan. Ammonia sensing properties of zno nanoparticles on flexible substrate. 2014.

[27] Yueming Li, Jing Liang, Zhanliang Tao, and Jun Chen. Cuo particles and plates: Synthesis and gas-sensor application. *Materials Research Bulletin - MATER RES BULL*, 43:2380–2385, 2008. doi: 10.1016/j.materresbull.2007.07.045.

[28] Fang Wang, Hairong Li, Zhaoxin Yuan, Yongzhe Sun, Fangzhi Chang, Heng Deng, Longzhen Xie, and Haiyan Li. A highly sensitive gas sensor based on cuo nanoparticles synthetized via a sol–gel method. *RSC Advances*, 6(83):79343–79349, 2016. doi: 10.1039/C6RA13876D. URL http://dx.doi.org/10.1039/C6RA13876D.

[29] Katarzyna Zakrzewska and Marta Radecka. Tio2-based nanomaterials for gas sensing—influence of anatase and rutile contributions. *Nanoscale Research Letters*, 12, 2017. doi: 10.1186/s11671-017-1875-5.

[30] Wojciech Maziarz, Anna Kusior, and Anita Trenczek-Zajac. Nanostructured tio(2)-based gas sensors with enhanced sensitivity to reducing gases. *Beilstein journal of nanotechnology*, 7:1718–1726, 2016. ISSN 2190-4286. doi: 10.3762/bjnano.7.164. URL https://pubmed.ncbi.nlm.nih.gov/28144521https://www.ncbi.nlm.nih.gov/pmc/articles/PMC5238649/.

[31] Shi Guang Shang, Xin Li, Ling Zhao, Rui Lu, and Hai Feng Chen. Synthesis, characterization and gas sensing properties of titanium dioxide nanoparticles by sol-gel method. *Materials Science Forum*, 852:238–243, 2016. ISSN 1662-9752. doi: 10.4028/www.scientific.net/MSF.852.238. URL https://www.scientific.net/MSF.852.238.

[32] Yu Du, Weinan Wang, Xiaowei Li, Jing Zhao, Jinming Ma, Yinping Liu, and Geyu Lu. Preparation of nio nanoparticles in microemulsion and its gas sensing performance. *Materials Letters*, 68:168–170, 2012. ISSN 0167-577X. doi: https://doi.org/10.1016/j.matlet.2011.10.039. URL https://www.sciencedirect.com/science/article/pii/S0167577X11012018.

[33] Nishchay A. Isaac, Marco Valenti, Andreas Schmidt-Ott, and George Biskos. Characterization of tungsten oxide thin films produced by spark ablation for no2 gas sensing. *ACS Applied Materials & Interfaces*, 8(6):3933–3939, 2016. ISSN 1944-8244. doi: 10.1021/acsami.5b11078. URL https://doi.org/10.1021/acsami.5b11078.

[34] Rui Lu, Xiaoling Zhong, Shiguang Shang, Shan Wang, and Manling Tang. Effects of sintering temperature on sensing properties of wo 3 and ag-wo 3 electrode for no 2 sensor. *Royal Society Open Science*, 5:171691, 2018. doi: 10.1098/rsos.171691.

[35] Vibha Srivastava and Kiran Jain. Highly sensitive nh3 sensor using pt catalyzed silica coating over wo3 thick films. *Sensors and Actuators B: Chemical*, 133(1):46–52, 2008. ISSN 0925-4005. doi: https://doi.org/10.1016/j.snb.2008.01.066. URL https://www.sciencedirect.com/science/article/pii/S0925400508000932.

[36] Niranjan Ramgir, Niyanta Datta, Manmeet Kaur, S. Kailasaganapati, A. K. Debnath, D. K. Aswal, and S. K. Gupta. Ammonia sensor based on wo3 thin films. *AIP Conference Proceedings*, 1451(1):185–187, 2012. ISSN 0094-243X. doi: 10.1063/1.4732409. URL https://aip.scitation.org/doi/abs/10.1063/1.4732409.

[37] Giuseppe Mele, Roberta Del Sole, and Xiangfei Lü. *18 - Applications of TiO2 in sensor devices*, pages 527–581. Elsevier, 2021. ISBN 978-0-12-819960-2. doi: https://doi.org/10.1016/B978-0-12-819960-2.00004-3. URL https://www.sciencedirect.com/science/article/pii/B9780128199602000043.

[38] Ananya Dey. Semiconductor metal oxide gas sensors: A review. *Materials Science and Engineering: B*, 229:206–217, 2018. ISSN 0921-5107. doi: https://doi.org/10.1016/j.mseb.2017.12.036. URL https://www.sciencedirect.com/science/article/pii/S0921510717303574.

[39] Nadeem Baig, Irshad Kammakakam, and Wail Falath. Nanomaterials: a review of synthesis methods, properties, recent progress, and challenges. *Materials Advances*, 2(6):1821–1871, 2021. doi: 10.1039/D0MA00807A. URL http://dx.doi.org/10.1039/D0MA00807A.

[40] Mritunjaya Parashar, Vivek Kumar Shukla, and Ranbir Singh. Metal oxides nanoparticles via sol–gel method: a review on synthesis, characterization and applications. *Journal of Materials Science: Materials in Electronics*, 31(5):3729–3749, 2020. ISSN 1573-482X. doi: 10.1007/s10854-020-02994-8. URL https://doi.org/10.1007/s10854-020-02994-8.

[41] Ajay Vasudeo Rane, Krishnan Kanny, V. K. Abitha, and Sabu Thomas. *Chapter 5 - Methods for Synthesis of Nanoparticles and Fabrication of Nanocomposites*, pages 121–139. Woodhead Publishing, 2018. ISBN 978-0-08-101975-7. doi: https://doi.org/10.1016/B978-0-08-101975-7.00005-1. URL https://www.sciencedirect.com/science/article/pii/B9780081019757000051.

[42] Jianlin Li, Qingliu Wu, and Ji Wu. *Synthesis of Nanoparticles via Solvothermal and Hydrothermal Methods*, pages 295–328. 2016. ISBN 978-3-319-15337-7. doi: 10.1007/978-3-319-15338-4_17.

[43] Margarita Sanchez-Dominguez, Magali Boutonnet, and Conxita Solans. A novel approach to metal and metal oxide nanoparticle synthesis: the oil-in-water microemulsion reaction method. *Journal of Nanoparticle Research*, 11(7):1823, 2009. ISSN 1572-896X. doi: 10.1007/s11051-009-9660-8. URL https://doi.org/10.1007/s11051-009-9660-8.

[44] Myungjoon Kim, Saho Osone, Taesung Kim, Hidenori Higashi, and Takafumi Seto. Synthesis of nanoparticles by laser ablation: A review. *KONA Powder and Particle Journal*, advpub, 2017. doi: 10.14356/kona.2017009.

[45] N. S. Tabrizi, M. Ullmann, V. A. Vons, U. Lafont, and A. Schmidt-Ott. Generation of nanoparticles by spark discharge. *Journal of Nanoparticle Research*, 11(2):315, 2008. ISSN 1572-896X. doi: 10.1007/s11051-008-9407-y. URL https://doi.org/10.1007/s11051-008-9407-y.

[46] T. V. Pfeiffer, J. Feng, and A. Schmidt-Ott. New developments in spark production of nanoparticles. *Advanced Powder Technology*, 25(1):56–70, 2014. ISSN 0921-8831. doi: https://doi.org/10.1016/j.apt.2013.12.005. URL https://www.sciencedirect.com/science/article/pii/S0921883113002446.

[47] Sung Lee. Electrodes for semiconductor gas sensors. *Sensors*, 17:683, 2017. doi: 10.3390/s17040683.

[48] X. Vilanova, E. Llobet, J. Brezmes, J. Calderer, and X. Correig. Numerical simulation of the electrode geometry and position effects on semiconductor gas sensor response. *Sensors and Actuators B: Chemical*, 48(1):425–431, 1998. ISSN 0925-4005. doi: https://doi.org/10.1016/S0925-4005(98)00080-X. URL https://www.sciencedirect.com/science/article/pii/S092540059800080X.

[49] M. J. Toohey. Electrodes for nanodot-based gas sensors. *Sensors and Actuators B: Chemical*, 105(2):232–250, 2005. ISSN 0925-4005. doi: https://doi.org/10.1016/j.snb.2004.06.006. URL https://www.sciencedirect.com/science/article/pii/S0925400504004319.

[50] V. Guarnieri, L. Biazi, R. Marchiori, and A. Lago. Platinum metallization for mems application. focus on coating adhesion for biomedical applications. *Biomatter*, 4, 2014. ISSN 2159-2527 (Print) 2159-2527. doi: 10.4161/biom.28822.

[51] Nguyen Viet Long, Toshiharu Teranishi, Yong Yang, Cao Thi, Yanqin Cao, and M. Nogami. Iron oxide nanoparticles for next generation gas sensors. *International Journal of Metallurgical & Materials Engineering*, 1:119, 2015. doi: 10.15344/2455-2372/2015/119.

[52] Mokhtar Hjiri, Mohamed Salah Aida, and Giovanni Neri. No2 selective sensor based on α-fe2o3 nanoparticles synthesized via hydrothermal technique. *Sensors (Basel, Switzerland)*, 19(1):167, 2019. ISSN 1424-8220. doi: 10.3390/s19010167. URL https://pubmed.ncbi.nlm.nih.gov/30621254https://www.ncbi.nlm.nih.gov/pmc/articles/PMC6338989/.

[53] Anne-Marije Andringa, Juliaan R. Meijboom, Edsger C. P. Smits, Simon G. J. Mathijssen, Paul W. M. Blom, and Dago M. de Leeuw. Gate-bias controlled charge trapping as a mechanism for no2 detection with field-effect transistors. *Advanced Functional Materials*, 21(1):100–107, 2011. ISSN 1616-301X. doi: https://doi.org/10.1002/adfm.201001560. URL https://doi.org/10.1002/adfm.201001560.

[54] Maria Tanese, Daniel Fine, Ananth Dodabalapur, and Luisa Torsi. Interface and gate bias dependence responses of sensing organic thin-film transistors. *Biosensors & bioelectronics*, 21:782–8, 2005. doi: 10.1016/j.bios.2005.01.016.

[55] Mark E. Roberts, Anatoliy N. Sokolov, and Zhenan Bao. Material and device considerations for organic thin-film transistor sensors. *Journal of Materials Chemistry*, 19(21):3351–3363, 2009. ISSN 0959-9428. doi: 10.1039/B816386C. URL http://dx.doi.org/10.1039/B816386C.

[56] Jiri Janata and Mira Josowicz. Organic semiconductors in potentiometric gas sensors. *Journal of Solid State Electrochemistry*, 13(1):41, 2008. ISSN 1433-0768. doi: 10.1007/s10008-008-0597-0. URL https://doi.org/10.1007/s10008-008-0597-0.

[57] B. R. Bunes, T. Knowlton, D. L. Jacobs, P. Slattum, and L. Zang. Dual gate architecture for high sensitivity, high selectivity chemical-sensing field effect transistors. In *SENSORS, 2014 IEEE*, pages 62–65. ISBN 1930-0395. doi: 10.1109/ICSENS.2014.6984933.

[58] VSPARTICLE. The vsp-g1 nanoparticle generator. URL https://vsparticle.com/products/vsp-g1-nanoparticle-generator.

[59] Chaim Gutfinger. Aerosol measurement: Principles, techniques, and applications. *International Journal of Multiphase Flow - INT J MULTIPHASE FLOW*, 22:807–808, 1996. doi: 10.1016/0301-9322(96)00006-7.

[60] András E. Vladár and Vasile-Dan Hodoroaba. *Chapter 2.1.1 - Characterization of nanoparticles by scanning electron microscopy*, pages 7–27. Elsevier, 2020. ISBN 978-0-12-814182-3. doi: https://doi.org/10.1016/B978-0-12-814182-3.00002-X. URL https://www.sciencedirect.com/science/article/pii/B978012814182300002X.

[61] J. Goldstein, Dale Newbury, David Joy, Charles Lyman, Patrick Echlin, Eric Lifshin, Linda Sawyer, and Joseph Michael. *Scanning Electron Microscopy and X-ray Microanalysis ISBN: 0306472929*, volume XIX. 2003. ISBN 0306472929. doi: 10.1007/978-1-4615-0215-9.

[62] ECTM. Cascade probe station. URL http://ectm.tudelft.nl/Repository/repitem.php?id=32&ti=13.

[63] Owlstone. Owlstone gen-sys. URL https://www.owlstoneinc.com/products/gen-sys-products/.

[64] Keithley. Keithley 2612b. URL https://www.tek.com/en/keithley-source-measure-units/smu-2600b-series-sourcemeter-manual/models-2611b-2612b-and-2614b-syste.

[65] EDA Solutions. L-edit ic. URL https://www.eda-solutions.com/products/tanner-l-edit-ic-layout/.

[66] B. E. Deal and A. S. Grove. General relationship for the thermal oxidation of silicon. *Journal of Applied Physics*, 36:3770–3778, 1965. ISSN 0021-8979. doi: 10.1063/1.1713945. URL https://ui.adsabs.harvard.edu/abs/1965JAP....36.3770D.

[67] Jindřich Leitner and David Sedmidubský. Thermodynamic modeling of oxidation of tin nanoparticles. *Journal of Phase Equilibria and Diffusion*, 40(1):10–20, 2019. ISSN 1863-7345. doi: 10.1007/s11669-018-0686-4. URL https://doi.org/10.1007/s11669-018-0686-4.

[68] H. Meng. Gas sensor based on array of multi-layer graphene decorated with metal/metal oxide nanoparticles. Master's thesis, Delft University of Technology, 2022.

[69] Nik Dennler, Shavika Rastogi, Jordi Fonollosa, André van Schaik, and Michael Schmuker. Drift in a popular metal oxide sensor dataset reveals limitations for gas classification benchmarks. *Sensors and Actuators B: Chemical*, 361:131668, 2022. ISSN 0925-4005. doi: https://doi.org/10.1016/j.snb.2022.131668. URL https://www.sciencedirect.com/science/article/pii/S0925400522003100.

[70] Bilge Saruhan, Roussin Lontio Fomekong, and Svitlana Nahirniak. Review: Influences of semiconductor metal oxide properties on gas sensing characteristics. *Frontiers in Sensors*, 2, 2021. ISSN 2673-5067. doi: 10.3389/fsens.2021.657931. URL https://www.frontiersin.org/articles/10.3389/fsens.2021.657931.

[71] M. Kennedy, F. Kruis, Heinz Fissan, and B. Mehta. Fully automated, gas sensing, and electronic parameter measurement setup for miniaturized nanoparticle gas sensors. *Review of Scientific Instruments*, 74, 2003. doi: 10.1063/1.1619552.

[72] E. Franke, Marion, J. Koplin, Tobias, and Ulrich Simon. Metal and metal oxide nanoparticles in chemiresistors: Does the nanoscale matter? *Small*, 2(1):36–50, 2006. ISSN 1613-6810. doi: https://doi.org/10.1002/smll.200500261. URL https://onlinelibrary.wiley.com/doi/abs/10.1002/smll.200500261.